

Asif Iqbal Zia

Subhas Chandra Mukhopadhyay

Electrochemical Sensing: Carcinogens in Beverages

Smart Sensors, Measurement and Instrumentation

Volume 20

Series editor

Subhas Chandra Mukhopadhyay
School of Engineering and Advanced Technology (SEAT)
Massey University (Manawatu)
Palmerston North
New Zealand
e-mail: S.C.Mukhopadhyay@massey.ac.nz

More information about this series at <http://www.springer.com/series/10617>

Asif Iqbal Zia · Subhas Chandra Mukhopadhyay

Electrochemical Sensing: Carcinogens in Beverages

 Springer

Asif Iqbal Zia
Massey University
Palmerston North
New Zealand

Subhas Chandra Mukhopadhyay
Massey University
Palmerston North
New Zealand

ISSN 2194-8402 ISSN 2194-8410 (electronic)
Smart Sensors, Measurement and Instrumentation
ISBN 978-3-319-32654-2 ISBN 978-3-319-32655-9 (eBook)
DOI 10.1007/978-3-319-32655-9

Library of Congress Control Number: 2016938654

© Springer International Publishing Switzerland 2016

This work is subject to copyright. All rights are reserved by the Publisher, whether the whole or part of the material is concerned, specifically the rights of translation, reprinting, reuse of illustrations, recitation, broadcasting, reproduction on microfilms or in any other physical way, and transmission or information storage and retrieval, electronic adaptation, computer software, or by similar or dissimilar methodology now known or hereafter developed.

The use of general descriptive names, registered names, trademarks, service marks, etc. in this publication does not imply, even in the absence of a specific statement, that such names are exempt from the relevant protective laws and regulations and therefore free for general use.

The publisher, the authors and the editors are safe to assume that the advice and information in this book are believed to be true and accurate at the date of publication. Neither the publisher nor the authors or the editors give a warranty, express or implied, with respect to the material contained herein or for any errors or omissions that may have been made.

Printed on acid-free paper

This Springer imprint is published by Springer Nature
The registered company is Springer International Publishing AG Switzerland

Preface

The research work required to do a substantial addition to the existing knowledge includes, but not limited to the literature surveys in electrochemical spectroscopy and allied fields, design and developments, simulations and fabrications, experimentation and analyses, measurements and hypothesis, functionalization and immobilization, selectivity and sensitivity, detailed mathematical and statistical analyses, and result validations. The presented research work has successfully been applied to develop an exciting transducer that could not only selectively detect its target but is also capable enough to quantify harmful synthetic organic impurities in our foodstuff. This research work has not only provided a real-time tool to perform week-long chemical and biochemical assays in minutes, but had also played its part as a source for community awareness about the said chemicals that we keep ingesting knowingly or unknowingly. Consequently, these teratogenic, endogenic and carcinogenic chemicals become our body burden, and we fall prey to some incurable diseases that shorten our lifespan.

Phthalates are the most ubiquitous chemicals that pose a grave danger to the human race due to their extraordinary use as a plasticizer in consumer product industry. All contemporary detection methods require a high level of skills, expensive equipment and long analysis time as compared to the technique presented in this research work that introduces a real-time non-invasive assay. A novel type of silicon substrate based smart interdigital transducer was fabricated by employing thin-film micro-electromechanical system semiconductor device fabrication technology. Electrochemical impedance spectroscopy was used in conjunction with the fabricated sensor to detect hormones and phthalates in deionized water, energy drinks, and juices. Various concentrations of phthalates as low as 2 parts per billion to a higher level of 200 parts per million in deionized water, energy drinks, and juices were detected distinctively using the new planar interdigital sensor based EIS sensing system. The sensor was functionalized by a self-assembled monolayer of 3-aminopropyltriethoxysilane embedded with molecularly imprinted polymer to introduce selectivity for the phthalate molecule. Spectrum analysis algorithm converted the experimentally obtained impedance spectra into useful information about the analyte by applying complex nonlinear least-square

curve fitting in order to obtain equivalent electrochemical circuit and corresponding circuit parameters describing the kinetics of the electrochemical cell. Principal component analysis was applied to monitor the effects of a surface-immobilized molecularly imprinted polymer layer on the evaluated circuit parameters and its electrical response.

The major contribution of this research work is the development of a smart sensing system that owns the capabilities to detect hormones and endocrine disruptor compounds in foodstuffs. Low-cost and robustness are the merit points that make this system unique. This system is sufficiently flexible to be readily coupled with any existing chemical and biochemical sensing technique.

The contributions of this research work can be summarized as follows:

1. Explore a novel interdigital capacitive sensor design that owns enough penetration depth of the fringing electric field, sufficient to allow bulk sample testing.
2. Analyse the new sensor design by finite element analysis and select the most precise configuration of interdigital electrodes under given boundary conditions.
3. Fabricate smart sensor interdigital configuration on a silicon substrate using MEMS-based semiconductor fabrication technology.
4. Analyse and achieve stability and reproducibility in impedance measurement characteristics of the smart sensor design.
5. Establish automatic data acquisition setup to measure impedance characteristics of an electrochemical cell using the fabricated sensor.
6. Real-time detection and analysis of hormones in a bulk aqueous medium by applying electrochemical impedance spectroscopy technique.
7. Real-time detection and analysis of two phthalate esters in polar, electrolytic, and acidic media using electrochemical impedance spectroscopy technique in bulk samples.
8. Develop and tailor robust technique to induce selectivity for the phthalate analyte in the smart sensing system.
9. Explore and apply the self-assembled monolayer (SAM) technique to immobilize analyte-selective functional material on highly polished silicon substrate based smart sensor.
10. Analyse the performance of the intelligent selective sensor and its validation by commercially available detection methodology.

One of the main objectives of this research was to develop an assay system that is robust enough to have an in-field application without any technical expertise requirement for the user and is sufficiently rapid to be used for real-time monitoring of beverage products at industrial level. In order to achieve this objective, a real-time label-free assay protocol was tailored and applied by introducing “artificial antibodies” to induce selectivity in the designed sensing system. The results obtained by the testing system were validated using commercially available high-performance liquid chromatography, diode array detection at an incident wavelength of 224 nm. DEHP tainted energy drinks and juices were also investigated by the developed technology in order to validate its operation in the real-world scenario.

The authors are indebted to many colleagues for their significant contribution to the research: Associate Profs. Pak-Lam Yu and Ibrahim Al-Bahadly, Dr. Chinthaka Gooneratne, Dr. Jürgen Kosel, Dr. Muhammad Syaifuddin, Ms. Nasrin Afsarimanish, Mr. Hemant Ghayvat, Mrs. Li (Shelly) Xie, Ms. Apeksha Rao, and Mr. Anindya Nag. Also sincere thanks to Ms. Trish O’Grady, Mrs. Ann-Marie Jackson, Mrs. Judy, Ms. Julia Good, Mr. Ken Mercer, Mr. Collin Plaw, Mr. Bruce Collins, Mr. Doug, Mr. John Sykes, Mr. John Edwards, Mr. Ian Thomas, Mrs. Lisa Lightband, Mr. Conal Hodgetts, and Mr. Brendon for assistance and support. Special thanks to Massey University for the research facilities, Higher Education Commission of Pakistan (HEC) and top management of COMSATS University for the financial assistance. Last but not least, we are indebted to our families for unqualified moral support and encouragement throughout the project.

Pakistan
New Zealand

Asif Iqbal Zia
Subhas Chandra Mukhopadhyay

Contents

1	Human Endocrine System and Hormonal Measurement	1
1.1	Hormones and Endocrine-Disrupting Compounds	1
1.2	Receptor–Ligand Binding Assays	4
1.2.1	Radio Receptor Assay (RRA).	5
1.2.2	Scintillation Proximity Assay (SPA)	5
1.2.3	Fluorescence Resonance Energy Transfer (FRET)	6
1.2.4	Fluorescence Polarization (FP)	7
1.2.5	Fluorometric Microvolume Assay (FMAT)	8
1.2.6	AlphaScreen™	8
1.2.7	Flow Cytometry	9
1.2.8	Fluorescence Correlation Spectroscopy (FCS)	9
1.3	Immunoassay	10
1.3.1	Surface Plasmon Resonance (SPR)	11
1.3.2	Total Internal Reflection Fluorescence (TIRF)	12
1.3.3	Ellipsometry	13
1.3.4	Nuclear Magnetic Resonance Spectroscopy	13
1.3.5	Amperometric Immunosensors	14
1.3.6	Conductimetric Immunosensors.	14
1.3.7	Surface Acoustic Wave Immunosensors (SAW)	14
1.3.8	Enzyme-Linked Immunosorbent Assay (ELISA)	15
1.4	Conclusions	17
	References	17
2	Impedance Spectroscopy and Experimental Setup	21
2.1	Introduction	21
2.2	Electrochemical Impedance Spectroscopy.	21
2.2.1	AC Bridges.	22
2.2.2	Lissajous Curves.	22
2.2.3	Fast Fourier Transforms (FFT).	22
2.2.4	Phase Sensitive Detections (PSD)	23
2.2.5	Frequency Response Analysis (FRA).	23

2.2.6	Electrochemical Impedance Spectroscopy; Theory and Analyses	24
2.2.7	'Nyquist' and 'Bode' Plots for Impedance Data Analysis . . .	28
2.2.8	Randle's Electrochemical Cell Equivalent Circuit Model . . .	28
2.3	Experimental Setup	32
2.3.1	Equipment and Instrumentations	33
2.3.2	Fixture and Test Probe Connections.	33
2.3.3	RS-232C Interface for 3522-50/3532-50 LCR Hi Tester. . .	34
2.3.4	Conclusions	35
	References	36
3	Novel Interdigital Sensors' Development	39
3.1	Introduction to Interdigital Sensors	39
3.2	Novel Planar Interdigital Sensors.	41
3.3	Finite Element Modelling Using COMSOL Multiphysics®.	42
3.4	Sensors' Fabrication	49
3.5	Sensors' Profiling and Problem Definition.	56
3.5.1	Connection Pads Soldering	56
3.6	Performance Evaluation	57
3.6.1	Experimental Evaluation	57
3.7	Achieving Stability in Sensors' Performance.	58
3.7.1	Post-fabrication Anneal of ID Sensor.	60
3.7.2	Results' Validation	62
3.7.3	Complex Nonlinear Least Squares Curve Fitting.	62
3.7.4	Principal Component Analysis (PCA)	66
3.7.5	PCA Analysis—EC1 (30–90 °C) Anneal	67
3.7.6	PCA Analysis—EC2 (91–150 °C) Anneal.	68
3.7.7	PCA Analysis—EC3 (151–210 °C) Anneal.	70
3.8	Conclusions	72
	References.	72
4	Electrochemical Detection of Hormones.	75
4.1	Introduction	75
4.2	Detection of Ovarian Hormone Estrone Glucuronide (E1G).	76
4.2.1	Motivation	76
4.2.2	Point-of-Care Methods	77
4.2.3	Basal Body Temperature Method (BBT)	77
4.2.4	Billings Ovulation Method.	77
4.2.5	Symptothermal Method (STM)	77
4.2.6	Ovarian Monitor	78
4.2.7	Materials and Methods to Detect E1G.	78
4.2.8	Results and Discussions	79
4.2.9	Electrochemical Impedance Spectroscopy Analyses for E1G	82
4.2.10	E1G Sensitivity Analysis	83

4.3	Electrochemical Detection of Progesterone Hormone	85
4.3.1	Motivation	85
4.3.2	Materials and Methods for Progesterone Detection	87
4.3.3	Electrochemical Impedance Analyses for Progesterone	87
4.4	Conclusions	91
	References	91
5	Electrochemical Detection of Endocrine Disrupting Compounds	93
5.1	Introduction	93
5.2	Impedimetric Detection of DEHP and DINP	95
5.2.1	Motivation	96
5.2.2	Materials and Methods	97
5.2.3	DEHP Detection Test in Deionized Water	98
5.2.4	Experimental Data Analyses by CNLS Curve Fitting	99
5.2.5	Sensitivity Analysis—DEHP	103
5.2.6	DEHP Detection in Commercially Sold Energy Drink	104
5.2.7	Impedance Measurements of DINP-Spiked Ethanol Samples	106
5.2.8	Impedance Measurements of DINP-Spiked Orange Juice	108
5.3	Conclusions	109
	References	110
6	Inducing Analyte Selectivity in the Sensing System	113
6.1	Introduction	113
6.2	Materials and Methods	115
6.2.1	Synthesis of DEHP Imprinted Polymer	116
6.3	EIS for Detection of DEHP in MilliQ	117
6.3.1	Results and Discussions	122
6.4	Adsorption Studies of DEHP to MIP	123
6.4.1	Static Adsorption of DEHP to MIP	123
6.4.2	Uptake Kinetics of MIP Coated Sensor to DEHP	124
6.5	Data Analyses Using Nonlinear Least Square Curve Fitting	125
6.6	Results Validation by HPLC	126
6.7	DEHP in Energy Drink—MIP Coated Sensor	128
6.8	Conclusions	131
	References	131
7	Portable Low-Cost Testing System for Phthalates' Detection	133
7.1	Introduction	133
7.2	Motivation	133
7.3	Development of Portable FRA Device	134
7.4	System Design	134
7.5	Materials and Methods	136

7.6	Results and Discussions	137
7.7	Electrochemical Impedance Spectroscopy Characterization	138
7.8	Conclusions	140
	References	141
8	Conclusions and Future Research	143
8.1	Summary and Conclusions	143
8.2	Future Work	147
8.2.1	Sensitivity and Selectivity Improvement	147
8.2.2	Thick Film Electrodes	147
8.2.3	Substrate Type	148

Chapter 1

Human Endocrine System and Hormonal Measurement

1.1 Hormones and Endocrine-Disrupting Compounds

The endocrine system in living organisms is made up of the set of cells and glands that produce chemical signals called hormones. Hormones travel through human bloodstream to approach respective receptors in the target cells. The major function of the endocrine system is to regulate nutrient supply to all cells, growth and reproduction. Anatomic positions of the glands of the endocrine system are shown in Fig. 1.1. Each set of glands relates to a particular function in the human body hence behave as a chemical control house to regulate the efficient operation of the other body organs. Table 1.1 provides a detail of the glands forming endocrine system and their function in the human body.

Endocrine Disruptors (EDs) are exogenous chemicals or mixture of chemicals that interfere with the ordinary functioning of the endocrine system and hormones. Among the known endocrine disruptors, the most ubiquitous are esters of 1-2-Benzenedicarboxylic acid commonly known as phthalates. These industrial chemicals have a significant number of commercial uses such as lubricants, additives, solvents, softeners for plastics including food and beverage packaging, cosmetics, insecticides, paints, medical and pharmaceutical applications [1]. Since phthalate esters are not covalently attached to the polyvinyl chloride (PVC) lattice structure, they leach, migrate, and evaporate directly into foodstuffs and atmosphere exposing human beings through ingestion, inhalation and dermal routes [2]. These can directly infuse into body fluids via medication and disposable medical plastic products [3].

Phthalates have been declared as ubiquitous environmental pollutants and endocrine disruptors by several health monitoring agencies all over the world for carcinogenic and teratogenic effects observed as reproductive and developmental defects in rodents [4, 5]. Published research concludes that phthalates pose highest toxicity and endocrine disruptive threat to the human race, especially to young children, infants, pregnant and nursing mothers [6]. Recent researchers have suggested declining trend in the human reproductive hormonal levels, damage to sperm DNA and reduced sperm count in male adults [5]; whereas, the elevated

Fig. 1.1 The endocrine system in human body

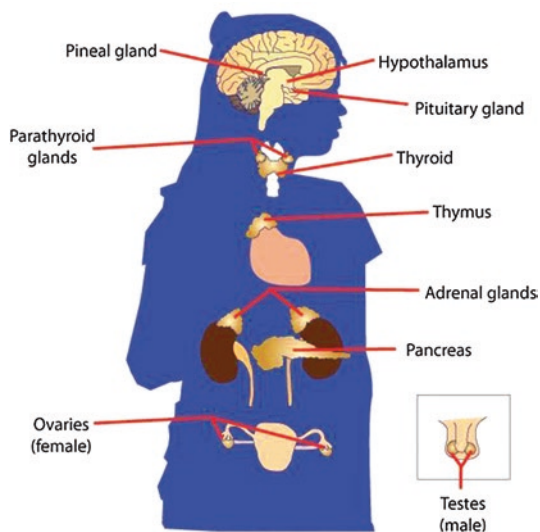


Table 1.1 Endocrine system's glands, hormones and their function

Gland	Hormones	Functions in human body
Hypothalamus	Releasing hormones	Stimulate pituitary activity
Pituitary	Trophic (stimulating)	Stimulate thyroid, gonadal and pancreatic activities
Thyroid	Thyroid	Regulates metabolism, growth and development
Adrenal	Corticosteroid hormones Catecholamine	Regulate metabolism and behaviour
Pancreas	Insulin and glucagon	Regulate blood sugar level
Gonads	Oestrogens and androgens	Regulate development and growth, reproduction, immunity, onset of puberty, and behaviour

risk of altered breast development and breast cancer, premature puberty and prostate changes in females [7, 8]. Leaching of phthalates into food from packaging [9]; from PET (PETE, polyethylene terephthalate) bottles into beverages and mineral water [2] and from corks of glass bottles has been published [10]. Wang et al. [11] showed that the phthalates leaching into the orange juice from tetra packaging grows 110 times higher than the safe intake limit of 6.0 $\mu\text{g}/\text{L}$ set by US EPA (The United States Environmental Protection Agency) during its shelf life and until close to its expiry date (Fig. 1.2). The guideline for safe drinking water published in a list of priority compounds, posing endocrine disrupting hazards to humans by World Health Organization (WHO) and the European Union sets 8.0 $\mu\text{g}/\text{L}$ as a maximum safe limit for DEHP presence in fresh and drinking water [12].

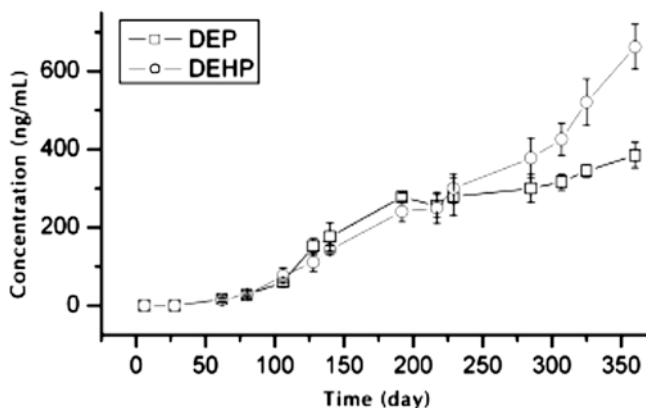


Fig. 1.2 Leaching of *DEHP* and *DEP* from tetra packaging within expiry date of orange packaged orange juice [11]

The ubiquitous presence of phthalates as an environmental pollutant and containment in laboratory apparatus seriously limits minimal detection level below 2-ppb even under the most stringent conditions and controlled setup [13]. Solid phase microextraction (SPME) is a solvent-free pre-concentration technique applied to extract phthalate metabolites from a mixture of compounds; in order to measure its quantity using Gas Chromatography (GC) and High-Performance Liquid Chromatography (HPLC) [14–17]. Different types of detectors are used to measure the amount of phthalates depending on the nature of the test sample. For example, DEHP is measured by GC using Electron Capture Detector (ECD) [18] and Flame Ionization Detector (FID) [7]. Liquid Chromatography (LC) coupled with Mass Spectrometry (MS) and UV detection are the most commonly applied well-established techniques [19].

In order to devise a rapid and efficient assay for hormones and EDCs, the author performed a detailed review of all the available contemporary commercial and laboratory techniques and methods used for hormone and EDCs detection. Hormone analysis is a very useful tool in the pharmaceutical, medical and biological sciences. It has been used as a diagnostic tool to confirm the disease and abnormality or to differentiate one physiological state from another. The method of hormone analysis has been changed throughout the years from bio-analysis to the more sophisticated techniques. However, every technique has its advantages and disadvantages and may be useful for different purposes. The best technique for measuring different hormones might also be different. Figure 1.3 shows all the types of phthalates used in the industrial sector.

Two major techniques used for hormone analysis are; receptor assay and immunoassay.

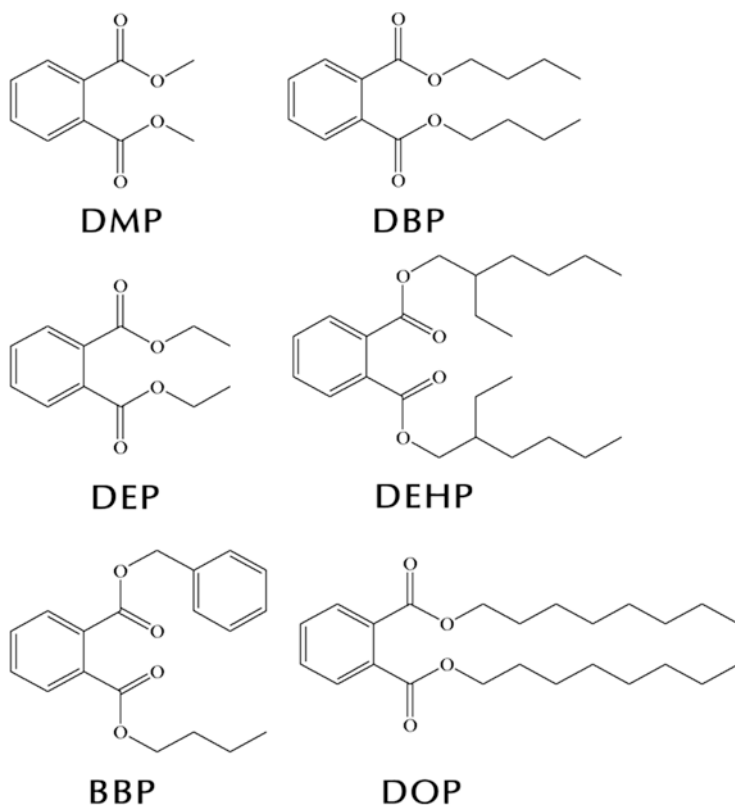


Fig. 1.3 Types of phthalates used in industry as plasticizers

1.2 Receptor–Ligand Binding Assays

In biochemistry, a **receptor** is a protein molecule found on the surface of a cell or embedded in the plasma membrane or the cytoplasm of a cell. It receives a particular chemical signal from one or more specific kinds of signalling molecules that may attach to it. The signalling molecule, which binds to a receptor, is called a ligand. A ligand may be a peptide or other small molecules such as a neurotransmitter, a pharmaceutical drug, a toxin or a hormone. The ideal assay should be selective, sensitive, easy to perform, reliable, low cost, fast and adaptable for automation. Moreover, ideal assay formats should not use any radioactive and toxic material in order to reduce health risks and environmental pollution as well as costs. Above all, the possibility to quantify multiple analytes in a single assay becomes more and more important, so the system should preferably be capable of multiplexing [20].

Receptor–ligand assays can be classified into three categories based on the detection techniques:

The heterogeneous assay uses washing; filtration, centrifuging or dialysis in order to separate the unbound fraction of the ligand from the receptor bound part of the analyte.

Homogeneous assay, on the other hand, is mix-and-measure assay. It does not require additional steps of washing, filtration, centrifuging or dialysis which induce an advantage of assay automation and miniaturization.

The non-separating homogeneous assay does not require separation procedures; rather a signal is centred or around a solid phase which contains the immobilised receptor or ligand [20].

1.2.1 Radio Receptor Assay (RRA)

Conventionally, receptor–ligand binding assays are heterogeneous and use radioactively labelled ligands for binding to a membrane-bound receptor. The principle is based on the interaction between a labelled ligand and an analyte for the same receptor binding site. After incubation of the labelled ligand, analyte and receptor it is necessary to filter or centrifuge to separate the free from bound fraction. The radioligand selected for RRA should be selective, chemically stable, radiochemically pure and must possess a high affinity for the respective receptor [21].

A major advantage of radio–ligand binding assays is sensitivity, selectivity and ease of use. Only one labelling step is required; that allows a quick set-up for the assay. The major drawback of these assays is, however, the use of radioactivity that poses a health risk to the operator and cause of producing radioactive waste. The requirement of separation of bound from free ligand renders these assays more labour-intensive and relatively slow.

1.2.2 Scintillation Proximity Assay (SPA)

SPA is a radioactive assay which involves immobilization of a receptor on a small (5 μm diameter) scintillant-containing microsphere and the ligand is labelled with a radioactive isotope. When this radioisotopically labelled molecule binds to the microsphere, the radioisotope comes in proximity to the scintillant. Energy transfer from the radioisotope to the scintillant takes place through emission of β particles to the scintillant which emits light photons as a consequence of the energy transfer. The light is detected by a phototube that in turn can be translated to the concentration of the ligand in the solution. The unbound radioactive ligand molecules lose energy in the aqueous medium without transferring it to the scintillant; hence, no photons are emitted due to unbound ligand molecules [22].

The technology has been widely utilized in a broad spectrum of applications, including mass measurement in research, pharmacological studies and biological function screening for analytes. The isotopes of interest in the SPA technique are [^3H] and [^{125}I], with a preference for ^{125}I due to its higher specific activity [23].

The advantage of mix-and-read-format makes this scintillation proximity assay easy to automate, which enhances assay reliability [23].

- Major disadvantages include the use of radioactivity making this technique very expensive and environment pollutant due to the production of radioactive waste.
- Another potential difficulty is the need to immobilize the receptor on a solid surface, where it should remain stable and maintain affinity.
- SPA is time-consuming (18 H) in comparison to a filtration assay (90 min). The time necessary to reach equilibrium for the receptor-bead interaction and to allow the beads to settle down in the microtiter plate is the leading cause. The latter is required to avoid signals from ligand that is not bound to the beads and can be accelerated by centrifugation. The relative long incubation time may also be a problem for sensitive receptors.

1.2.3 Fluorescence Resonance Energy Transfer (FRET)

Most of the mix-and-measure assays use the principle of fluorescence resonance energy transfer between ligand and receptor molecule when they come in proximity. FRET uses the transfer of energy from a donor molecule to an acceptor molecule, which depends on the distance between two, for detection. FRET employs sensitivity to distance for the study of molecular interactions. The transmission of energy from a donor to acceptor is radiation-free. The donor molecule is the dye or chromophore that initially absorbs the energy, and the acceptor is another chromophore to which subsequently absorbs energy [24]. This resonance interaction occurs over distances greater than the interatomic distances. It occurs without conversion into thermal energy or loss due to any molecular collision. The transfer of energy reduces the donor's fluorescence intensity and excited state lifetime which causes an increase in emission intensity of the acceptor. The kind of interaction that occurs in FRET is often referred as donor/acceptor interaction. FRET can result either in a decrease in fluorescence of the donor or an increase in fluorescence of the acceptor. The two resulting signals are compared to extract information [25] as shown in Fig. 1.4.

The advantage of this method is a measure of interaction; that is independent of the absolute concentration of the sensor [26, 27]. The disadvantage is the matter of proximity depending on the assay design, appropriate donor-acceptor pair selection, distinguishability from one another, and the requirement of enough spectral overlap for efficient energy transfer between donor and acceptor pair. The utility of this technique to measure receptor-ligand interactions in the homogeneous assay is also limited due to the requirement of labelling both the donor and acceptor

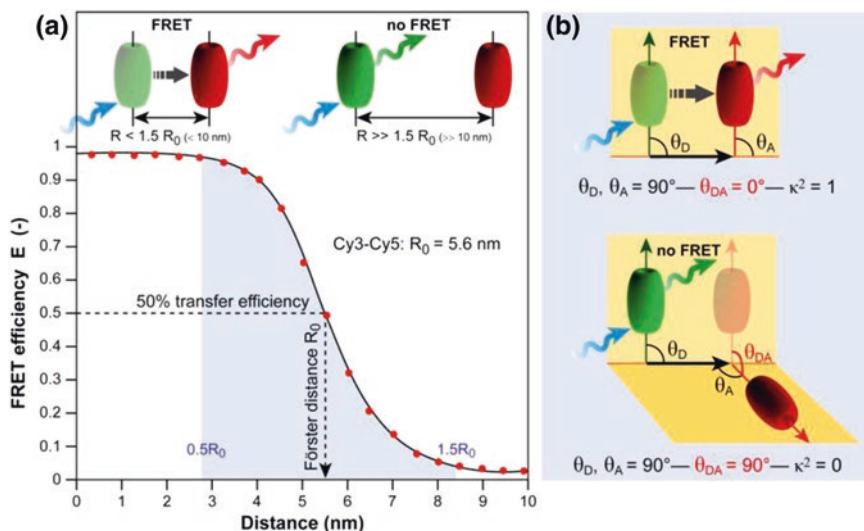


Fig. 1.4 Basic concept of FRET as a photophysical process. **a** The plot displays the dependence of the FRET efficiency on the proximity of the donor–acceptor pair. **b** Shows the effect of the angle between donor fluorochrome and acceptor molecule on FRET [25]

molecule. FRET is applied to study the structure and conformation of proteins [24]; spatial distribution and assembly of proteins [26]; receptor–ligand interactions [27]; immunoassays [28]; structure and conformation of nucleic acids [29].

1.2.4 Fluorescence Polarization (FP)

Fluorescence Polarization measurements are based on the assessment of the rotational motion of the molecular species upon excitation with polarized light. This technique measures the difference in the rotational speed of the ligand molecule upon binding to its receptor during an excited lifetime. The fluorescently labelled ligand is excited by polarized light, and the polarization of the emitted light is determined. Excitation of a fluorescent ligand with low molecular weight by polarized light results in depolarized light emitted in consequence of the rapid rotation of ligand. When the same fluorescent ligand is bound to a high molecular weight receptor, the rotational speed of the bound molecules decrease causing the emitted light remains partially polarized.

This technique has a distinct advantage of one-step labelling as compared to FRET that required two-step labelling. FP requires simple and less complicated testing setup. The disadvantages of this technique is a lack of precision at low (Nanomolar) concentrations; sensitivity is dependent on the affinity of ligand, intensity of the fluorophore and quantity of the receptor. Required precision for

an acceptable standard FP assay is achieved by keeping the receptor concentration, at least, 1 pmol/mg protein and the ligand affinity below 5 nM as stated by Gagne et al. [30]. The FP Assay technique has been applied to the soluble oestrogen receptor [31].

1.2.5 Fluorometric Microvolume Assay (FMAT)

This is mix-and-measure assay technique which makes use of commercially available laser scanner that measures multi-well plates. The small molecule ligand is labelled with a fluorophore and receptor is immobilized on beads in, either, 96, 384 or 864 multi-well plates with a transparent bottom and thick sidewalls of each well. The scanner scans a 1 mm² area using Helium–Neon red laser (633 nm) as the excitation source for fluorophore labelled ligands bound to receptor molecules. It uses two photomultiplier tubes with band pass filters for the respective labels to detect two independent red dye emissions e.g. Cy5 and Cy5.5. Multiplexing minimizes reagent consumption and increases throughput. The mix-and-measure format is achieved by discriminating between cell-associated and free fluorescence during data processing, where cell-associated fluorescence is detected as localized areas of strong fluorescence at the bottom of the well. In order to avoid interference from autofluorescence of the cells, long wavelength emitting red dyes are used, which results in a very sensitive assay. Laser-scanning imaging is an analogous technique to FMAT, which can also be used for multiplexing to measure ligand–receptor interactions [32].

1.2.6 AlphaScreenTM

This is homogeneous bead-based assay also known as Amplified Luminescence Proximity Homogenous Assay. The donor used for this assay is singlet oxygen (¹O₂, half-life 4 μs). On excitation with a wavelength of 680 nm, photosensitizer present in the donor beads convert ambient oxygen to singlet oxygen, that can travel a longer distance (200 nm) allowing the assay to probe interactions over a longer distance than FRET. The receptor is immobilized on donor beads whereas antibody-captured ligand is present on acceptor bead. If acceptor bead is in the close proximity to the donor, i.e. less than 200 nm, the singlet oxygen transfers its energy in order to return to ground state, to the acceptor bead leading to the emission of light with wavelength varying between 520 and 620 nm. The singlet oxygen molecule goes undetected if there is no acceptor bead present within the range of 200 nm [33]. The beads used in this assay are 250 nm diameter, which is much smaller than the beads used in SPA and FMAT. This property serves advantageously to avoid clogging in liquid handling devices [34].

1.2.7 Flow Cytometry

This technique sequentially sorts or counts microscopic particles suspended in a fluid by means of optical signals using fluorescence. These particles may be cells or cell sized beads of polystyrene/latex or dextran microspheres with a diameter in the micrometer range. Flow Cytometry requires that one of the interacting partners among receptor and ligand is immobilized on the bead, and the other is provided with a fluorescent tag for the quantification of receptor–ligand binding. Two lasers are used to identify the bead and quantify the fluorescence associated with the immobilized partners [35]. It can measure and quantify molecular interaction in a sensitive and precise manner, combined with a high throughput of samples, multiplexing and the possibility of kinetic analyses. Although these are deemed to be the advantages of flow Cytometry technique but on the other hand, it remains difficult to setup such assays which require highly skilled manpower and expensive setups.

1.2.8 Fluorescence Correlation Spectroscopy (FCS)

Fluorescence correlation spectroscopy is a homogeneous assay technique that determines receptor–ligand binding by measuring intensity fluctuations consequent to the differences in diffusion rate of individual dye-labelled ligands free in solution or bound to a high-molecular-weight receptor. Binding of the ligand molecule to a receptor molecule results in an increase in the mass and hence in a reduced rate of diffusion, which leads to increased average time spent in the irradiated volume. This results in multiple photons emission from the labelled ligand/complex within a given time. As these photons are emitted from the same labelled ligand/complex moving in the fluid volume due to Brownian motion, they are correlated in time. The average correlation time is a measure of the fraction of ligand that is bound to the receptor and will be at its maximum if the fluorescently labelled ligand saturates the receptor. Since fluctuations of the fluorescent signal are governed by the number and quantum yield of the fluorescent molecules, it is necessary to reduce the irradiated volume such that individual molecules can be measured. This is achieved by using diffraction-limited laser beams and confocal detection optics, in combination with pinholes in the image plane, generating observation volumes in the order of femtoliters (μm^3) [36]. Laser systems used in FCS are based on; Helium–Neon laser with an excitation wavelength of 543 nm and 633 nm; Argon laser with an excitation wavelength of 488 and 514 nm and Argon–Krypton lasers with an excitation wavelength of 568 and 647 nm.

FCS displays an advantage to study receptor–ligand interactions at the molecular level in a living cell as compared to the traditional assay techniques which require extraction of a receptor from its natural membrane environment. Another advantage of FCS is that there is no need to immobilize a ligand or receptor as in

the case of bead-based assays and biosensors. FCS is suitable for producing high throughput screening with and an additional advantage of a microliter of sample volume. On the other hand, it requires expensive setup in a laboratory environment with highly skilled workforce and extremely expensive state of the art optical and analytical equipment that is termed as a disadvantage of the technique.

1.3 Immunoassay

An **immunoassay** is a type of biochemical testing that is used to measure the concentration of a particular substance in a solution containing a complex mixture of substances. Such testing uses the ability of a very limited group of molecules called antigen to bind with an antibody. The binding between two requires high specificity just like a lock and key. The degree to which the analytical reagent can bind to its specific partner determines the particular nature of the assay. The analytical reagents associated with a detectable label are required to perform immunoassay. These labels used may be radioactive, phosphorescent, fluorescent, and chemiluminescent dyes. In addition to the binding specificity, a transducer is used to produce a measurable signal in response to a particular binding of the antibody–antigen pair. Four main types of transducer have been used in immunoassay technology. The electrochemical transducer (potentiometric, amperometric, conductimetric) detect changes in electrical properties of the sample. Heat transducer (calorimetric) detect changes in temperature of the sample. The mass transducer [piezoelectric, Surface Acoustic Wave (SAW)]. The optical transducer (luminescent, fluorescent, reflective, refractive, ellipsometric, Surface Plasmon Resonance (SPR) Nuclear Magnetic Resonance (NMR) and waveguide) detect the change in frequency, phase shift and wave properties of the acoustic or electromagnetic radiation carrying the information after reflecting or refracting from the sample.

All immunoassays require reference to a calibrator for interpretation of the signal produced as a result of the procedure. The comparison mimics the characteristics of the sample medium. In the case of qualitative immunoassays, the calibrator consists of reference with no analyte present. It is called negative sample whereas, a positive sample is one which has the lowest concentration of the detectable analyte. Quantitative assays make use of additional calibrators that contain known analyte concentrations. The assay response of a real sample compared to the assay responses by the calibrators produces a signal. The strength of this signal determines the presence or concentration of an analyte in the sample.

Immunosensor is a device operating on the principles of solid-phase immunoassay, with either antibody or antigen immobilized on the sensor surface. These are used to detect an extensive range of analytes like environment pollutant such as pesticides, bacteria, drugs, and medical diagnostic markers such as hormones (steroids and pituitary hormones). Advantages like, the absence of labelling requirements and ability to investigate the reaction dynamics of the antibody–antigen binding has provided these devices a leading edge over the conventional assay

techniques. The fundamental principles of immunosensors with respect to the applied transducer systems are discussed as follows.

The development of optical techniques for monitoring of minute changes in light scatter, refractive index, phase change and absorption has provided a promising platform for the development of this technique. Optical transducers based on reflectance, ellipsometry, surface plasmon resonance and optical fiber waveguide have all been briefly described here.

1.3.1 Surface Plasmon Resonance (SPR)

This method used for the detection of antibody–antigen interaction does not require labelling. The SPR device consists of a sensor chip, a flow cell, a light source, a prism and a detector that is positioned at a fixed angle. The sensor's surface consists of a thin gold layer (~ 50 nm) fixed onto a glass surface with an interaction layer e.g. BSA-biotin. The carboxylic acid group on this layer can be activated to immobilize either the receptor/antibody, or the ligand/antigen covalently [37].

SPR measures changes in refractive index for a resonance angle at which polarized light is reflected from a surface. This change is related to the change in mass of the analyte or layer thickness. [38, 39]. Specific ligands can be immobilized on the upper surface of the device (sensor surface), to interact directly with the biomolecules in the sample. SPR technology is based on the excitation of the surface electrons of the metal (gold) which behave differently as compared to the bulk electrons since they can oscillate more freely in comparison to the bulk electrons. When excited, these electrons, also termed as surface plasmon, oscillate at a different frequency from that in the bulk of the metal film, absorb light photons and generate an evanescent wave. In SPR system, polarized light is directed in one plane into the prism and gets totally internally reflected due to the difference of refractive indices of prism and metal surface from the metal-glass interface. At the resonance angle, SPR is initiated; the absorption of light energy by the surface plasmon causes a sharp decrease in the intensity of the reflected light. The evanescent wave propagates into the metal layer which allows it to sense the metal-sample interface. The resonance angle is determined by the wavelength, polarization and refractive indices of the prism, metal and a sample layer of the system. Changes in refractive index take place when biomolecules attach to the ligand immobilized at the sensor surface. Consequent to that the resonance angle, at which drop of intensity is observed, changes. Continuous monitoring of the reflected light intensity provides a direct profile of the changes in the refractive index at the sensor surface and hence a real-time analysis of the binding events at the sensor surface is obtained. The basic operating principle of SPR is shown in Fig. 1.5.

As surface plasmon resonance is dependent on changes in mass, it is advantageous to attach the molecule to the lowest molecular weight to the surface and

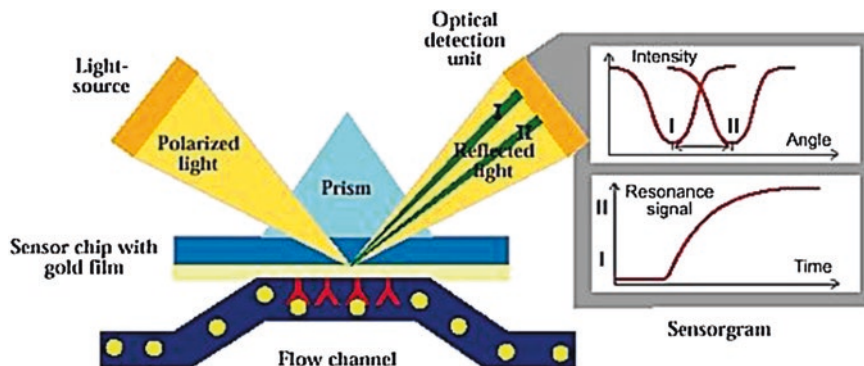


Fig. 1.5 Detection principle of SPR technique [38]

measure binding of the higher molecular weight partner. Nevertheless, due to the possible difficulties of immobilizing low molecular weight ligands/antigen (e.g. loss in binding affinity), it might be necessary to attach the high-molecular weight receptor/antibody to the surface and work with a smaller signal [40]. The latter approach has the benefit of requiring less receptor [41], but has a significant limitation in the form of denaturation of the immobilized receptor may occur upon repeated use. The sensitivity of the assay can be increased by immobilizing the ligand/antigen on the sensor surface, thereby, generating a large signal due to binding higher molecular mass receptor/antibody as described by Kroger et al. [42].

The main advantage of SPR is thus the monitoring of molecular interactions in real-time without the use of labels. The major limitation is that one of the binding partners needs to be immobilized.

1.3.2 Total Internal Reflection Fluorescence (TIRF)

Total internal reflection fluorescence detection technique is based on the same principle corresponding to SPR. The difference between two is that SPR is a label-free technique whereas TIRF relies on the binding of a fluorescent-labeled ligand to an immobilized receptor on the sensor surface. The information carrying signal in TIRF is not dependent on the mass of the ligand, but it makes use of the sensitivity of fluorescence. The evanescent wave produced due to the excitation of the surface plasmon by polarized light causes excitation in the fluorescent labels present close to the sensor surface (~ 100 nm). The change in the intensity of the incident light is measured. Since only those fluorescent ligands that are near the surface and thus bound to the receptors are excited by the evanescent wave, the signal is not affected by the fluorescent ligand in the buffer solution [43–45]. TIRF

has been used to measure estrus cycle in dairy cows by measuring the progesterone level in the bovine milk [46].

1.3.3 Ellipsometry

Ellipsometry is a sensitive optical technique to determine surfaces and thin films properties. It is used to study the binding of proteins to surfaces [47]. If a known oriented linearly polarized light reflects from a surface at an oblique angle, the polarization of the reflected light changes to elliptically polarized. The angle of incidence, the direction of polarization of light, and the properties of the incident surface determine the orientation and shape of the ellipse. The polarization of the reflected light can be measured with a quarter-wave plate followed by an analyser; the orientations of the quarter-wave plate and the analyser are varied until no light passes through the analyser. By measuring these orientations and the direction of polarization of incident light, relative phase change Δ , and the relative amplitude change ψ can be evaluated. These properties vary when a molecule is adsorbed to the surface, and the new readings can be interpreted as a change in the refractive index and coating thickness of the sensor surface. This leads to the calculation of the concentration of the bound analyte. Isoscope[®] ellipsometer has been used to study receptor-ligand interactions. [48].

1.3.4 Nuclear Magnetic Resonance Spectroscopy

Nuclear magnetic resonance (NMR) is a physical phenomenon which is based on the absorption and re-emission of electromagnetic radiation of a magnetic nucleus in the presence of a strong magnetic field. The EM energy is absorbed, when the frequency of the applied electromagnetic field matches the natural frequency of the exposed nucleus, called resonance frequency. The resonance frequency depends on the magnetic field strength and the nuclear magnetic properties of the atom. NMR imaging relies on the observation of magnetic quantum mechanical properties of an atomic nucleus. The resonant frequency of a material varies directly with the strength of the magnetic field applied. Superconductors are used to increase the magnetic field strength to obtain the required resolution of the image.

NMR spectroscopy is used to study the interaction of molecules at the atomic level. It is also widely used to elucidate the structures of chemically synthesized compounds and biomolecules [49]. Functional group analysis, bonding connectivity and orientation, through space connectivity, Molecular Conformations, DNA, peptide and enzyme sequencing and structure are a few other applications of NMR [50].

1.3.5 Amperometric Immunosensors

These devices measure current flowing through the electrolyte in a chemical cell at a constant voltage. The current is produced as a result of the redox reaction at the sensing electrode. The current generated is varies directly with the amount of oxygen or hydrogen peroxide reduced or oxidized at the electrode [51]. The system has the advantage of high sensitivity, linear concentration dependence and high selectivity. However, for intrinsically non-electroactive molecules like proteins cannot be detected by a direct approach that is a demerit of this system. For such molecules, enzymes are incorporated as labels to catalyse redox reactions that facilitate the production of electroactive species that may then be able to be detected by amperometric immunosensors. For example, a multi-analyte amperometric immunosensor has been developed for measuring the human gonadotropin hormone, follicle stimulating hormone and luteinizing hormone achieving low detection limits. The device uses two horseradish peroxidase-labelled antibodies in a ferrocene-medicated system [52].

1.3.6 Conductimetric Immunosensors

Chemical reactions produce or consume ions species and, therefore, alter the overall electrical conductivity of the solution. Sensors designed by immobilizing a suitable enzyme over a set of chemically inert metals electrodes, and by measuring the change in the conductance of a solution containing the analyte of interest, consequent to an applied electric field, are termed as conductimetric immunosensor. For example, when urea is converted to ionic product NH_4^+ by the enzyme urease, the increase in the solution conductance measured is proportional to the concentration of urea in the solution [53]. These sensors face the problem of non-specificity of measurements because the resistance of the solution is determined by migration of all ions present.

1.3.7 Surface Acoustic Wave Immunosensors (SAW)

This technique uses oscillations of piezoelectric crystals at higher frequencies (30–200 MHz), and an acoustic wave is generated by application of an alternating voltage to a pattern of interlaced metal electrodes, known as an interdigital transducer. The high-frequency acoustic signal is detected by another interdigital transducer separated by a small distance. The adsorption of the sample to the crystals slows down the acoustic wave, and the recorded change in velocity is proportional to the analyte concentration. Such devices have successfully been used in specific areas such as environmental gas monitoring [54], chemical detection [55], rapid

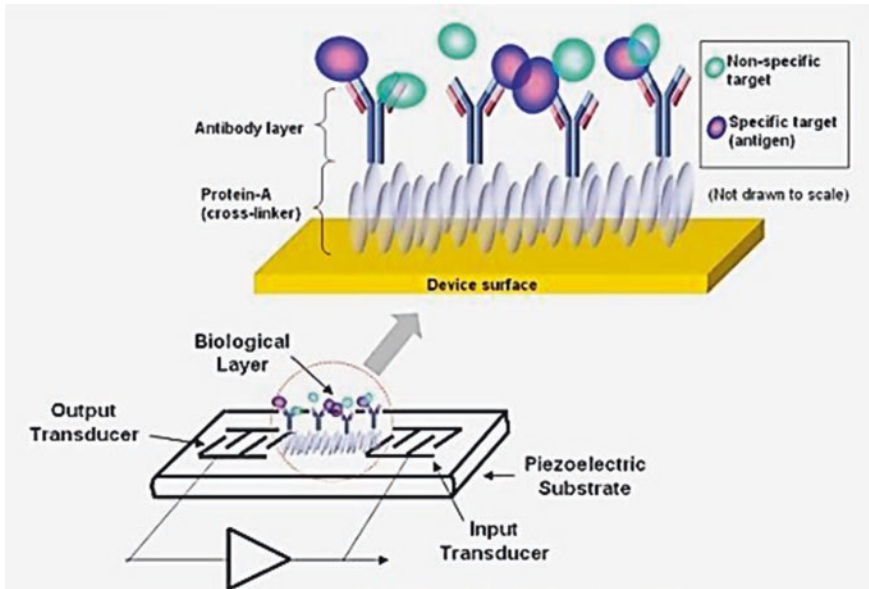


Fig. 1.6 Schematics of a SAW immunosensor [57]

immunoassay of antigen present in the foodstuffs and human IgG measurements [56]. The schematics of a SAW sensing device is shown in Fig. 1.6 [57].

1.3.8 Enzyme-Linked Immunosorbent Assay (ELISA)

It is a biochemical technique used to detect the presence of an antibody or an antigen in a sample. An unknown amount of antigen is immobilized on a microtiter plate by adsorption and detection antibody is added which form a binding with the antigen. The detection antibody can be covalently linked to an enzyme through bio-conjunction. Before each step, the microtiter plate is washed with a mild detergent solution to remove antibodies that remain unbound. An enzymatic substrate is added to develop the plate to observe a visible signal, most commonly a colour change, which indicates the quantity of antigen in the sample. ELISA is used as a diagnostic tool in medicine, plant pathology, biochemical detection, and as quality control in various industries [58].

All the assay techniques and methods discussed in the previous literature survey have their own merits and de-merits. Labelled sensors use immunoassay approach for binding the target molecule that is purely laboratory-based technique involving expensive, time-consuming and hi-tech laboratory protocols, hence, rendering impossible real-time measurements. Sensors for direct, label-free quantification of analytes are attractive to researchers for a number of reasons like direct

Table 1.2 Advantages and disadvantages of contemporary techniques used for biochemical analytes

Assay format	Detection principle	Advantages	Disadvantages
Filtration assay	Radioactive	Labelling steps do not change affinity	Requires separation, radioactivity, medium throughput
SPA/flash plate	Energy transfer	Mix-n-read, affinity does not change by labelling, high-throughput	Radioactivity, receptor immobilization, low sensitivity
Filtration assay non-radioactive	Fluorescence	Fluorescent	Require separation, labelling change affinity, medium-throughput, fluorescence interference
FRET	Energy transfer	Mix-n-read, fluorescent	Dual labelling, distance constraints, correct dipole orientation, background noise
FP	Light polarization	Mix-n-read, one label, ratiometric measurement, ease of automation, facile to miniaturize	Labelling alters affinity, requires suitable ligands
FMAT	Single cell measurement	Mix-n-read, multiplexing, minimal background noise, miniaturization	Requires receptor immobilization, high assay variation, expensive setup
AlphaScreen™	Energy transfer	Mix-n-read, time-resolved	Uses bead for donor and acceptor, receptor immobilization
Flow cytometry	Single cell measurement	Mix-n-read, sensitive, minimal background noise, high throughput, multiplexing	Requires fluorescent labels and immobilization of receptor and ligand, limitation in sample handling
FCS	Diffusion mediated intensity fluctuations	Molecular, homogenous, min. background noise, real time, time resolved, miniaturization	Limited accessibility, complex instrumentation, stringent optical requirements
SPR	Refractive index	No labelling, sensitive, real-time, no interference, automation	Receptor or ligand immobilization, sensitivity depends on molecular weight of analyte, high cost, high protein density, correct orientation
TIRF	Refractive index	Real-time, high sensitivity, combined with micro fluids, surface specificity	Receptor immobilization, labelling
Microarray	Optical intensity change	Multiplexing, real-time	Labelling and immobilization of receptor and ligand

detection of analytes with minimal or no sample preparation, cost effective, simple and real-time. These involve optical, mass-sensitive and electrochemical detection routes for measurement of an analyte in the bulk sample. Optical sensors are the most studied, but the electrochemical sensors are relatively more sensitive and display comparatively lower detection limit capabilities with a requirement of least complicated support instrumentation. On the other hand, optical and mass-sensitive techniques claim state-of-the-art electronics and bulky instrumentation for interpretation of optical and mass variation data into clear information. Table 1.2 provides the reader a crisp and comprehensive comparison of the contemporary techniques and methodologies that are applied most frequently in today's world.

1.4 Conclusions

Almost all contemporary analytical techniques described here are highly sensitive due to the requirement of measurement of trace levels of EDCs present in food and beverage samples. Table 1.2 compares the advantages and disadvantages of the most applied biochemical sensing techniques. Unfortunately, these are time-consuming, expensive, complicated, produce laboratory waste, need the expertise of highly trained professionals in addition to the submission of samples to laboratories, worth millions of dollars. Blood and urine are the most common matrices used for biomonitoring of EDCs in the human body, but the results of these biomonitors do not provide the complete picture of EDCs intake, rather just provides the quantity of metabolites excreted, losing information about the amount of phthalates that have become the body burden. Therefore, it is necessary to have a rapid assay which may detect the quantity of phthalates present in food and beverages as initial intake via the oral route which is deemed to be the biggest source of human phthalate exposure due to the extensive use of plastics in our everyday lifestyle. The requirement of instant screening of a batch of products manufactured at an industrial setup still requires the attention of the researchers to devise an assay which may be simple enough to be handled with minimal training needs and does not involve bulky and expensive support electronics. The objective of this research is to develop a low-cost real-time testing system which could readily be installed in an automated setup. Furthermore, a portable, low-cost sensing system is envisaged which can be used to quantify the amount of phthalates in consumer food products, rapidly.

References

1. T. Schettler, Human exposure to phthalates via consumer products. *Int. J. Androl.* **29**(1), 134–139 (2005)
2. P. Montuori, E. Jover, M. Morgantini et al., Assessing human exposure to phthalic acid and phthalate esters from mineral water stored in polyethylene terephthalate and glass bottles. *Food Addit. Contam.* **25**(4), 511–518 (2008)

3. R. Green, R. Hauser, A.M. Calafat et al., Use of di (2-ethylhexyl) phthalate-containing medical products and urinary levels of mono (2-ethylhexyl) phthalate in neonatal intensive care unit infants. *Environ. Health Perspect.* **113**(9), 1222 (2005)
4. P. Foster, Disruption of reproductive development in male rat offspring following in utero exposure to phthalate esters. *Int. J. Androl.* **29**(1), 140–147 (2006)
5. J.D. Meeker, A.M. Calafat, R. Hauser, Urinary metabolites of di (2-ethylhexyl) phthalate are associated with decreased steroid hormone levels in adult men. *J. Androl.* **30**(3), 287 (2009)
6. J.A. Colacino, T.R. Harris, A. Schechter, Dietary intake is associated with phthalate body burden in a nationally representative sample. *Environ. Health Perspect.* **118**(7), 998 (2010)
7. L. López-Carrillo, R.U. Hernández-Ramírez, A.M. Calafat et al., Exposure to phthalates and breast cancer risk in northern Mexico. *Environ. Health Perspect.* **118**(4), 539 (2010)
8. J.A. Colacino, A.S. Soliman, A.M. Calafat et al., Exposure to phthalates among premenstrual girls from rural and urban Gharbiah, Egypt: a pilot exposure assessment study. *Environ. Health* **10**(1), 40 (2011)
9. M.R. Lee, F.Y. Lai, J. Dou et al., Determination of trace leaching phthalate esters in water and urine from plastic containers by solid-phase microextraction and gas chromatography-mass spectrometry. *Anal. Lett.* **44**(4), 676–686 (2011)
10. R. Sendón, A. Sanches-Silva, J. Bustos et al., Detection of migration of phthalates from agglomerated cork stoppers using HPLC-MS/MS. *J. Sep. Sci.* **35**(10–11), 1319–1326 (2012)
11. Z. Guo, D. Wei, M. Wang et al., Determination of six phthalic acid esters in orange juice packaged by PVC bottle using SPE and HPLC-UV: application to the migration study. *J. Chromatogr. Sci.* **48**(9), 760–765 (2010)
12. WHO, *WHO Guidelines for drinking-water quality, fourth edition*, World Health Organization (2011), http://www.who.int/water_sanitation_health/publications/2011/dwq_guidelines/en/. ISBN: 978-92-4-154815-1
13. X.L. Cao, Determination of phthalates and adipate in bottled water by headspace solid-phase microextraction and gas chromatography/mass spectrometry. *J. Chromatogr. A* **1178**(1–2), 231–238 (2008)
14. J. Li, Y. Cai, Y. Shi et al., Analysis of phthalates via HPLC-UV in environmental water samples after concentration by solid-phase extraction using ionic liquid mixed hemimicelles. *Talanta* **74**(4), 498–504 (2008)
15. F. Tamayo, E. Turiel, A. Martín-Esteban, Molecularly imprinted polymers for solid-phase extraction and solid-phase microextraction: Recent developments and future trends. *J. Chromatogr. A* **1152**(1), 32–40 (2007)
16. J.-P. Lai, M.-L. Yang, R. Niessner et al., Molecularly imprinted microspheres and nanospheres for di (2-ethylhexyl) phthalate prepared by precipitation polymerization. *Anal. Bioanal. Chem.* **389**(2), 405–412 (2007)
17. P. Qi, J. Wang, Y. Li et al., Molecularly imprinted solid-phase extraction coupled with HPLC for the selective determination of monobutyl phthalate in bottled water. *J. Sep. Sci.* **34**(19), 2712–2718 (2011)
18. M. Wagner, J. Oehlmann, Endocrine disruptors in bottled mineral water: total estrogenic burden and migration from plastic bottles. *Environ. Sci. Pollut. Res.* **16**(3), 278–286 (2009)
19. C. Giam, H. Chan, G. Neff, Rapid and inexpensive method for detection of polychlorinated biphenyls and phthalates in air. *Anal. Chem.* **47**(13), 2319–2320 (1975)
20. D.A. Vignali, Multiplexed particle-based flow cytometric assays. *J. Immunol. Methods* **243**(1), 243–255 (2000)
21. J. Šmisterová, K. Ensing, R. De Zeeuw, Methodological aspects of quantitative receptor assays. *J. Pharm. Biomed. Anal.* **12**(6), 723–745 (1994)
22. R. Nebel, On-farm milk progesterone tests. *J. Dairy Sci.* **71**(6), 1682–1690 (1988)
23. N.D. Cook, Scintillation proximity assay: a versatile high-throughput screening technology. *Drug Discov. Today* **1**(7), 287–294 (1996)

24. T. Jonsson, C.D. Waldburger, R.T. Sauer, Nonlinear free energy relationships in Arc repressor unfolding imply the existence of unstable, native-like folding intermediates. *Biochemistry* **35**(15), 4795–4802 (1996)
25. H.C. Ishikawa-Ankerhold, R. Ankerhold, G.P. Drummen, Advanced fluorescence microscopy techniques—frap, flip, flap, fret and flim. *Molecules* **17**(4), 4047–4132 (2012)
26. B.S. Watson, T.L. Hazlett, J.F. Eccleston et al., Macromolecular arrangement in the aminoacyl-tRNA. cnddot. elongation factor Tu. cnddot. GTP ternary complex. A fluorescence energy transfer study. *Biochemistry* **34**(24), 7904–7912 (1995)
27. W. Berger, H. Prinz, J. Striessnig et al., Complex molecular mechanism for dihydropyridine binding to L-type Ca²⁺ channels as revealed by fluorescence resonance energy transfer. *Biochemistry* **33**(39), 11875–11883 (1994)
28. P.L. Khanna, E.F. Ullman, 4', 5'-Dimethoxy-6-carboxyfluorescein: A novel dipole-dipole coupled fluorescence energy transfer acceptor useful for fluorescence immunoassays. *Anal. Biochem.* **108**(1), 156–161 (1980)
29. R.M. Clegg, A. Murchie, D. Lilley, The solution structure of the four-way DNA junction at low-salt conditions: a fluorescence resonance energy transfer analysis. *Biophys. J.* **66**(1), 99–109 (1994)
30. A. Gagne, P. Banks, S. Hurt, Use of fluorescence polarization detection for the measurement of Fluopeptide™ binding to G protein-coupled receptors. *J. Recept. Signal Transduct.* **22**(1–4), 333–343 (2002)
31. T.J. Kowski, J.J. Wu, Fluorescence polarization is a useful technology for reagent reduction in assay miniaturization. *Comb. Chem. High Throughput Screening* **3**(5), 437–444 (2000)
32. P. Zuck, Z. Lao, S. Skwish et al., Ligand-receptor binding measured by laser-scanning imaging. *Proc. Natl. Acad. Sci.* **96**(20), 11122–11127 (1999)
33. E.F. Ullman, H. Kirakossian, A. Switchenko et al., Luminescent oxygen channeling assay (LOCI): sensitive, broadly applicable homogeneous immunoassay method. *Clin. Chem.* **42**(9), 1518–1526 (1996)
34. M.B. Meza, Bead-based HTS applications in drug discovery. *Drug Discov. Today* **5**, 38–41 (2000)
35. B. Bohn, Flow cytometry: a novel approach for the quantitative analysis of receptor-ligand interactions on surfaces of living cells. *Mol. Cell. Endocrinol.* **20**(1), 1–15 (1980)
36. M. Eigen, R. Rigler, Sorting single molecules: application to diagnostics and evolutionary biotechnology. *Proc. Natl. Acad. Sci.* **91**(13), 5740–5747 (1994)
37. U. Jönsson, L. Fägerstam, S. Löfas et al., *Introducing a Biosensor Based Technology for Real-Time Biospecific Interaction Analysis*, pp. 19–26
38. U. Jönsson, L. Fägerstam, B. Ivarsson et al., Real-time biospecific interaction analysis using surface plasmon resonance and a sensor chip technology. *Biotechniques* **11**(5), 620–627 (1991)
39. S. Subrahmanyam, S.A. Piletsky, A.P. Turner, Application of natural receptors in sensors and assays. *Anal. Chem.* **74**(16), 3942–3951 (2002)
40. W.D. Wilson, Analyzing biomolecular interactions. *Science* **295**(5562), 2103–2105 (2002)
41. J.E. Gestwicki, H.V. Hsieh, J.B. Pitner, Using receptor conformational change to detect low molecular weight analytes by surface plasmon resonance. *Anal. Chem.* **73**(23), 5732–5737 (2001)
42. D. Kröger, F. Hucho, H. Vogel, Ligand binding to nicotinic acetylcholine receptor investigated by surface plasmon resonance. *Anal. Chem.* **71**(15), 3157–3165 (1999)
43. E.L. Schmid, A.-P. Tairi, R. Hovius et al., Screening ligands for membrane protein receptors by total internal reflection fluorescence: the 5-HT₃ serotonin receptor. *Anal. Chem.* **70**(7), 1331–1338 (1998)
44. D. Axelrod, T.P. Burghardt, N.L. Thompson, Total internal reflection fluorescence. *Ann. Rev. Biophys. Bioeng.* **13**(1), 247–268 (1984)
45. D. Axelrod, E.H. Hellen, R.M. Fulbright, Total internal reflection fluorescence, in *Topics in Fluorescence Spectroscopy* (Springer, 2002), pp. 289–343

46. N.D. Käppel, F. Pröll, G. Gauglitz, Development of a TIRF-based biosensor for sensitive detection of progesterone in bovine milk. *Biosens. Bioelectron.* **22**(9), 2295–2300 (2007)
47. U. Jönsson, M. Malmqvist, I. Ronnberg, Adsorption of immunoglobulin G, protein A, and fibronectin in the submonolayer region evaluated by a combined study of ellipsometry and radiotracer techniques. *J. Colloid Interface Sci.* **103**(2), 360–372 (1985)
48. M. Stenberg, H. Nygren, A receptor-ligand reaction studied by a novel analytical tool—the isoscope ellipsometer. *Anal. Biochem.* **127**(1), 183–192 (1982)
49. B. Meyer, T. Peters, NMR spectroscopy techniques for screening and identifying ligand binding to protein receptors. *Angew. Chem. Int. Ed.* **42**(8), 864–890 (2003)
50. C.A. Lepre, J.M. Moore, J.W. Peng, Theory and applications of NMR-based screening in pharmaceutical research. *Chem. Rev.* **104**(8), 3641–3676 (2004)
51. B. R. Eggins, *Chemical sensors and biosensors*: John Wiley & Sons, 2008
52. D. Pritchard, H. Morgan, J. Cooper, Simultaneous determination of follicle stimulating hormone and luteinising hormone using a multianalyte immunosensor. *Anal. Chim. Acta* **310**(2), 251–256 (1995)
53. L. Watson, P. Maynard, D. Cullen et al., A microelectronic conductimetric biosensor. *Biosensors* **3**(2), 101–115 (1988)
54. C.G. Fox, J.F. Alder, Surface acoustic wave sensors for atmospheric gas monitoring. A review. *Analyst* **114**(9), 997–1004 (1989)
55. M. Nieuwenhuizen, A. Nederlof, M. Vellekoop et al., Preliminary results with a silicon-based surface acoustic wave chemical sensor for NO₂. *Sens. Actuators* **19**(4), 385–392 (1989)
56. E. Gizeli, N.J. Goddard, C.R. Lowe et al., A love plate biosensor utilising a polymer layer. *Sens. Actuators B: Chem.* **6**(1), 131–137 (1992)
57. P.J. Edmonson, W.D. Hunt, D.D. Stubbs et al., Analogies between digital radio and chemical orthogonality as a method for enhanced analysis of molecular recognition events. *Int. J. Mol. Sci.* **9**(2), 154–168 (2008)
58. A. Voller, D.E. Bidwell, A. Bartlett, in *The enzyme linked immunosorbent assay (ELISA). A guide with abstracts of microplate applications* (Dynatech Europe, Borough House, Rue du Pre., 1979)

Chapter 2

Impedance Spectroscopy and Experimental Setup

2.1 Introduction

The objective of this chapter is to introduce the measuring instruments and software programs used for the experimental setup. It provides the reader a detailed insight of, electrochemical impedance spectroscopy basics and data representation along with highlighting the methodology of measurement data collection. It explains all the hardware and software used to collect the impedance data and the models involved in analyzing the acquired information. It also describes the interfacing of the measuring instruments with LabVIEW program to obtain a stand-alone automated measurement system. It provides an account of the significant applications of impedance spectroscopy method for characterization of sensors and material under test (MUT). The objectives are to measure and characterize the developed sensors according to EIS models and methods. Mathematical methods like complex non-linear least square curve fitting were used to deduce equivalent circuit to the electrochemical cell under test. The parameters obtained from the measuring instruments are frequency, f , impedance, Z and phase angle. Mathematical methods used to interpret these into real and imaginary parts in the complex plane for analysis of impedance characteristics are also discussed.

2.2 Electrochemical Impedance Spectroscopy

Electrochemical Impedance Spectroscopy (EIS) has seen a huge boost in popularity in recent time due to its extraordinary sensitivity. It is used to evaluate electrical properties of materials and their interfaces with surface-modified electrodes [1]. This method has been widely used to study of electrochemistry [2, 3], biomedical applications [4, 5], material science [6] and others. J. Ross McDonald in [7] describes the EIS as a part of Impedance measurement using AC polarography involving electrochemical reactions. The response of an electrochemical cell to a low amplitude sinusoidal perturbation as a function of frequency and has been

reported to estimate the dielectric properties of milk [8], meat inspection [9], quality testing in leather [10], Saxophone reed inspection [11], detection of contaminated seafood with marine biotoxin [12], food endo-toxins [12–16], evaluate electrical properties of drinks, and water [17]. EIS involves measurements and analysis of materials involving ionic conduction in solid and liquid electrolytes. Ionically conducting glasses and polymers, fused salts, and nonstoichiometric ionically bonded single crystals have been used for impedance measurements where conduction can involve motion of ion vacancies and interstitials. EIS is also conducted to study of fuel cells, rechargeable batteries, and corrosion. Another category of IS applies to dielectric materials: solid or liquid non-conductors whose electrical characteristics involve dipolar rotation, and to materials with predominantly electronic conduction [18]. System Impedance may be measured using various techniques. The most cited impedance measurement techniques are given as follows.

2.2.1 AC Bridges

This is the oldest of all the techniques initially used for the measurement of double-layer parameters, principally of the hanging mercury drop electrode. It has also been used to measure the electrode impedance in a faradaic reaction to evaluate the dynamic processes at the electrode. Although this method is slow, yet provides a magnificent precision of measurements.

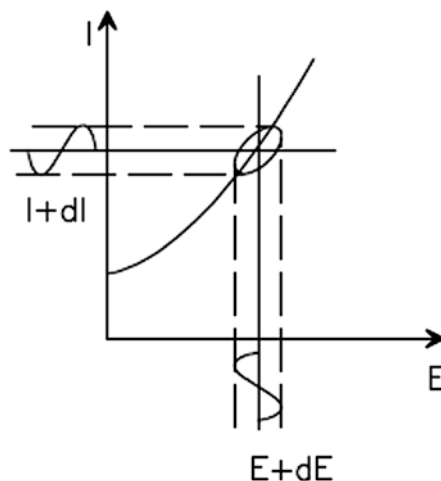
2.2.2 Lissajous Curves

Formation of elliptical figures as a result of the simultaneous application of the applied AC voltage and resulting AC current to a twin beam oscilloscope is called Lissajous curves. Analyzes of Lissajous curves produced on twin channel oscilloscope screens was used to perform impedance measurements and had been an accepted method for impedance spectroscopy prior to the advent of modern EIS instrumentation. The measurement time involved in using this technique (often up to many hours) is long enough for a chemical cell to cause drift in its system parameters. The cell can change through adsorption of impurities, oxidations, degradations, temperature variations, etc. These curves have been used to determine the impedance, but frequency limitations and sensitivity to noise has limited the use of this technique. Figure 2.1 shows the formation of Lissajous figures as a consequence of two out of phase signals.

2.2.3 Fast Fourier Transforms (FFT)

The Fast Fourier Transforms is a mathematical method to evaluate the system impedance. Taking the Fourier transform of the perturbation signal in time domain

Fig. 2.1 Formation of Lissajous figure



and generation of corresponding frequency domain data using a computerized algorithm is referred as FFT. FFT provides a fast and efficient algorithm for computation of the Fourier transforms. In practice, only limited length data is transformed, causing the broadening of the computer frequency spectrum, commonly called 'leakage'. Another problem called 'aliasing' is linked with the presence of the frequencies larger than one-half of the time domain sampling frequency.

2.2.4 Phase Sensitive Detections (PSD)

Phase sensitive detection is used in lock-in amplifiers interfaced with precision potentiostats for system impedance measurements. It contains one time-independent component, depending on the phase difference between two signals and proportional to the amplitude of the measured AC signal. The output signal is applied to a low-pass filter that averages the signal component having frequencies above the cut-off frequency. The disadvantage of the lock-in technique is that it retains the combination of harmonic frequencies present in the input signal.

2.2.5 Frequency Response Analysis (FRA)

Frequency Response Analyzers are hi precision instruments that determine the frequency response of the standardized system. The operation of FRA is based on interpreting correlation of the studied signal with the reference perturbation. The measured signal is multiplied by the sine and cosine of the reference signal of the same frequency and integrated over one time period. Real and imaginary parts of

the measured signal are recovered, strictly rejecting all harmonics. The advantage of the correlation process is a reduction of noise, but it is achieved at the cost of attenuation of the output signal.

Among a number of methods available for impedance measurements, FRA has become a de facto standard for EIS. FRA is a single sine-wave input method in which a small amplitude (5–15 mV) AC sine wave of a given frequency is overlaid on a dc bias potential, applied to the working/excitation electrode and measurement of resulting AC current is made. The system remains pseudo-linear at low-amplitude AC potential. The process is repeated for the desired frequency range, and impedance is computed for five to ten measurements per decade change in frequency. In order to ensure the system linearity, stability, and repeatability, this method is rendered viable only for a stable and reversible system in equilibrium. For this reason, instantaneous impedance measurements are mandatory for non-stationary systems [19]. A non-linear system will contain harmonics (noise) in the measured current response. The drift in the measured system parameters is often observed if the system loses its steady state during the measurement time. The electrochemical cell can change through adsorption, oxidation, coating degradation and temperature variations; to list, these are a few major factors affecting the steady-state condition of the system under test. EIS is used to deduce the changes taking place in the electrochemical system in general and observe the changes in the conductance and capacitance at the sensing surface, interface, and layers, in particular. Next section discusses the fundamental concepts of impedance spectroscopy.

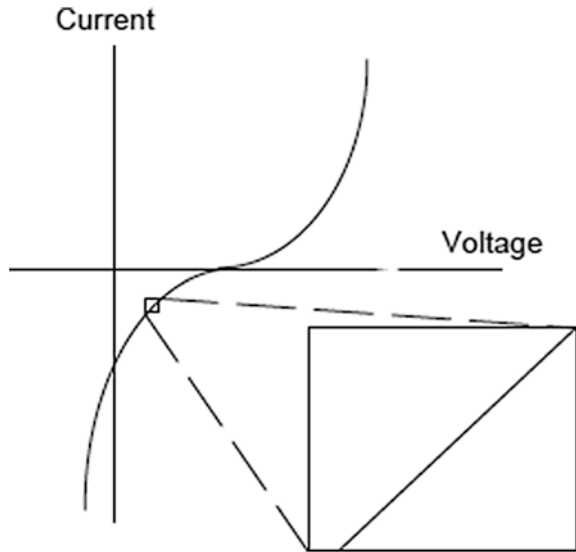
2.2.6 Electrochemical Impedance Spectroscopy; Theory and Analyses

In practice, electrochemical cells are an example of complex non-linear systems. The relationship between current and voltage is highly non-linear. Pseudo-linearity of the electrochemical system is achieved by considering a small linear part of the I-V curve as shown in Fig. 2.2.

Pseudo-linearity is quite useful because; cell's substantial non-linear response to Direct Current (DC) potential is not observable as current is measured at excitation frequency; the measured current is independent of harmonics. If the system is non-linear, the current response of the system will be deformed by the harmonics. The system under test must remain in steady-state throughout the testing time; this is another stringent condition that may affect system linearity. With the advent of hi precision fast FRAs and computing systems, this problem could be catered for. For example, it takes only 88 ms for Hioki 3522-50 to measure impedance, at a particular frequency, without compromising the accuracy of 99.95 % while operating at slow mode; refer to Hioki 3522-50 specification sheet shown in Table 2.1.

In a pseudo-linear electrochemical cell, the impedance can be measured by applying a low-amplitude AC perturbation, E_t , and measuring the phase shift appearing in consequent alternating current flowing through the sensor with

Fig. 2.2 I-V curve for a non-linear system. Pseudo-linearity of the system is achieved by considering a small part of the curve



reference to the applied signal. The magnitude of the occurring phase shift depends on the impedance offered to the electron flow by nature of the electrolyte, diffusion, electrode kinetics and chemical reactions happening inside the cell. Figure 2.3 shows a phase shift θ in the received, current signal with reference to the applied potential perturbation.

Impedance (Z) is a measure of the circuit characteristics to impede the flow of electrons through the circuit, measured in Ohm when exposed to periodic electrical perturbations. The reciprocal of impedance is called admittance, denoted by Y and measured in Siemens (S). Mathematically, impedance is expressed as a complex number comprising of resistance and reactance. Resistance is a static property of the system and is independent of the incident Alternating Current (AC) frequency. It is represented by the real part of the compound number, denoted as R_e , Z_{real} , or Z' . On the other hand, reactance is purely frequency dependent and appears in capacitors and inductors consequent to the applied AC frequency. Reactance is represented by the imaginary part of the complex impedance and is symbolized by R_{im} , X_c or Z_c'' for capacitive reactance and X_L or Z_L'' for inductive reactance, respectively. The basic Ohm's law in Eq. 2.1 defines the resistance R in term potential, V , and current I as;

$$R = \frac{V}{I} \quad (2.1)$$

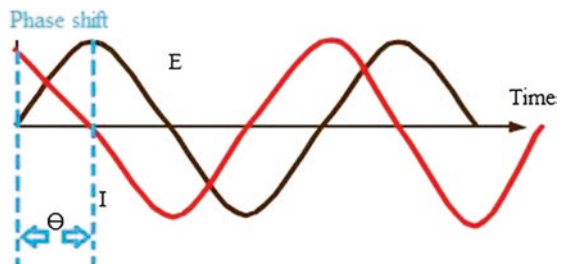
whereas, Ohm's law for alternating current defines impedance Z in terms of time-dependent alternating potential E_t , and current I_t as:

$$Z = \frac{E_t}{I_t} \quad (2.2)$$

Table 2.1 Hioki Hi Precision LCR 3522-50 and 3532-50 Specifications

Specifications		
	3522-50	3532-50
Measurement parameters	Z , Y , θ , Rp (DCR), Rs (ESR), G, X, B, Cp, Cs, Lp, Ls, D, Q	Z , Y , θ , Rp, Rs (ESR), G, X, B, Cp, Cs, Lp, Ls, D, Q
Measurement ranges: Z , R, X	10.00 m Ω –200.00 M Ω (depending on measurement frequency and signal levels)	
θ	–180.00° to +180.00°	
C	0.3200 pF–1.0000 F	0.3200 pF–370.00 mF
L	16.000 nH–750.00 kH	
D	0.00001–9.99999	
Q	0.01–999.99	
Y , G, B	5.0000 nS–99.999 S	
Basic accuracy	Z: $\pm 0.08\%$ rdg. $\theta \pm 0.05^\circ$	
Measurement frequency	DC, 1 MHz–100 kHz	42 Hz–5 MHz
Measurement signal levels	10 mV–5 V rms/10 μ A–00 mA rms	
Output impedance	50 Ω	
Display screen	LCD with backlight/99,999 (full 5 digits)	
Measurement time (Typical values for displaying Z)	Fast: 5 ms	Fast: 5 ms
	Normal: 16 ms	Normal: 21 ms
	Slow 1: 88 ms	Slow 1: 72 ms
	Slow 2: 828 ms	Slow 2: 140 ms
Settings in memory	Max. 30 Sets	
Comparator functions	HI/IN/LO settings for two measurement parameters; percentage, $\Delta\%$, or absolute value settings	
DC Bias	External DC bias ± 40 V max. (option)	
External printer	9442 printer (option)	
External interfaces	GP-IB or RS-232C (Options), external I/O for sequencer use	
Power source	100, 120, 220 or 240 V($\pm 10\%$) AC (selectable), 50/60 Hz	
Maximum rated power	40 VA approx	50 VA approx

Fig. 2.3 Phase shift in current I_t as a response to excitation-potential E_t in a linear system



The excitation signal can be expressed as a function of time;

$$E_t = E_0 \sin \omega t \quad (2.3)$$

where E_t is the potential difference at time t , E_0 is the amplitude of the voltage signal at $t = 0$, and ω is the angular frequency given by ($\omega = 2\pi f$) expressed in radians/second and frequency, f , in hertz.

For a linear system, the response signal I_t , has a phase shift, θ , with amplitude of I_0 which can be expressed by:

$$I_t = I_0 \sin(\omega t - \theta) \quad (2.4)$$

An expression in Eq. 2.2 for Ohm's Law can be used to calculate the impedance of the system given by;

$$\begin{aligned} Z &= \frac{E_t}{I_t} = \frac{E_0 \sin \omega t}{I_0 \sin(\omega t - \theta)} \\ Z &= Z_0 \frac{\sin(\omega t)}{\sin(\omega t - \theta)} \end{aligned} \quad (2.5)$$

The impedance, Z , now can be expressed in term of a magnitude of Z_0 and a phase shift, θ . Equation 2.5 can also be expressed in term of Euler's relationship given by;

$$e^{j\theta} = \cos \theta + j \sin \theta \quad (2.6)$$

where $j = \sqrt{-1}$ ('j' is preferred by electrochemists instead of 'i')

The impedance, Z , can be expressed in term of potential, E , and current response, I , given by;

$$E_t = E_0 e^{j\omega t} \quad (2.7)$$

$$I_t = I_0 e^{j(\omega t - \theta)} \quad (2.8)$$

Therefore the impedance, Z ;

$$Z(\omega) = \frac{E_t}{I_t} = \frac{E_0 e^{j\omega t}}{I_0 e^{j(\omega t - \theta)}} = Z_0 e^{j\theta} \quad (2.9)$$

$$Z(\omega) = Z_0 (\cos \theta + j \sin \theta) \quad (2.10)$$

The impedance now is in the form of real part ($Z_0 \cos \theta$) and imaginary part ($Z_0 \sin \theta$) represented as follows:

$$\text{Re}Z = Z' = Z_{\text{real}} = Z_0 \cos \theta \quad (2.11)$$

$$Z'' = Z_{\text{imag}} = Z_0 \sin \theta \quad (2.12)$$

The raw data for all measured frequencies in EIS experiments comprises of the real and imaginary components of potential difference E' and E'' and the real and imaginary components of current I' and I'' respectively. The phase shift (θ) and total impedance (Z) are the two basic parameters calculated out of the raw data using equations given in Table 2.3. For data analysis purpose, the calculated impedance characteristics are expressed as Nyquist plot and Bode plot.

2.2.7 'Nyquist' and 'Bode' Plots for Impedance Data Analysis

Nyquist plot also known as Cole-Cole plot is one of the most critical and popular formats for evaluating electrochemical parameters like electrolytic solution resistance (R_s), electrode polarization resistance (R_p) and double layer capacitance (C_{dl}), etc. These parameters shall be discussed in detail in the following sections. Nyquist plot represents $Z'(\omega)$ and $Z''(\omega)$ in a complex plane. Among several advantages of Nyquist plot; calculation of solution resistance by extrapolating the curve to x-axis; observable effects of solution resistance; emphasis on the series circuit; comparison of the results of two or more separate experiment, are a few major advantages. One major disadvantage of Nyquist plot is that information on frequency is lost which makes the calculation of C_{dl} complicated.

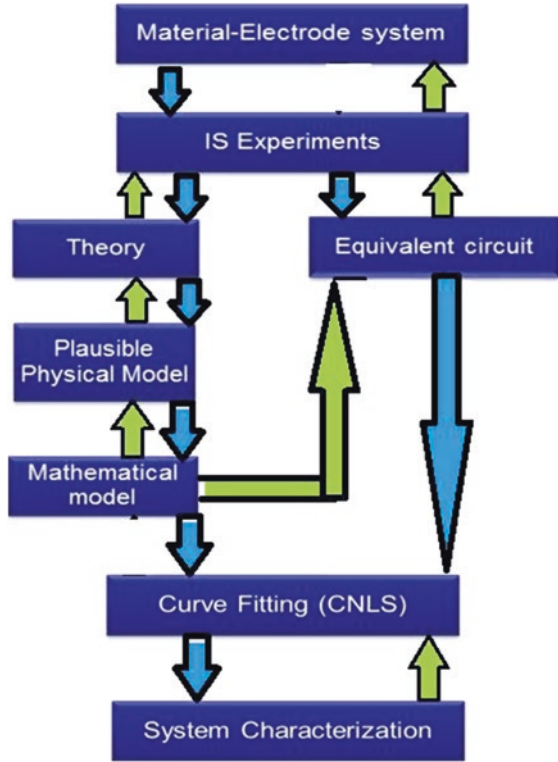
Bode plot represents absolute $Z(\omega)$ and phase angle $\theta(\omega)$ in the frequency domain. Since frequency appears at one of the axes, the effect of the spectrum on the impedance and phase drift is obvious. R_s , R_p , C_{dl} and frequency values, where phase shift $\theta(\omega)$ is maximum/minimum, can be evaluated using Bode plot. This format is desirable when data-scatter prevents adequate fitting of the Nyquist plot. Due to these edges, researchers declare Bode plot as a clearer description of electrochemical cell's frequency-dependant behavior compared to Nyquist plot.

A flow diagram developed by McDonald [18], shown in Fig. 2.4, has been followed by analysis of the electrochemical research on detection of hormones and EDCs presented in this thesis. In order to understand the significance and methods to extract electrochemical cell's parameters, Randle's electrochemical cell model was used to deduce equivalent circuit for the electrochemical cell under test. Complex Nonlinear Least Square (CNLS) curve fitting technique was applied to extract equivalent circuit and component parameters.

2.2.8 Randle's Electrochemical Cell Equivalent Circuit Model

This model was introduced by Randle in 'Discussion of the Faraday Society' in 1947 [20]. The model provides the account of mixed kinetic processes taking

Fig. 2.4 Flow chart for the measurement and characterization of a material-electrode system by EIS [18]



place at the electrode-electrolyte interface. These processes include the fast mass transfer reaction, slow-paced charge transfer reaction, and diffusion processes at the interface. A double layer capacitance is observed at the interface due to the presence of Outer Helmholtz Plane (OHP) and Inner Helmholtz Plane (IHP) at the electrode surface as shown in Fig. 2.5.

The Randle’s cell includes double-layer capacitance, C_{dl} , solution resistance, R_s , charge/electron transfer resistance, R_{ct} and Z_W as shown Fig. 2.6 in the electrochemical cell equivalent circuit deduced in [20].

The expression for the absolute impedance as a function of frequency is given as;

$$Z(\omega) = R_s + \frac{R_{ct}}{1 + \omega^2 R_{ct}^2 C_{dl}^2} - \frac{j\omega R_{ct}^2 C_{dl}}{1 + \omega^2 R_{ct}^2 C_{dl}^2} \quad (2.13)$$

where the real part (Z') is given by;

$$Z'(\omega) = R_s + \frac{R_{ct}}{1 + \omega^2 R_{ct}^2 C_{dl}^2} \quad (2.14)$$

Fig. 2.5 Kinetic processes taking place at electrode-electrolyte interface (Randle's cell model)

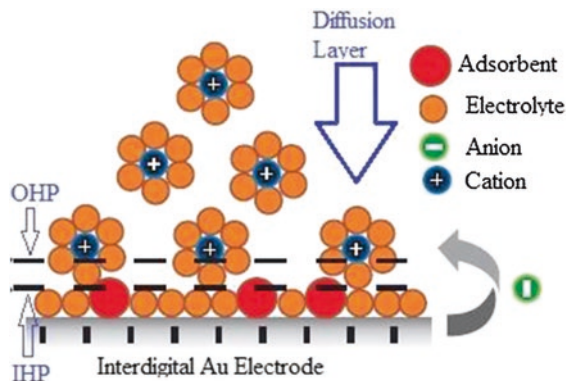
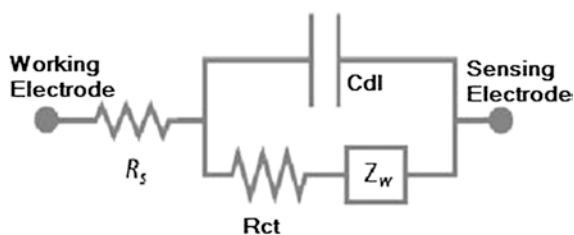


Fig. 2.6 Randle's electrochemical cell equivalent circuit model



and the imaginary part (Z'') is given by;

$$Z''(\omega) = -\frac{\omega R_{ct}^2 C_{dl}}{1 + \omega^2 R_{ct}^2 C_{dl}^2} \quad (2.15)$$

The impedance spectra from the experimental results depicted electrode and electrolyte are related by a mixed kinetic and diffusion processes at the electrode surface which causes a polarization at the interface. R_{ct} is, therefore, sometimes referred as polarization resistance, denoted as R_p , in EIS literature. The value of 'charge transfer resistance R_{ct} , r polarization resistance R_p ' can be calculated from Bode or Nyquist plot. The rate of an electrochemical reaction can be strongly influenced by diffusion of reactants towards, or away from the electrode-electrolyte interface. This situation can exist when the electrode is covered with adsorbed solution components or a selective coating. An addition element called Warburg impedance, Z_w , appears in series with resistance R_{ct} . Mathematically Warburg impedance is given by;

$$Z_w = \frac{\sigma_w}{\sqrt{j\omega}} \quad (2.16)$$

where, σ_w is called Warburg diffusion coefficient. It appears that the characteristic of the Warburg impedance is a straight line with a slope of 45° at a lower frequency. This refers to low-frequency diffusion control because the diffusion

of reactants to the electrode surface is a slow-paced process which can happen at low frequencies only. At higher frequencies, however, the reactants do not have enough time to diffuse. The slope of this line gives Warburg diffusion coefficient. The Nyquist plot in Fig. 2.7 shows the diagonal line of diffusion process (Warburg impedance) at low frequency. The charge transfer process at higher frequency is illustrated by a single time constant semi-circle curve.

The Nyquist plot for a Randle's cell is always a semicircle due to an RC parallel equivalent circuit. The solution resistance R_s also referred as 'uncompensated solution resistance' denoted as ' R_Ω ' in EIS literature can be calculated by high-frequency intercept on the real axis. High-frequency intercept lies closer to the origin of the plot. In Fig. 2.7 it could be read as 25 k Ω . The real axis value at the other (low frequency) intercept is the sum of solution and polarization resistance. The low-frequency intercept could be read by interpolating the semi-circle to the real axis. (In Fig. 2.7 it reads as 325 k Ω). The diameter of the semicircle is, therefore, equal to the polarization resistance (300 k Ω in this case). Figure 2.8 shows the absolute impedance, Z , versus frequency and phase angle in degree with respect to the applied frequency, f in Hz. The two plots combined together are referred as Bode plot. Figure 2.9 shows a combined Bode plot for an electrochemical system with Z (absolute) plotted on the primary y-axis and phase (degree) plotted along the secondary y-axis. Frequency is plotted on the x-axis. This format of Bode plot is a useful alternative to calculating solution resistance (R_s or R_Ω), polarization resistance (R_p or R_{ct}) and C_{dl} . Furthermore, $\log(Z_{abs})$ versus $\log(\omega)$ plot sometimes allow a more efficient extrapolation of the data from higher frequencies.

Fig. 2.7 Nyquist plot for Randle's electrochemical cell model [19]

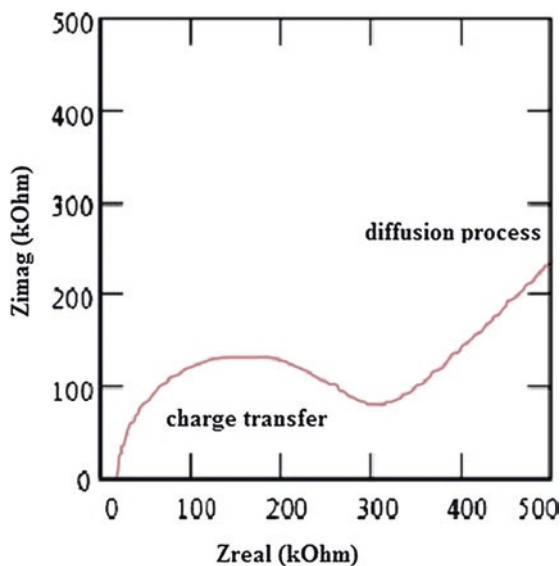


Fig. 2.8 Bode plot for Randle’s electrochemical cell model [19]

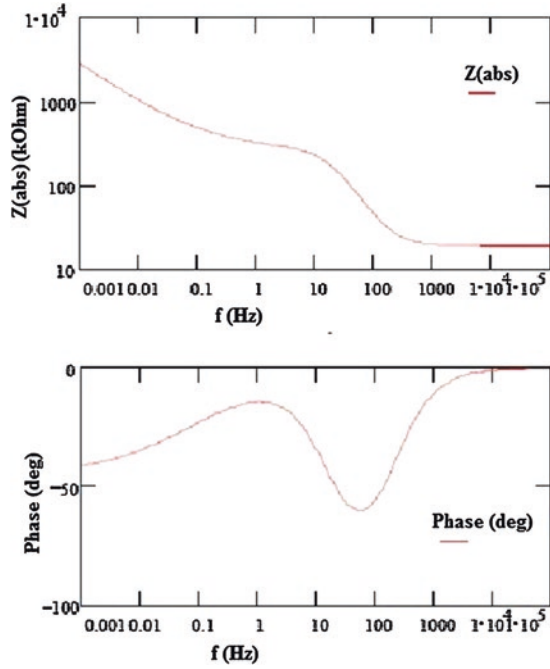
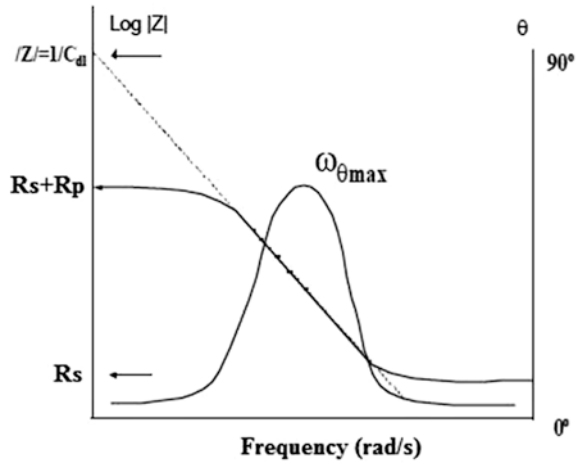


Fig. 2.9 Extraction of intrinsic parameters from bode plot [19]



2.3 Experimental Setup

The experiment setup mainly consisted of Hi-precision Hioki 3522-50 LCR meter, Hioki 4-terminal probe 9140, digital thermometer and humidity tester interfaced through RS232 to a tailor-made LabVIEW program executing on a desktop data



Fig. 2.10 Laboratory test bench with Hioki Hi Precision LCR and data acquisition system

acquisition computer. The temperature, humidity, and inert atmosphere controls were achieved by placing the sensor inside a desiccator, whenever required, to perform the testing under stringent environmental conditions. MicroSuite Laboratory, a research facility available to the School of Engineering and Advanced Technology, Massey University, Palmerston North was used to conduct all set of experiments. Figure 2.10 shows the main experimental setup and the block diagram of the laboratory setup and apparatus used for this research in addition to other in-lab available facilities for heating, cooling, auto envelope, chromatography, microscopy, and spectrophotometry, etc.

2.3.1 Equipment and Instrumentations

The high precision LCR meter Hioki 3522-50 and 3532-50 have been used to obtain test parameters' measurements in order to perform investigation electrochemical impedance spectroscopy from 1 to 5 MHz range as required. The technical specifications of the high-performance set of test equipment LCR meter Hioki 3522-50 and 3532-50 are given in Table 2.1. Figure 2.11 shows the front panel of Hioki high precision LCR meter 3522-50.

2.3.2 Fixture and Test Probe Connections

The standard fixture is a four-wire type Hioki 9261 which can be used for all test frequencies from DC to 5 MHz. Figure 3.3 shows Hioki 9140 4-terminal test probe with crocodile clip termination which can be used for testing in a range of 1 MHz–100 kHz. There are two sets of terminals connecting the sensor to the test



Fig. 2.11 Hioki (Japan) 3522-50 LCR Hi-tester

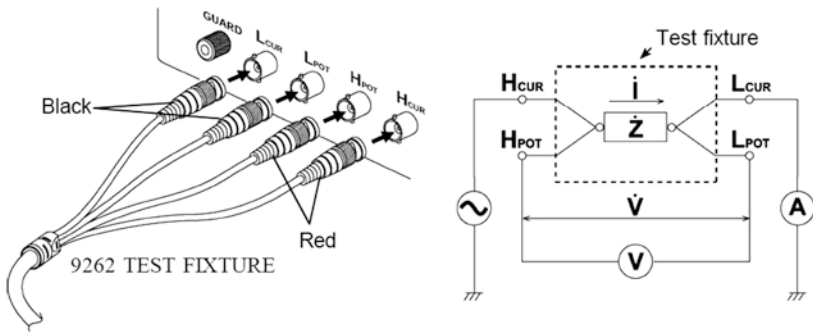


Fig. 2.12 Connecting LCR3522-50/3532-50 to the 9262 test fixture and developed interdigital sensing system

equipment. The outer set of terminals, named H_{CUR} and L_{CUR} on the front panel, are used to measure the current flowing through the sensor, whereas, the inner set of terminals, appointed as H_{POT} and L_{POT} , measure the potential across the sensor at any instant of time. Detail description is shown in Fig. 2.12. Table 2.2 displays the details of fixture connection with shielding to the device under test (DUT).

2.3.3 RS-232C Interface for 3522-50/3532-50 LCR Hi Tester

An RS-232C was used to interface Hioki LCR3522-50 to a desktop/laptop computer in order to develop an automatic data acquisition system. Use of the interface made it possible to control all the functions of the LCR3522-50/3532-50 using software algorithm. The graphical user interface was developed in Labview software to input setting parameters except power on/off. The program consisted of commands and queries made by the data acquisition computer system to the interfaced instrument. A command sent is a set of instructions or data to setup the test conditions

Table 2.2 Hioki Hi Precision LCR test terminals description

Test Terminal	Description
H _{CUR}	Carries the signal current source. Connected to the excitation electrodes of the interdigital sensor
H _{POT}	Detected high voltage sense terminal. Measure potential difference at any instant of time
L _{POT}	Detected low voltage sense terminal
L _{CUR}	Test Current detection terminal
GUARD	Connected to the GND input to minimize noise

Table 2.3 LCR testing parameters and calculation equations

Parameter	Series equivalent circuit mode	Parallel equivalent circuit mode
Z	$ Z = V/I (= \sqrt{R^2 + X^2})$	
Y	$ Y = 1/ Z (= \sqrt{G^2 + B^2})$	
R	$R_s = ESR = Z \cos\theta $	$R_p = 1/ Y \cos\theta (= 1/G)$
X	$X = Z \sin\theta $	
G		$G = Y \cos\theta $
B		$B = Y \sin\theta $
L	$L_s = X/\omega$	$L_p = 1/\omega B$
C	$C_s = 1/\omega X$	$C_p = B/\omega$
D	$D = 1/\tan \theta $	
Q	$Q = \tan \theta = (1/D)$	

communicated to the LCR meter, whereas query is a set of data or status information requested from the LCR meter. The LCR transmitted the measured/calculated parameters in response to the queries made by the data acquisition computer. The software echoed back the received automatic measurements of the required parameters’ data on the computer monitor via a graphical user interface in addition to writing/saving it in Microsoft Excel worksheet in ‘xls’ format. Table 2.3 provides the details of the parameters measured and calculated by LCR3522-50/3532-50 using the mathematical equations mentioned against each parameter. The data acquisition computer system was used to analyse further the saved information to study the impedance characteristics of the developed sensors and material under test.

2.3.4 Conclusions

The experimental setup, instrumentation, program and measurement methods have been discussed in this chapter. High precision LCR meter’s interface with the LABVIEW program has been established in order to erect a stand-alone automatic measurement system. Details of the experimental setup, connection cables,

instruments settings, and program interface were explained in the chapter. The basic theory of measurement method using Impedance Spectroscopy (IS) has also been discussed to enlighten the reader with the basic measurement methodology. The setup has been built to a stage where it could be interfaced with a smart sensing transducer that could fetch the information from the electrochemical cell, interpret it into required electrical signal so that valuable information about the kinetic processes taking place inside the cell could be extracted. Development of a sensitive, selective and reliable sensor was the most important part of this research project. The details of the development of the smart sensor are discussed in the following chapter.

References

1. E.J. Olson, P. Buhlmann, Minimizing hazardous waste in the undergraduate analytical laboratory: a microcell for electrochemistry. *J. Chem. Educ.* **87**(11), 1260–1261 (2010)
2. M. Khafaji, S. Shahrokhian, M. Ghalkhani, Electrochemistry of levo-thyroxin on edge-plane pyrolytic graphite electrode: application to sensitive analytical determinations. *Electroanalysis* **23**(8), 1875–1880 (2011)
3. J. Fischer, H. Dejmokova, J. Barek, Electrochemistry of pesticides and its analytical applications. *Curr. Org. Chem.* **15**(17), 2923–2935 (2011)
4. C. Valero Vidal, A. Igual Muñoz, Effect of physico-chemical properties of simulated body fluids on the electrochemical behaviour of CoCrMo alloy”. *Electrochim. Acta* **56**(24), 8239–8248 (2011)
5. C. Wolner, G.E. Nauer, J. Trummer et al., Possible reasons for the unexpected bad biocompatibility of metal-on-metal hip implants. *Mater. Sci. Eng., C* **26**(1), 34–40 (2006)
6. C. Xhoffer, K. Van den Bergh, H. Dillen, Electrochemistry: a powerful analytical tool in steel research. *Electrochim. Acta* **49**(17), 2825–2831 (2004)
7. J.R. Macdonald, Impedance spectroscopy. *Ann. Biomed. Eng.* **20**(3), 289–305 (1992)
8. S.C. Mukhopadhyay, C.P. Gooneratne, G.S. Gupta et al., A low-cost sensing system for quality monitoring of dairy products. *Instrum. Measur. IEEE Transac.* **55**(4), 1331–1338 (2006)
9. S.C. Mukhopadhyay, C.P. Gooneratne, A novel planar-type biosensor for noninvasive meat inspection. *Sens. J. IEEE* **7**(9), 1340–1346 (2007)
10. S. Mukhopadhyay, S.D. Choudhury, T. Allsop et al., Assessment of pelt quality in leather making using a novel non-invasive sensing approach. *J. Biochem. Biophys. Methods* **70**(6), 809–815 (2008)
11. S.C. Mukhopadhyay, G.S. Gupta, J.D. Woolley et al., Saxophone reed inspection employing planar electromagnetic sensors. *Instrum. Meas. IEEE Transac.* **56**(6), 2492–2503 (2007)
12. M. Rahman, S.B. Abdul, S.C. Mukhopadhyay et al., Novel sensors for food inspections, *Sens. Trans. (1726–5479)* **114**(3) 2010
13. A. Mohd Syaifudin, S. Mukhopadhyay, P. Yu et al., Characterizations and performance evaluations of thin film interdigital sensors for Gram-negative bacteria detection. pp. 181–186
14. A. Mohd Syaifudin, S. Mukhopadhyay, P. Yu et al., Detection of natural bio-toxins using an improved design interdigital sensors. pp. 1028–1031
15. A. Mohd Syaifudin, S. Mukhopadhyay, P. Yu, Modelling and fabrication of optimum structure of novel interdigital sensors for food inspection, *Int. J. Numer. Model. Electron. Netw. Devices Fields* **25**(1), pp. 64–81 (2012)
16. M.S. Abdul Rahman, S.C. Mukhopadhyay, P.-L. Yu et al., Detection of bacterial endotoxin in food: new planar interdigital sensors based approach, *J. Food Eng.* **114**(3), pp. 346–360 (2013)

17. A.I. Zia, A.R. Mohd Syaifudin, S.C. Mukhopadhyay et al., MEMS based impedimetric sensing of phthalates. pp. 855–860
18. E. Barsoukov, J.R. Macdonald, Impedance spectroscopy: theory, experiment, and applications: Wiley-Interscience (2005)
19. B.-Y. Chang, S.-M. Park, Electrochemical impedance spectroscopy. *Ann. Rev. Anal. Chem.* **3**, 207–229 (2010)
20. J.E.B. Randles, Kinetics of rapid electrode reactions. *Discuss. Faraday Soc.* **1**, 11–19 (1947)

Chapter 3

Novel Interdigital Sensors' Development

3.1 Introduction to Interdigital Sensors

Affinity sensors are the most frequently used devices for biological and chemical sensing research and applications. These can be segregated into two broad categories depending on the target binding techniques applied; labelled and label-free. Labelled sensors use immunoassay approach for binding the target molecule that is purely laboratory-based technique involving expensive, time-consuming and hi-tech laboratory protocols, hence, rendering real-time measurements impossible. Sensors for direct, label-free quantification of analytes are attractive to researchers for a number of reasons like direct detection of analytes with minimal or no sample preparation, cost effective, simple and real-time. These involve optical, mass-sensitive and electrochemical detection routes for measurement of an analyte in the bulk sample. Optical sensors are the most studied, but the electrochemical sensors are relatively more sensitive and display comparatively lower detection limit capabilities with a requirement of least complicated support instrumentation. On the other hand, optical and mass-sensitive techniques claim state-of-the-art electronics and bulky instrumentation for interpretation of optical and mass variation data into clear information.

The term 'interdigital' (ID) refers to digit-like or finger-like parallel in-plane electrodes built in a periodic pattern in order to exploit the capacitive effect produced as a result of applied alternating electric field that fringes through the material sample and carries useful information about it. This term is often replaced by 'interdigitated', 'combed' and 'microstrip' in the research literature but, strictly speaking, it is the name of a specialized geometric structure shown in Fig. 3.1, which owns significant advantages in accessing the material properties. The most significant benefit is a single side access to the material under test (MUT). This benefit provides freedom of penetrating the sample with the electric, magnetic or acoustic field only on the single side which encourages in situ measurements and detections. Other advantages of interdigital structures include its capability to be used for non-destructive testing which makes it more useful for process control and inline testing applications [1]. The penetration depth of quasi-static electric field

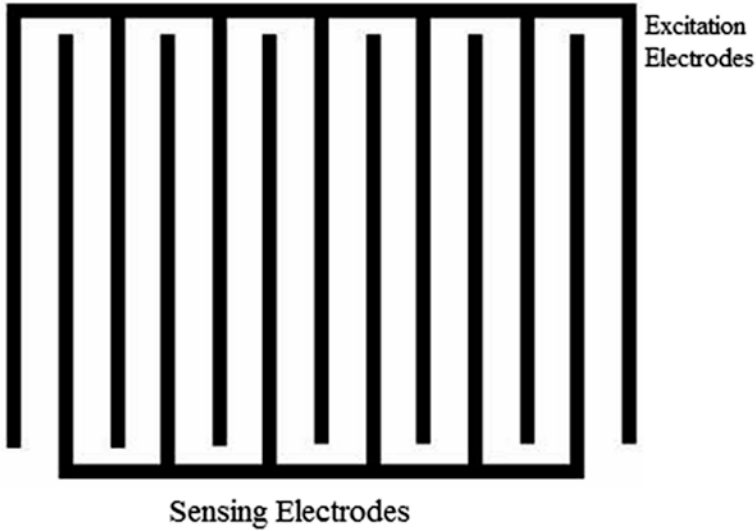


Fig. 3.1 Planar interdigital sensor geometry

lines can be varied thus making it possible to obtain dielectric profiling and conduction properties of semi-insulating materials. These dielectric properties profiling can be further helpful in evaluating other physical parameters of the material under test like density, structural integrity and chemical content in that material sample [2].

The technology of planar interdigital sensors is under development since last three decades. These sensors are employed in a number of applications like photosensitive detection, humidity detection, chemicals and gas sensing, moisture sensing applications and measurement of electrolytic conductivity [3]. The dielectric characterization to evaluate the material properties is one of the most interesting areas where interdigital sensors along with meander coils are successfully employed to study the dielectric properties of meat [4], leather [5], dairy products [6] and saxophone reeds [7].

Conventional interdigital sensors operate on the principle of a parallel plate capacitor. Parallel plate capacitors offer uniformity of the applied electric field and the equations related to the dielectric material properties are simple, but these 3D structures do not provide single side and non-invasive testing freedom. Interdigital sensors, on the other hand, are 2D structures (coplanar geometry) and provide non-destructive, in situ and single side access to the material under test. The transformation of parallel plate capacitor to interdigital one is shown in Fig. 3.2.

The transformation occurred at the cost of the electric field which changed from uniform electric field to 'fringing electric field' penetrating through the material under test. That is the reason conventional interdigital sensors are also referred as fringing field dielectrometry sensors in the literature. The basic idea behind this transformation is to apply spatially periodic electric field to the material under test using single side access to the material. The penetrating field lines combined with

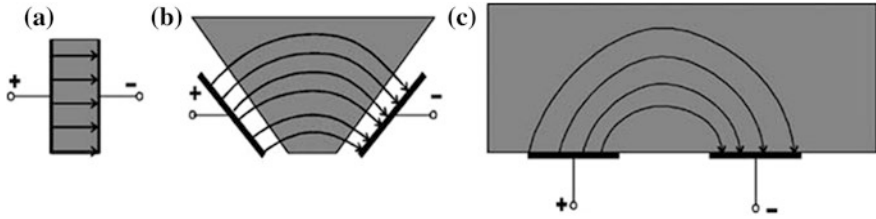


Fig. 3.2 Concept of transformation, **a** parallel plate capacitor, **b** transformation to planar geometry, **c** coplanar structure

the variation of applied excitation frequency carry useful dielectric spectroscopic information about the material sample [8]. A change in the dielectric material properties is a function of various chemical, physical and structural properties of the material. Therefore, a comparative study of electrochemical impedance spectroscopy of material sample reflects the changes in material properties. The well-known expression for capacitance is given by:

$$C = \frac{\epsilon_0 \epsilon_r A}{d} \quad (3.1)$$

where C is the capacitance, ϵ_0 is the permittivity of free space (8.8554×10^{-12} F/m), ϵ_r is the relative permittivity of the dielectric medium used, A is the area, and d is the spacing between the positive and negative electrode. The value of capacitance varies directly with the area A of electrodes, according to Eq. (3.1), and for interdigital sensors the area of electrode is sacrificed considerably due to its coplanar structure. The value of the capacitance in ID structure is reduced to an extent that it approaches the stray capacitance of the conductors connecting excitation source and electrodes. This limitation necessitates the use of repeated coplanar structures connected in parallel to keep the signal to noise ratio at an acceptable range. Important concepts related to this technology are discussed in detail in [9–11].

3.2 Novel Planar Interdigital Sensors

Depending on the application, the penetration depth of the fringing electric field is considered one of the most important parameter in the design of the ID sensor structures. The penetration depth of the fringing quasi-static electric fields above the interdigital electrodes is proportional to the spacing between the centre lines of the sensing and the driven fingers and is independent of frequency. This spacing is termed as spatial wavelength ' λ '. The effect of variation in the spatial wavelength is illustrated in Fig. 3.3.

In order to increase the penetration depth, novel ID sensors were designed with a greater number of sensing electrodes as compared to the driving or excitation electrodes. Different geometries have been discussed in research literature [12]. A.R.M

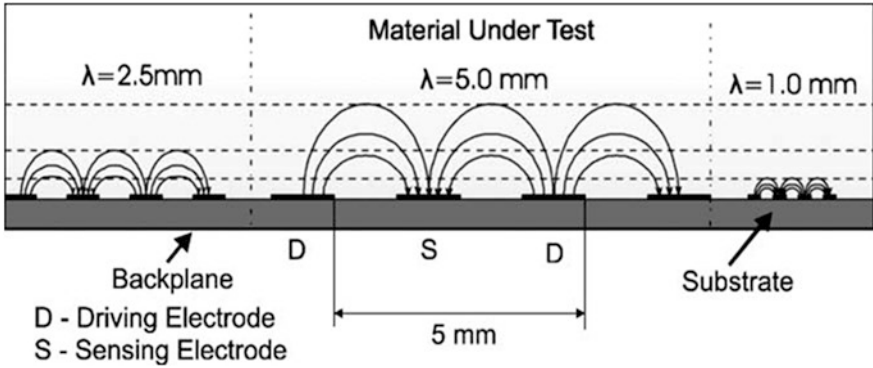
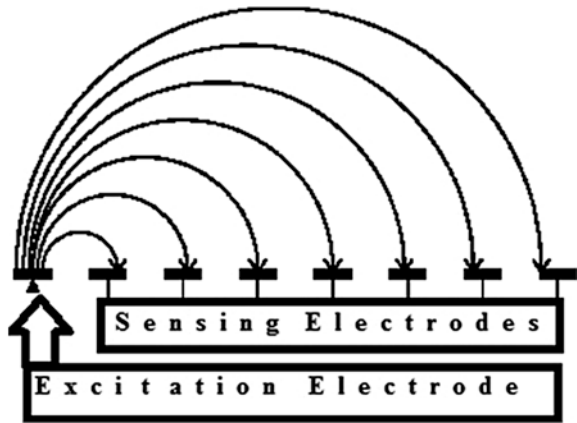


Fig. 3.3 The penetration depth of electric field lines is proportional to the electrode spatial period λ .

Fig. 3.4 Excitation pattern for multi-sensing electrode ID sensor geometry



Syaifudin et al. investigated the capacitance and penetration depth as a function of a number of negative (sensing) electrodes keeping the sensing area of the ID geometry constant, and varying the substrate material. The concept of variation in penetration depth with a higher number of sensing electrodes is illustrated in Fig. 3.4.

3.3 Finite Element Modelling Using COMSOL Multiphysics®

COMSOL Multiphysics is finite element analysis software designed to facilitate physicists and engineers to simulate the actual environment and boundary conditions of the experiment to analyse the outcome of the proposed experiment mathematically. The FEM makes use of the solution of partial differential equations and Maxwell's equations to simulate the design and geometry of the sensor.

In this research, four different geometries of novel ID sensors were simulated using COMSOL. Sensing area, substrate thickness, substrate material and electrode dimensions were kept constant with a variation in the number of sensing electrodes, pitch length and spatial wavelength. To avoid confusion, it is worth mentioning that pitch length is the distance between two adjacent electrodes, whereas, the spatial wavelength is the separation between two electrodes of the same polarity (excitation electrodes in this case). To obtain a trade-off between capacitance value, pitch length and spatial wavelength for different geometries of the ID sensor were modelled using COMSOL Multiphysics version 4.2 [13].

The sensors were modelled in the three-dimensional workspace with micro-metre sized electrodes and pitch length. Four sensors with different geometries and a different number of sensing electrodes were modelled keeping the effective sensing area, substrate material, electrode thickness and electrode area constant. Sensing area of each electrode sensor was fixed to $2.5 \text{ mm} \times 2.5 \text{ mm}$, electrode thickness to 520 nm and electrode area was kept constant at $25 \text{ }\mu\text{m} \times 245 \text{ }\mu\text{m}$. Each sensor contains a different number of capacitive ID features in parallel which enables it to achieve strong sensing signal and acceptable level of the signal to noise ratio. The constant geometric parameters facilitated us in simplifying the design and were in compliance to the available feature size that could be fabricated at the MEMS fabrication facility. Pitch length and number of sensing electrodes were varied in order to get a design suitable for the particular application [14].

Single crystal silicon substrate with thickness $525 \text{ }\mu\text{m}$ and relative permittivity (ϵ_r) 4.2 was used in the models so that the proposed models may practically be fabricated on commercially available 4 in. silicon wafer. In order to calculate capacitance, stored electric energy, penetration depth of electric field lines and field intensity the model was exposed to a dielectric medium on the top with a dielectric constant of 80 and 5.1. These are the dielectric constant values corresponding to pure MilliQ water and DEHP which were selected to observe the model response of each sensor towards the material under test. To obtain higher penetration depth and uniform electric field distribution throughout, the sensor geometry was designed with two configurations of five and eleven sensing electrodes. Figure 3.5 shows the geometric features of two ID sensors 1-5-25, 1-11-25 with pitch length of $25 \text{ }\mu\text{m}$. Figure 3.6 shows the geometry built in COMSOL for 1-5-50 and 1-11-50, bearing pitch length of $50 \text{ }\mu\text{m}$ in both cases. It should be noted that the sensor type number specifies the number of sensing electrodes and pitch length in micrometres. For example 1-5-50 illustrates: 1 excitation electrode, 5 sensing electrodes and $50 \text{ }\mu\text{m}$ pitch length.

The objective of modelling four different types of sensors was to obtain the best-suited design for the proposed application. The models were built on a substrate, and a pseudo test medium with known dielectric constant was used on the sensing side in order to figure out the sensor with best possible sensitivity for the material under test. COMSOL uses finite element meshing to evaluate the potential distribution and electric field intensity not only in the material under test but in the substrate, as well, to calculate the value of capacitance and stored electrical energy for the whole structure. Figure 3.7 provides a three-dimensional illustration

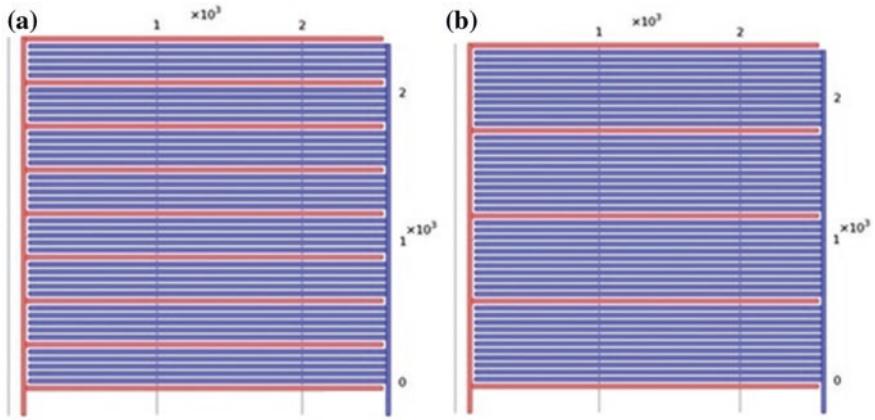


Fig. 3.5 COMSOL geometric models of ID sensors with 25 μm pitch length, **a** 1 excitation, 5 sensing electrodes, **b** 1 excitation, 11 sensing electrodes

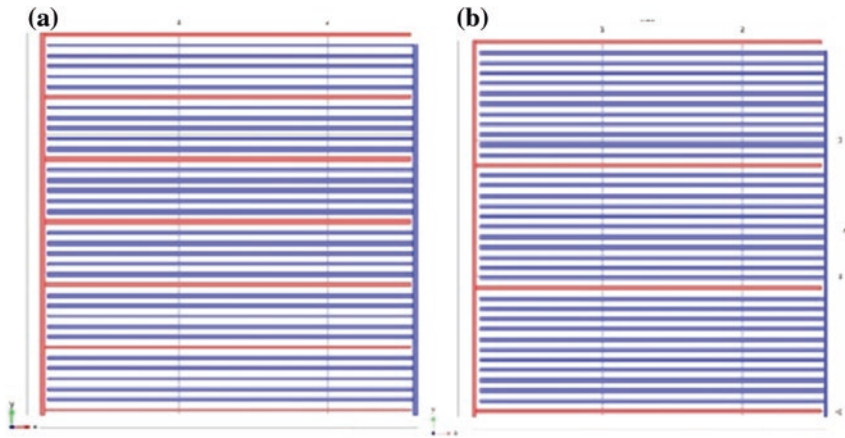


Fig. 3.6 COMSOL geometric models of ID sensors with 50 μm pitch length, **a** 1 excitation, 5 sensing electrodes, **b** 1 excitation, 11 sensing electrodes

of the ID sensor structure displaying simulated substrate and material under test. For viewing of the ID electrode structure, the material under test is rendered transparent in the figure.

The electrostatic study of sensors model was carried out using the AC/DC module of COMSOL. The evaluation of electrostatic energy density ‘ W_e ’ is obtained using the COMSOL simulation. The amount of energy required to charge a capacitor equals energy of applied electrostatic field, given by;

$$W_e = \frac{Q^2}{2C} \tag{3.2}$$

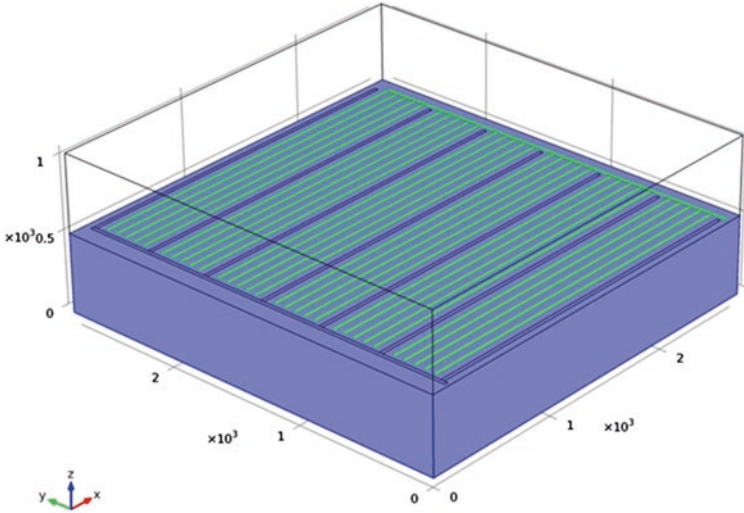


Fig. 3.7 1-5-50 Sensor structure; Silicon substrate (*bottom*) material sample (*top*)

The auto calculation of W_e is available in the Electrostatics application of COMSOL; FEM calculates it by integrating the scalar product of electric displacement D and electric field intensity E across the electrostatic domain, $d\Omega$ is the domain boundary. Equation (3.3) shows the expression integrated over the electrostatic domain to calculate energy.

$$W_e = \int_{\Omega} (D \cdot E) d\Omega \tag{3.3}$$

The capacitance, C , is related to the total charge accumulated on the two conductive plates, Q , and the voltage difference between them, ΔV , by;

$$C = \frac{Q}{\Delta V} \tag{3.4}$$

The calculation of C is carried out by the stored electric energy, W_e .

The voltage across the two plates, ΔV , and is given by;

$$C = \frac{Q^2}{2W_e} = \frac{C^2 \Delta V^2}{2W_e} \Rightarrow C = \frac{2W_e}{\Delta V^2} \tag{3.5}$$

where W_e is the stored electrostatic energy density and V_0 is the applied voltage to the excitation electrode. The sensing electrode is kept at 0 V.

The analyses conducted using COMSOL were used to evaluate the electric field distribution and electric field intensity for all four sensors. COMSOL simulated electric potential distribution in the sensors is shown in Figs. 3.8 and 3.9. For the

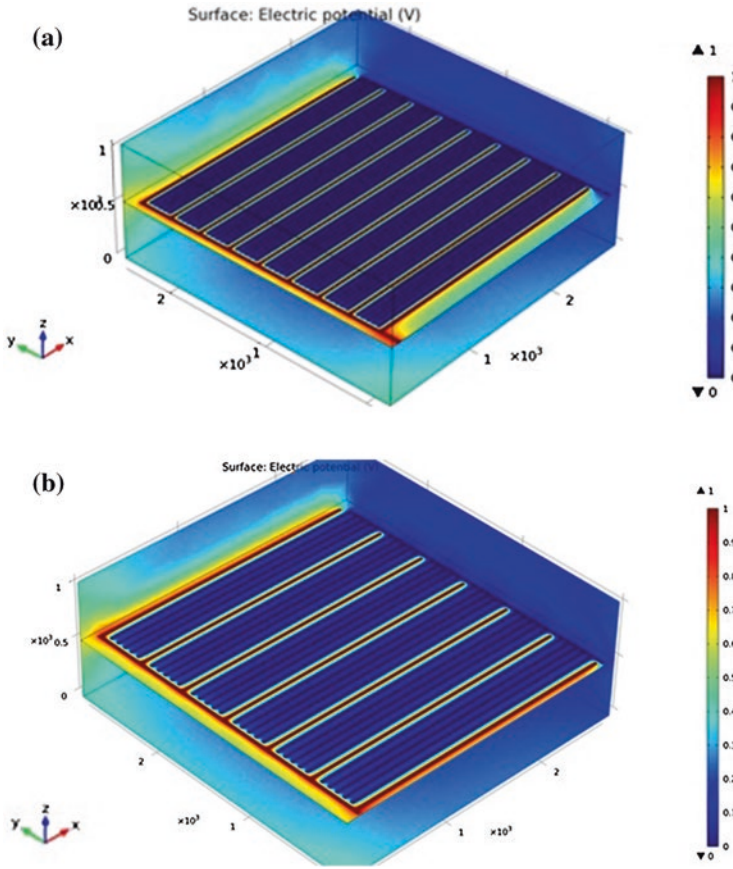


Fig. 3.8 Potential distribution modelling in COMSOL for **a** 1-5-25, **b** 1-5-50

sake of simplification of the problem, the voltage applied to the excitation electrodes of sensor models, V_0 in the simulation is kept at 1 V but the actual experiments were carried out at 100 mV–1 V in order to avoid capacitive effects and stray inductance of the connecting wires.

Further analysis was conducted to evaluate the distribution of electric field and intensity for all the four types of sensors. The model calculated the capacitance value and total electrical energy stored for both sensors for the anticipated material used for practical testing. For this purpose, analyses were carried out for material with dielectric constant 80 (MilliQ) first and then for material with dielectric constant 5.1 (DEHP) keeping the dielectric constant of the substrate 4.2 (single crystal silicon) constant throughout the analyses.

The calculated values for capacitance and total electrical energy stored in are presented in Table 3.1 which provides necessary information to choose the right sensor for fabrication.

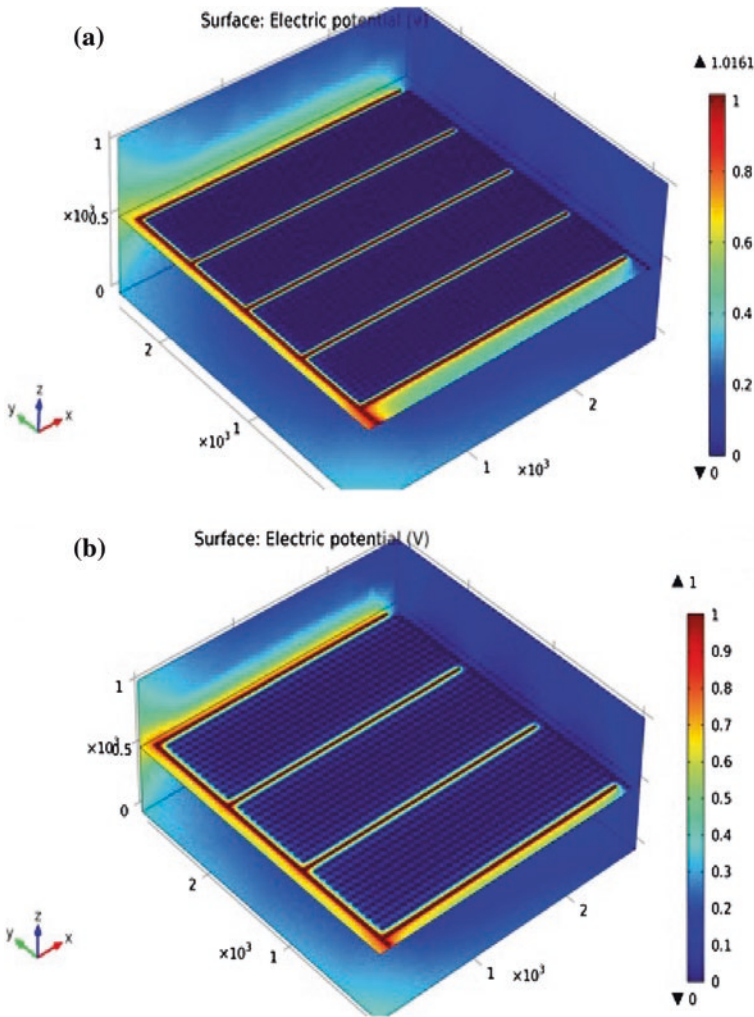


Fig. 3.9 Potential distribution modelling in COMSOL for a 1-11-25 and b 1-11-50 ID sensors

The plot in Fig. 3.10 shows the capacitance value calculated for all four ID sensors using COMSOL Multiphysics for proposed dielectric medium to be tested i.e. MilliQ and DEHP. The plot shows that sensor 1-5-25 displays least response towards DEHP as it shows nearly same values for both kinds of dielectric mediums.

It should be noted that each sensor has a different number of parallel ID capacitor features as shown in Table 3.2. The plot for the capacitance of single ID capacitor feature is presented in Fig. 3.11.

The plot in Fig. 3.11 explicitly depicts that 1-11-25 displays most responsive behavior for a medium such as DEHP whereas 1-11-50 should perform

Table 3.1 Calculated values of capacitance and total electrical energy stored for all four sensors using COMSOL Multiphysics®

Sensor type	Milli-Q $\epsilon_r = 80$		DEHP $\epsilon_r = 5.1$	
	Capacitance (F)	Energy (J)	Capacitance (F)	Energy (J)
1-5-25	2.1564e-12	1.0782e-12	2.3915e-12	1.1958e-12
1-5-50	1.3942e-11	6.9712e-12	1.5243e-12	7.6213e-13
1-11-25	1.2619e-11	6.3097e-12	1.376e-12	6.8799e-13
1-11-50	8.4627e-12	4.2314e-12	9.2558e-13	4.6279e-13

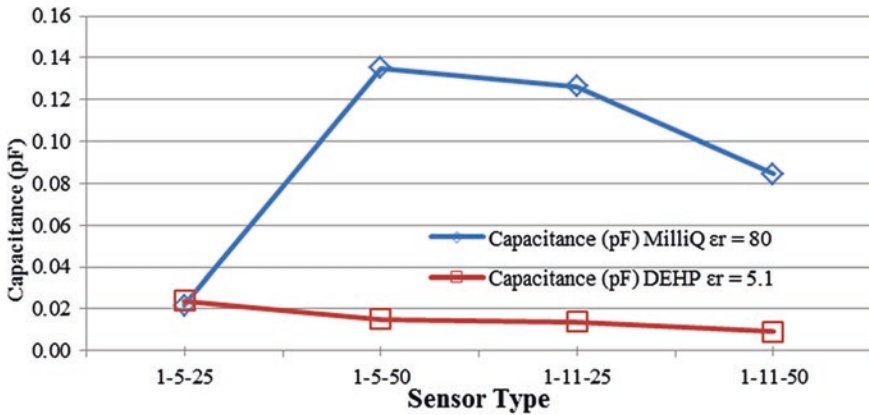


Fig. 3.10 Modelled capacitance for ID sensors

Table 3.2 Geometric design parameters for all four types of modelled ID sensors

Sensor type	Pitch length (μm)	Number of sensing elect	Number of excite elec	Sensing area (mm^2)	Capacitors in ID sensor
1-5-25	25	40	9	6.25	8
1-5-50	50	30	7	6.25	7
1-11-25	25	44	5	6.25	5
1-11-50	50	33	4	6.25	3

comparably well in the detection of DEHP in water. 1-5-50 has an intermediate response whereas 1-5-25 is completely irresponsive to the change of dielectric properties of the material under test. The electric field intensity and penetration depth of electric flux lines simulated in the modeled sensors using COMSOL Multiphysics are shown in Fig. 3.12. Electric field intensity is a measurement of the electric field (V/m) along the z-axis.

The electric fields simulated on the potential distribution plots provide a clear visualization of the idea of the fringing electric field penetrating through the material under test as described earlier in the literature survey on the topic. It is also

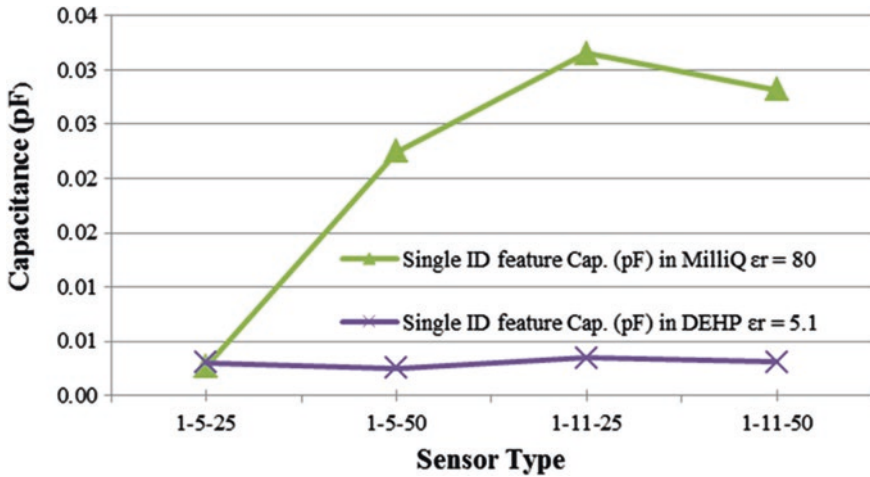


Fig. 3.11 Modelled capacitance of single ID capacitor feature on each sensor

worth noting that the electric field penetrates into the substrate material, as well, which contributes toward the numerical calculations of the capacitance and the stored electric energy in the device. For a good comparison of the performance of all four sensors, therefore, the parameter of the substrate dielectric constant is not varied throughout the sensor design. Minimum electric field intensity is observed for 1-5-25, whereas a maximum value for 1-11-50 is clearly displayed in Fig. 3.12. The average penetration depth for 1-5-25 is calculated to be 137.5 μm , for 1-5-50 is 212.5 μm , for 1-11-25 is 287.5 μm and for 1-11-50, it has a maximum value of 437.5 μm which is evident in the images from the COMSOL models are given in Figs. 3.12 and 3.13. The thickness of the test medium was, therefore, kept constant at 525 μm throughout the simulation.

3.4 Sensors' Fabrication

The fabrication of the sensors was realized at King Abdullah University of Science and Technology, Saudi Arabia as a result of academic collaboration between the former and School of Engineering and Advanced Technology, New Zealand [15]. The sensors were fabricated with two pitch lengths, 25 and 50 μm , respectively. Each type of sensor was fabricated for two repeated patterns of 1 excitation, 5 sensing electrodes and 1 excitation and 11 sensing electrodes coded as 1-5 and 1-11, respectively. This variation was carried out due to the fact that the optimum number of sensing electrodes between excitation electrodes contributes towards the sensitivity of the device. Therefore, four electrode geometries were fabricated for practical performance analysis stated in this research thesis. The wafers fabricated with the said sensor geometries were further coated with polymer layers. All

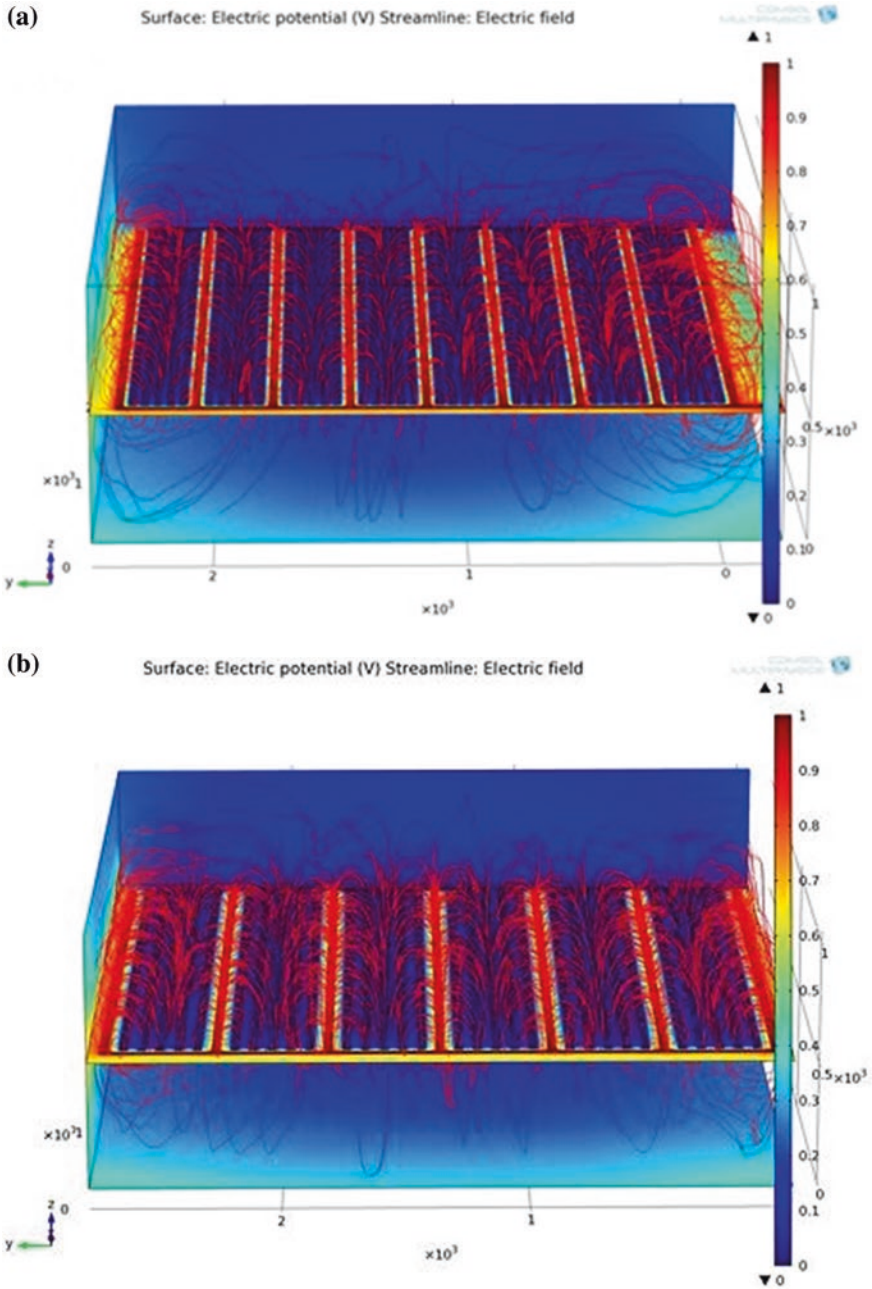


Fig. 3.12 Electric field and penetration depth simulation using COMSOL a 1-5-25, b 1-5-50

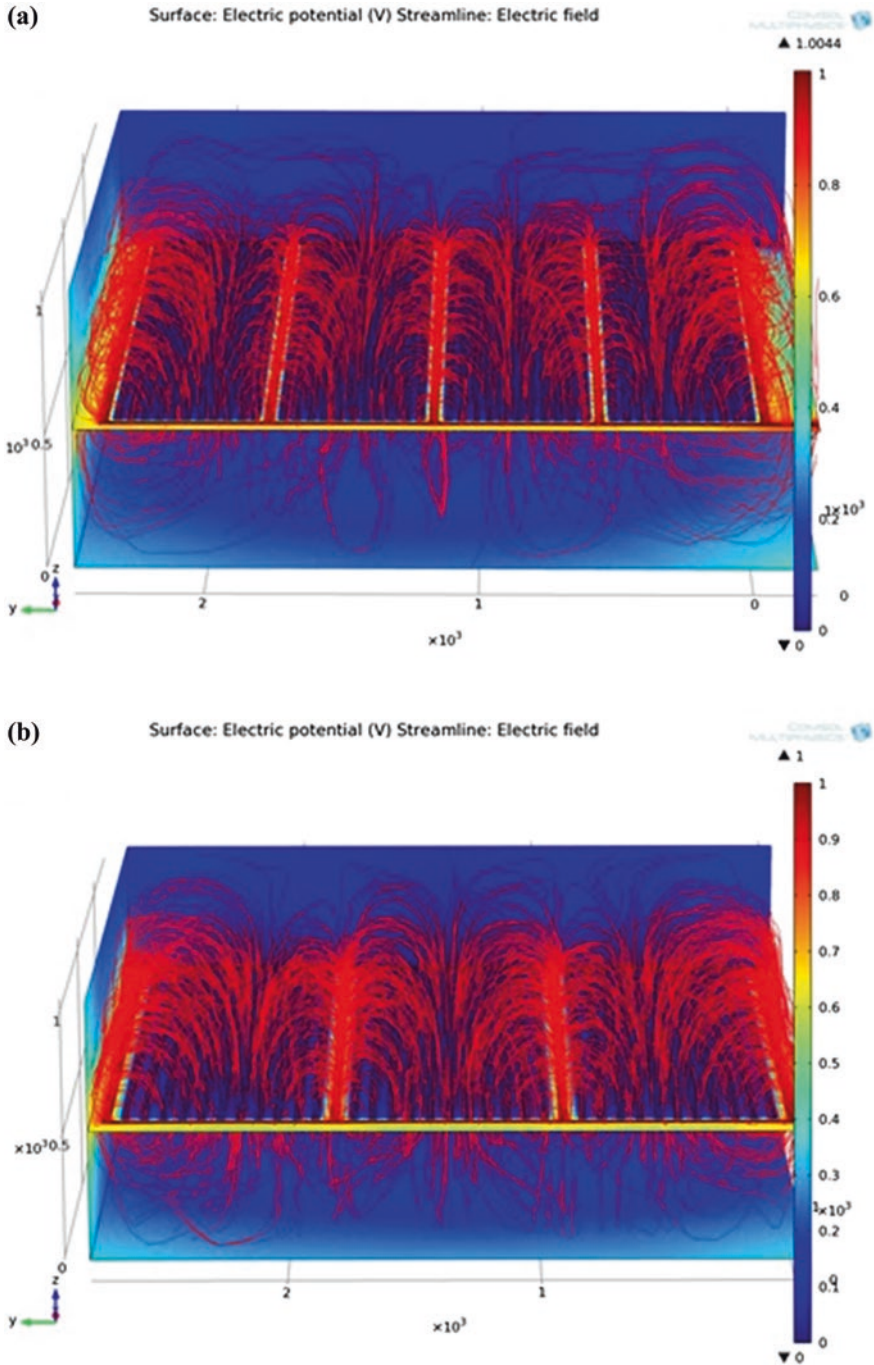


Fig. 3.13 Electric field and penetration depth simulation using COMSOL a 1-11-25 and b 1-11-50 ID sensors

areas except the electrodes and bonding pads were covered with a coating. Since the sensing area is kept open, a molecular-selective coating can be applied directly to the electrodes and the sensing area. This approach helped target analytes to be attracted and absorb as close as possible to the sensing (electrode) surface leading to high detection signals. Two different materials namely; perylene C and Silicon Nitride (Si_3N_4), were used for coating purpose on various wafers of fabricated sensors. Perylene C is a polymeric material that provides pinhole-free isolation for the sensor from the corrosive test samples but is relatively softer material as compared to Si_3N_4 . Therefore, a coating thickness of $1\ \mu\text{m}$ was used for perylene C, whereas, Si_3N_4 was coated to $200\ \text{nm}$ only.

Planar interdigital (PID) thin film electrode structures were fabricated by DC magnetron sputtering process on a single crystal, p-doped, 4-in. diameter, $525\ \mu\text{m}$ thick and single-side polished silicon wafer. Commercially available photolithography and etching techniques were used for the fabrication process. This type of sensors owns an advantage of noncontact measurements due to fabrication on a rigid substrate which maintains the well-defined geometry of the electrode structure essentially required to implement model-based parameter estimation algorithms effectively. 'Coventorware[®]' software was used to design the patterns of the ID structures. 36 workable sensors each with dimensions of $10\ \text{mm} \times 10\ \text{mm}$ and sensing area of $6.25\ \text{mm}^2$ were patterned on a wafer over native grown SiO_2 layer. The width of electrodes was set to a constant value of $25\ \mu\text{m}$ with sensing area dimensions as $2.5\ \text{mm} \times 2.5\ \text{mm}$ respectively as shown in Fig. 3.14. The four ID structure geometries are illustrated in Fig. 3.15.

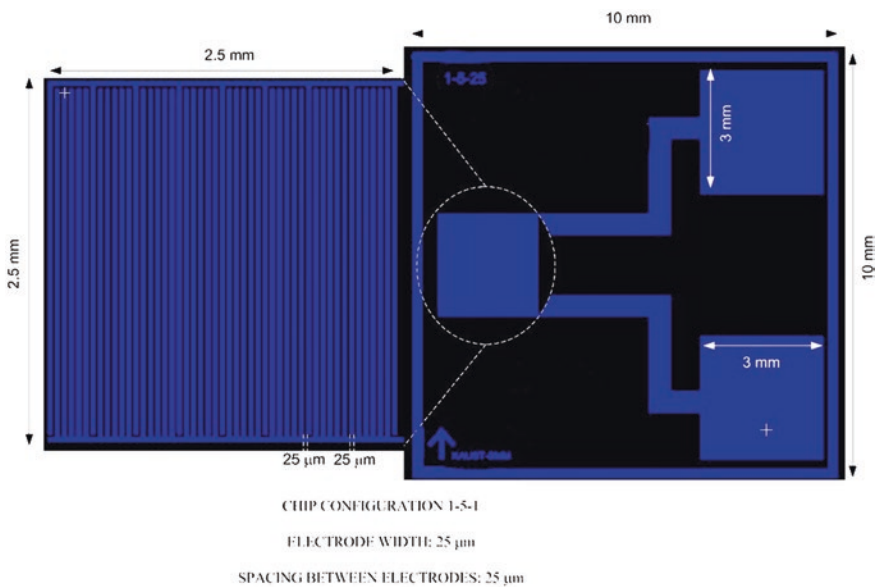


Fig. 3.14 1-5-25 sensor: basic design geometry and dimensions

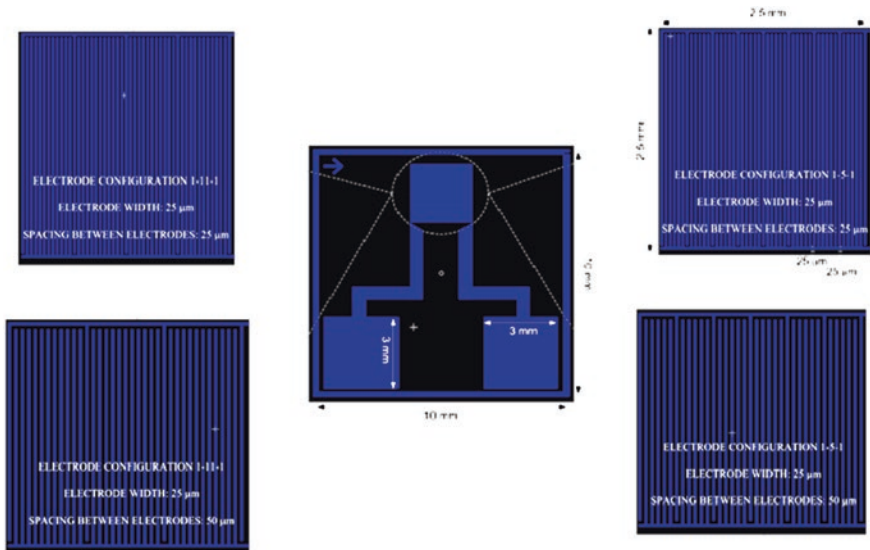


Fig. 3.15 Interdigital electrode fabrication configurations

All patterns were printed on a 5-in. soda lime transparent mask using a laser mask writer. Pre-baking was performed at 150 °C on the wafer substrate, so photoresist attached better to the surface. A spin coater was used to coat 4 μm of positive photoresist (EC13027) on a 4-in. wafer.

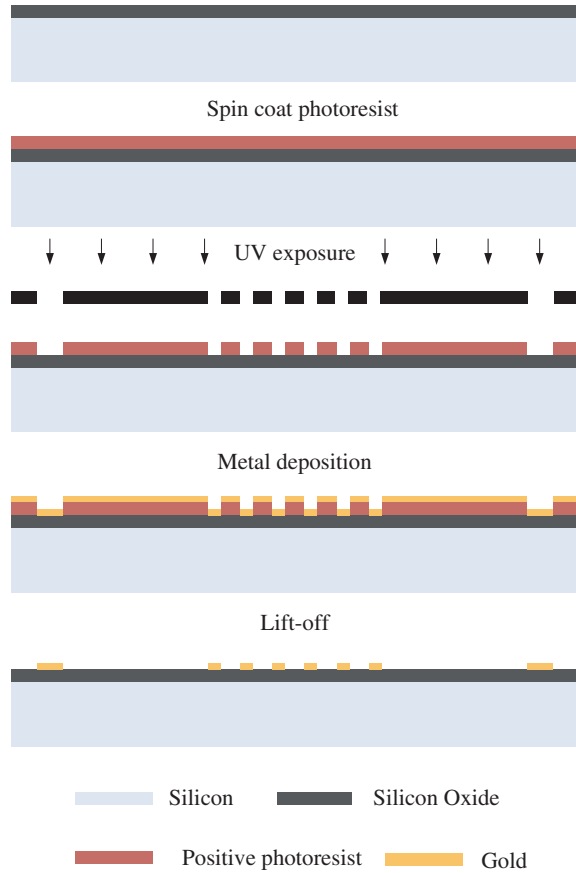
An oven was used to post bake the wafer at 100 °C for 1 min. A UV light exposure tool was used to transfer the ID patterns to photoresist of the wafer. A constant dose of 200 mJ/cm³ was used for a separation of 30 μm between the wafer and the mask. The wafer was then developed for one minute under a solution Tetra-Methyl Ammonium Hydroxide (TMAH) based solution (AZ 726).

Plasma etching at 70 °C was used to perform a “Descum” process to remove residual photoresist in the trenches. Following this, 20 nm of Chromium (Cr) and 500 nm of Gold (Au) were sputtered onto the wafer substrate by DC magnetron sputtering. Gold electrodes have the advantage of being inert and flexible.

Argon gas was used at a pressure of 30 mTorr and the DC power was set to 800 W. Lift-off was then performed with a solution of acetone. Figure 3.16 shows the steps involved in the fabrication process of the sensors.

After lift-off, the wafer was coated with a 1 μm layer of Parylene C. Figure 3.17 shows the coating procedure with Parylene C. The passivation layer is required to protect the sensing area from corrosion by the solutions used during experimentation. Furthermore, it prevents moisture diffusion into the Si/SiO₂ substrate that could influence its dielectric properties which would affect sensor response. The electrodes and conducting connecting lines were covered except parts of the bonding pads. Parylene C is an ideal passivation layer; since it has a

Fig. 3.16 Fabrication process for all four types of sensors



favorable combination of electrical and physical properties as well as a very low permeability to moisture and other corrosive substances. Furthermore, Parylene can withstand continuous exposure to air at temperatures of up to 100 °C for 10 years while under vacuum, or inert atmospheric conditions the temperature limit increases to 220 °C.

A conformal parylene coater was used to coat the wafer with parylene. The deposition of parylene C is void and pinhole free, and it does not edge, bridge or gap and the wafer in the chamber gets uniformly coated since the vapour deposition process is not in the line of sight. After the parylene coating, 4 μm of positive photoresist (EC13027) was coated on the wafer. A UV light exposure tool was used to soften the resist over the bonding pad windows. After development plasma etching was used to etch the parylene and open via to the bonding pads at RF power 800 W, temperature (chamber and substrate) 100 °C, pressure 500 mTorr and O₂ 100 sccm. Figure 3.18 shows 4 in. Silicon substrate fabricated with all four types of sensors and individual sensor against scale for dimension observation.

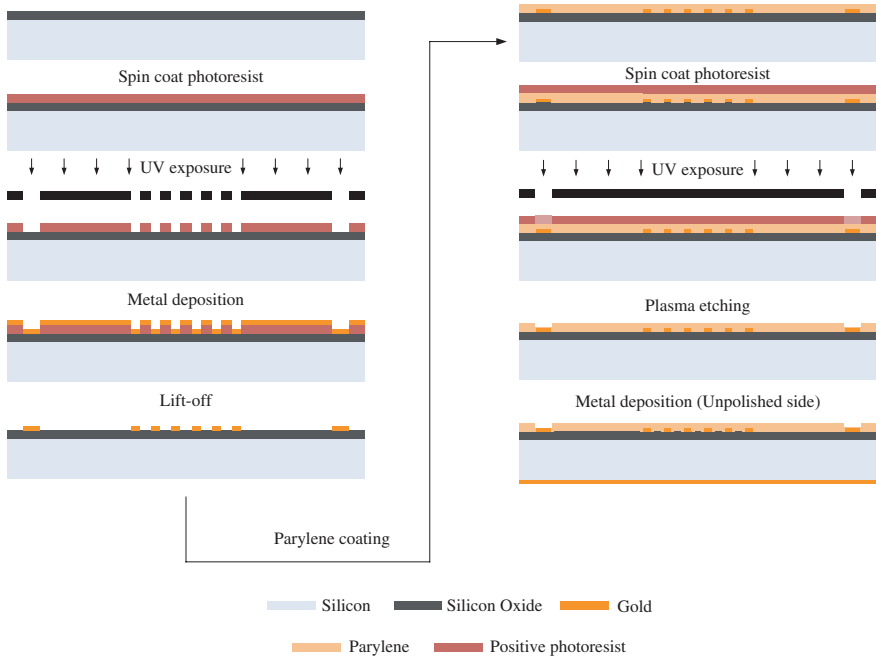


Fig. 3.17 Steps involved in coating 1 μm passivation layer of Parylene C

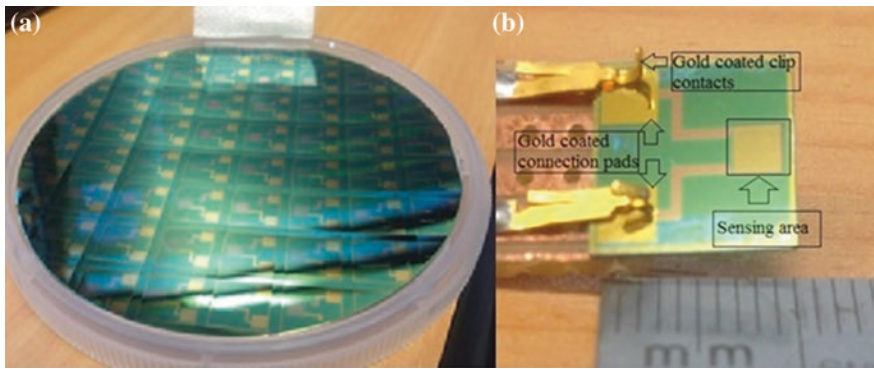


Fig. 3.18 a 36 Workable sensors fabricated on one wafer. b Individual sensor shown against scale

An improved design of the silicon sensors were coated with a different but relatively harder material, Silicon Nitride. After fabrication steps, as in Fig. 3.16, the wafer was coated with a 200 nm layer of (Si_3N_4) by Plasma Enhanced Chemical Vapour Deposition (PECVD). Si_3N_4 has been used in many micro-devices as a passivation layer. The silicon nitride film thickness can be easily controlled and

modified by varying its deposition methods. Above all, Si_3N_4 thick film can withstand continuous exposure to air and corrosive materials at high temperatures for an extended period of time. The deposition of Si_3N_4 using the PECVD technique results in a film that owns better adhesion, better isolation and insulation, good step coverage and uniformity. All areas except the electrodes and bonding pads were covered with Si_3N_4 .

3.5 Sensors' Profiling and Problem Definition

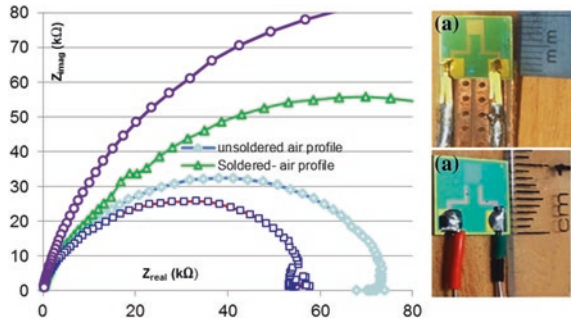
Capacitive affinity sensors and transducers could be constructed by fabricating the thin film electrodes with a choice of materials on a number of substrates; and immobilizing analyte recognition compounds in the form of thin layers on the sensing surfaces, electrodes or between the electrodes. EIS is used to deduce the changes taking place in the electrochemical system in general and observe the changes in the conductance and capacitance at the sensing surface, interface and layers, in particular. The consequent changes in the dielectric properties or capacitive variations when an analyte binds to the molecular recognition sites could be measured [8, 16]. In order to ensure the system linearity, stability and repeatability, this method is rendered viable only for a stable and reversible system in equilibrium. For this reason, instantaneous impedance measurements are mandatory for non-stationary systems [11]. The electrode-electrolyte interface capacitance dominates at a low incident frequency. Therefore, the system displays high sensitivity towards biochemical-recognition events induced capacitive variations at electrode-electrolyte interface which seems to be a merit point for the applied technique [17].

Unfortunately, the large scale of sensitivity renders poor reproducibility and temperature instabilities to the system which changes its parameters even in the testing duration [18–20]. Among many factors like humidity, pH, and test time, etc. it was observed that temperature and surface roughness of the electrode surface are the most vital factors causing instability, and there is a critical requirement of inducing immunity in the sensor against these parameters in order to produce stability, reproducibility and robustness in the sensing system for practical applications [16].

3.5.1 Connection Pads Soldering

Soldering connecting wires to connection pads of the sensors revealed that the sensors' profile change as soon as the sensor is exposed to an amount of heat above the eutectic temperature of gold and chromium. This proved to be an irreversible change in the impedance reading capability of the transducer. At 300 °C large fraction of Chromium diffuses into the thin gold layer and the soldering temperature approaches that limit with 60:40 composition of Tin (Sn) and Lead (Pb), respectively, in solder [21, 22].

Fig. 3.19 Impedance characteristics using the same sensor before (a) and after (b) soldering



In order to investigate the problem, a selected sensor was profiled for impedance characteristics in the air and deionized water. Later, it was re-profiled in same test samples after soldering wires to the connection pads. An average of three sets of impedance measurement was plotted in each case, and all the experiments were carried out at identical humidity (44 %) and temperature (23.3 °C) conditions for all experiments. The Cole-Cole plot in Fig. 3.19 shows the shift in the impedance measurements for the same sensor before and after soldering. This initial investigation on the problem led to a detailed study of the fabrication process and understanding the Physics of thin film fabrication by magnetron sputtering [23]. Next section provides a detailed account of the research and development in order to achieve stability in the impedance measurements.

3.6 Performance Evaluation

3.6.1 Experimental Evaluation

Two sensors 1-1-50A and 1-1-50B were selected from the fabricated wafer for time series profiling in air under same temperature and humidity conditions. Both sensors were identical in terms of design; fabricated with repeated patterns of single excitation and single sensing electrodes and spatial wavelength of 50 μm . The connection pads were clipped in gold plated clipping pins to form a connection with the Hioki 3522-50 LCR Hi Tester as shown in Fig. 3.18b. Figure 3.20 displays the inconsistency in impedance measurements by 1-1-50B at different times in the presence of identical atmospheric conditions at all times in a lab setup. Figure 3.21 shows the Nyquist plot for sensor 1-1-50A at 44 % humidity and 23.3 °C temperature at different times mentioned against each measurement. The Same unreliability of measurements can be seen this case too that was observed for 1-1-50B shown in Fig. 3.20.

It is evident from the plots that despite the constant testing parameters the fabricated sensors are not stable in measuring impedance.

Fig. 3.20 Cole-Cole plot for 1-1-50B 'as is' fabricated sensor's test in air at 44 % humidity and 23.3 °C temperature at different times

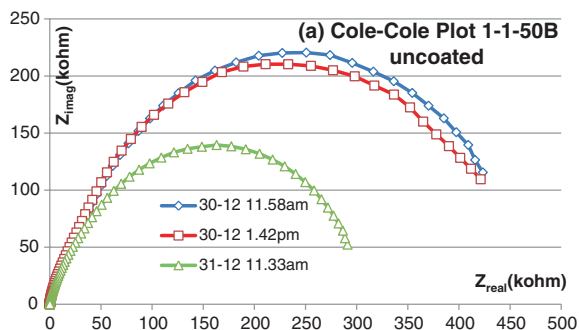
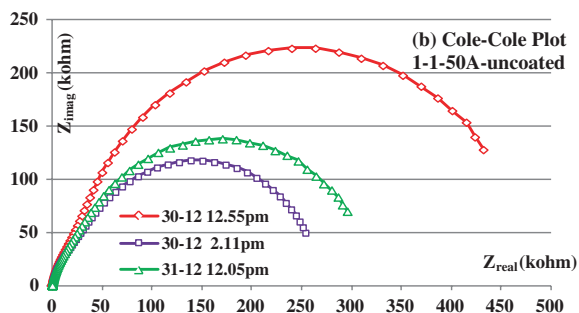


Fig. 3.21 Cole-Cole plot for 1-1-50A sensor's test in air at 44 % humidity and 23.3 °C temperature at different times



It should be noted that each plot is an average of three measurements, and the test equipment was set up to operate in a slow mode to keep the measurement error less than 0.05 %. Test leads' stray capacitance error was normalized by using device's built-in open and short calibration algorithm. The algorithm measures the test leads capacitance in open and short circuit configurations and use this information to eliminate the noise from the measured values using mathematical methods and accuracy equations as mentioned in the device manual [24]. The impedance plots so obtained verify the stability and reproducibility issues as pointed out in Sect. 3.5 of this manuscript. This kind of challenges have limited the commercial use of the impedimetric sensors and despite two decades of research efforts and hundreds of publications, not any product, based on impedance spectroscopy, has achieved widespread commercial success [25, 26]. Serious efforts are lately being made to overcome the dilemma of stability and reproducibility [19, 23].

3.7 Achieving Stability in Sensors' Performance

In this part of presented research, the stability and reproducibility issue of the printable thin film interdigital electrodes have been addressed by looking into the physical and material aspects of the thin film deposition protocols of electrodes.

Surface energies and morphology of the deposited/printed thin film electrodes play a significant role in the application of electrochemical impedance spectroscopy technique [10, 11, 27]. Macdonald [10] refers to the early EIS experiments conducted primarily to measure the capacitance of an ideally polarizable mercury electrode in the form of a hanging mercury droplet. Being a liquid metal, the spherical droplet of mercury takes its shape by achieving a balance between the inter-atomic forces and surface energies. This energy balance is responsible for the presence of perfect smooth surface of the mercury droplet. The absence of uneven surface and activation energies renders defect-less surface and bulk lattice structure of the mercury electrode, hence providing stability to the EIS measurements. Stability in the EIS measurement is a function of surface morphology which in turn depends on the surface energies and defect-less lattice structure of the thin film printed electrodes. Scanning Electron Microscopy (SEM) was used in the requirement to understand the surface morphology of the DC magnetron Argon sputtered gold electrodes for the fabricated sensor. Figure 3.22 shows the SEM image of the bare electrode showing grains of the sputtered gold on the electrode surface. Usually, gold does not display good adhesion to the silicon substrate. Gold, on the other hand, is the most commonly used electrode material for sensing application due to its excellent physiochemical stability, biological affinity, low electrical resistivity inevitable for impedance spectroscopy measurements and high reflectivity required for optical sensors. In order to deposit Gold on Si substrate, the deposition of a seed layer such as Chromium is needed in order to provide better adhesion of Gold on Si wafer. DC magnetron sputtering of Gold over the seed layer of Chromium deposits Gold in the form of grains forming the electrode surface. The grain size depends on the rate of sputtering of Gold due to Argon [28]. Even at extremely slow rates of argon, flow the sputtered metal deposits in the form of grains which is the major cause of surface defects and unbalanced surface energies at the electrode surface [29].

The use of Argon plasma sputtering for gold deposition is a low-cost method most commonly employed in the semiconductor fabrication industry.

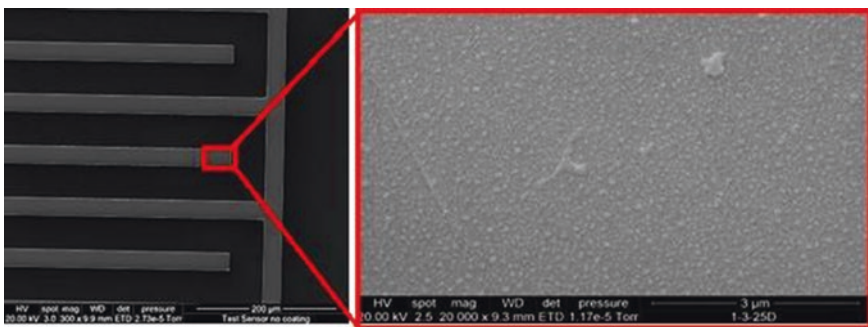


Fig. 3.22 SEM image of the fabricated electrode shows roughness of electrodes due to DC magnetron sputtering process

3.7.1 Post-fabrication Anneal of ID Sensor

Due to the physics of the deposition procedure, lattice structure defects are created within the sputtered gold thin film electrodes [29]. Semiconductor industries follow an extended set of proceedings to fabricate an electronic device including multiple cleaning, annealing and sintering processes. These necessary procedures help to remove the lattice defects automatically during the fabrication processes. In this case, the sensor fabrication procedure does not involve any annealing step; therefore, the defects in the lattice structure of the gold electrodes are not removed which affect the performance of the sensor. A therapeutic post-fabrication heat treatment was applied to the sensor to achieve improvement in its performance, but keeping the fabrication cost to the bare minimum level. A combination of sputtered gold electrodes deposition and post-annealing procedure served the dual purpose of low cost and better performance of the sensor.

In order to equalize the surface energies and remove the defects from the electrode surface, temperature annealing is the most cited method in material science research [22, 28]. The energy required to eliminate a defect on an electrode surface held at a constant potential is the difference in surface tension per defect on a surface with defect γ_d and surface without defect γ_0 . The work done required to eliminate a defect at the solid interface at constant potential is given by:

$$E_{d(\phi)} = E_d^0 - \lim_{\rho \rightarrow 0} \frac{1}{\rho} \left\{ \int_{\phi_{pz}}^{\phi} (\sigma_d^+(\phi') - \sigma_d(\phi')) d\phi' \right\} \quad (3.6)$$

where, ϕ is the electrode potential, σ is the surface charge density and ρ is the density of defects on the surface. Analog to Eq. 3.6 the activation energy required to transport atom on the surface is given as:

$$E_{d(\phi)} = E_d^0 - \lim_{\rho \rightarrow 0} \frac{1}{\rho} \left\{ \int_{\phi_{pz}}^{\phi} (\sigma_d^+(\phi') - \sigma_d(\phi')) d\phi' \right\} \quad (3.7)$$

$\sigma_d^+(\phi')$ is the charge density on the surface with defects in the activated transition state. Generalizing surface charge densities around a particular potential ϕ_0

$$\sigma_d(\phi) = \sigma_d(\phi_0) + C_d(\phi_0)(\phi - \phi_0) \quad (3.8)$$

$$\sigma_0(\phi) = \sigma_0(\phi_0) + C_0(\phi_0)(\phi - \phi_0) \quad (3.9)$$

$C_d(\phi_0)$ and $C_0(\phi_0)$ are the differential capacitance of the surface with and without defects. Using Eqs. 3.6, 3.8 and 3.9:

$$E_d(\phi) = E_d^0 - \lim_{\rho \rightarrow 0} \frac{1}{\rho} \left\{ \sigma_d(\phi_0) - \sigma_0(\phi_0)(\phi - \phi_0) + \frac{1}{2} \left(C_d(\phi_0) - C_0(\phi_0)(\phi - \phi_0)^2 \right) \right\} \quad (3.10)$$

At a small potential, the defect energies behave as linear function of the potential difference. This holds good for the activation energies required for defect transport process too [30, 31].

The annealing temperature and time are the most important parameters in this regards. Annealing temperature was set to reach 210 °C in seven steps of 30 °C each considering presence of both Gold and Chromium thin films on the sensor surface. At 300 °C large fraction of chromium diffuses into thin gold layer, consequently increasing the resistivity of the electrodes that may lead to poor circuit characteristics [21]. 210 °C was set as a trade-off between electrode surface defects' removal and avoid unwanted diffusion of Cr into gold to keep the resistivity of the electrodes to a minimal level. In order to observe the changes in the sensing characteristics with temperature the sensor was set in the vacuum oven and the oven was programmed to start from 30 °C, anneal the sensor for one hour and raise the temperature to 60 °C at a rate of 10 °C per minute. Anneal again for one hour and increase temperature to 90 °C at the same rate and so on. At the end of each annealing step, impedance measurements were taken twice before the oven moves to next temperature range. Annealing process of the sensor was carried out in a vacuum oven in order to avoid oxidation of electrodes and silicon surface (Fig. 3.23).

Fig. 3.23 Annealing sensors in vacuum oven in micro-suit



3.7.2 Results' Validation

The plot of all the impedance measurements taken during annealing procedure is given in Fig. 3.24. Consequent to the annealing procedure, the sensor was tested again under initial humidity condition in order to observe its behaviour. The impedance measurements were taken in duplicate at different times and temperatures in a pre-heated oven. A maximum of 90 °C was reached to avoid oxidation at a higher temperature. Figure 3.25 shows the impedance plot for the annealed sensor at 30, 60 and 90 °C.

It is evident from Fig. 3.25 that annealing has affected the profile of the sensor in a forceful manner. The sensor behaves identically under same temperature and humidity conditions while profiled at two different times at a lapse of one hour, which is quite promising in terms of stability and repeatability of the impedimetric measurements. The SEM image of the electrode surface, after annealing, shows highly smooth electrode surface as displayed in Fig. 3.26 SEM image of electrode before (a) and after (b) anneal (b). It should be noted that a dust particle was focused on the SEM image to provide depth and contrast to observe surface smoothness. For comparison, the SEM image of same part of the electrode surface is given in Fig. 3.26a. It is evident from the figures that even at a resolution of 40,000 the electrode surface appears smooth without any grains and grain boundaries.

3.7.3 Complex Nonlinear Least Squares Curve Fitting

Electrochemical spectrum analyser algorithm was used to deduce the equivalent circuit and component parameters by fitting the experimental data to its theoretically

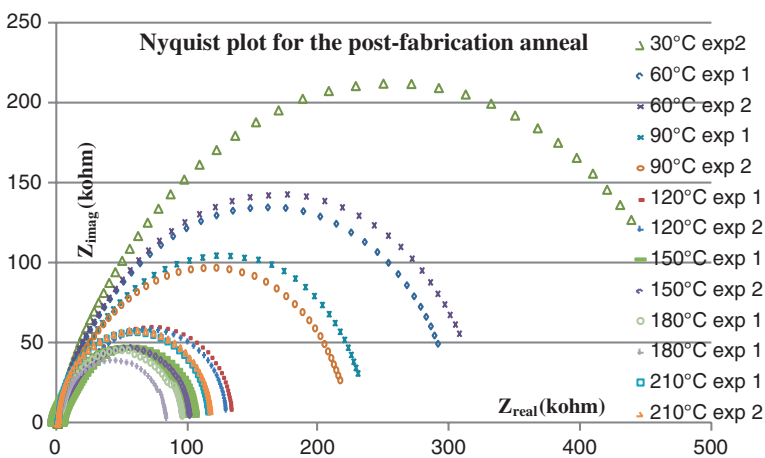


Fig. 3.24 Nyquist plot for EIS during annealing process at 30, 60, 90, 120, 150, 180, and 210 °C

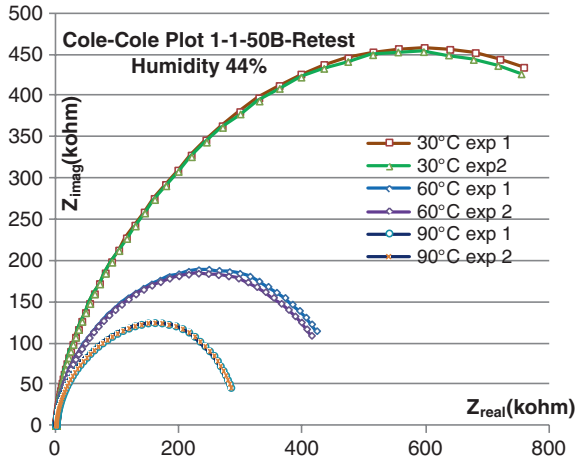


Fig. 3.25 Nyquist plot for improved performance annealed sensors at initial temperature and humidity conditions

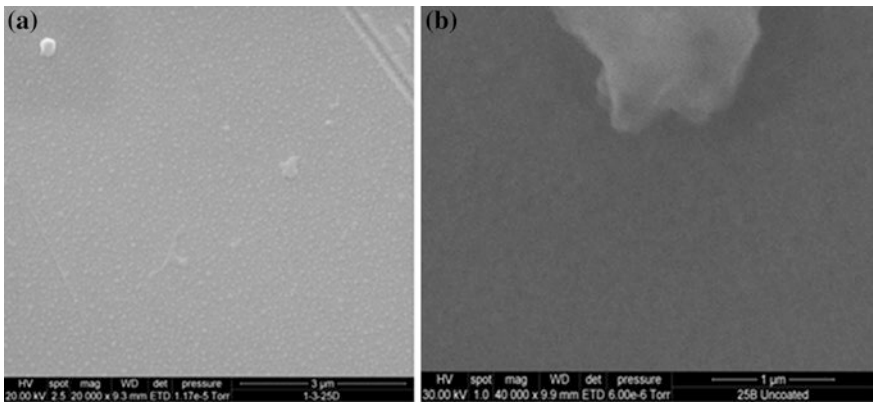


Fig. 3.26 SEM image of electrode before (a) and after (b) anneal

estimated response based on Randle’s model. The algorithm performs statistical analysis to calculate the residual mean square $r_{amplitude}^2$ for experimentally observed values in measured spectra by complex nonlinear least square using following relation [32, 33].

$$r_{amplitude}^2 = \sum_{i=1}^N \frac{(Z'_{iobs} - Z'_{icalc})^2 + (Z''_{iobs} - Z''_{icalc})^2}{Z'_{iobs}{}^2 + Z''_{iobs}{}^2} \tag{3.11}$$

Table 3.3 Component parameters for the best fit circuit ($r_{amplitude}^2 = 1E-4$)

Temp	30 °C	60 °C	90 °C	120 °C	150 °C	180 °C	210 °C
C1 (nF)	0.768	0.818	0.533	1.07	1.80		
C2 (nF)				1.28	0.92		
R1 (Ω)	2.88E-06	2.68E-10	1.96E-13	1.39E+01	3.12E-01	3.54E-02	6.84E-02
R2 (Ω)	0.226 M	0.108 M	0.056 M	6.33	0.217 k	3.93 k	9.51 k
R3 (Ω)	0.176	7.17	3.15	2.40 k	4.99 k	15.52 k	17.6 k
W1 (Ω)	5.43E-12	3.26E-13	4.10E-14	1.15E-15	2.19E-18	5.19E-12	1.49E-13
W2 (MΩ)				1.49	2.06		
CPE1	1.50E-08	1.59E-08	8.42E-09	2.93E-05	4.40E-05	4.85E-09	2.98E-08
CPE2						3.80E-09	3.80E-09

where

Z'_{iobs} is the observed real impedance

Z'_{icalc} is the calculated real impedance

Z''_{iobs} is the observed imaginary impedance

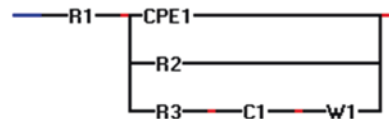
Z''_{icalc} is the calculated imaginary impedance

$r_{amplitude}^2$ determines the deviation of the experimentally observed data from the optimal solution. Table 3.3 shows components' parameters for optimal curve fitting of the experimental data averaged over three fittings. An interesting observation made was that the sensor's response to the fitted circuit model changed with the change in annealing temperature.

It followed one circuit model in the temperature range 30–90 °C, another model for 91–150 °C and a third model for 151–210 °C. Figures 3.27, 3.29 and 3.31 show the equivalent circuits EC1, EC2, and EC3 suggested by the CNLS algorithm for temperature range 30–90 °C, 91–150 °C and for 151–210 °C respectively. Figures 3.28, 3.30 and 3.32 show the fitted Nyquist plots for EC1, EC2, and EC3 by the CNLS algorithm for temperature range 30–90 °C, 91–150 °C and for 151–210 °C respectively. It should be noted that $r_{amplitude}^2$ for each fitting is of the order of magnitude 10^{-4} achieved with 300 iterations.

The analysis shows that the annealing of the sensor is driving the profile of the electrodes from a single time constant circuit to a circuit of twin time constants, which could be attributed to the migration of defects on the electrode surface caused by gradually created balance between the inter-atomic forces and surface energies in the thin film electrodes. At high temperature, the Si semiconductor substrate becomes more conductive due to increased rate of electron-hole pairs formation inside the single crystal silicon substrate. It behaved as conducting

Fig. 3.27 EC1 CNLS equivalent circuit for 30–90 °C



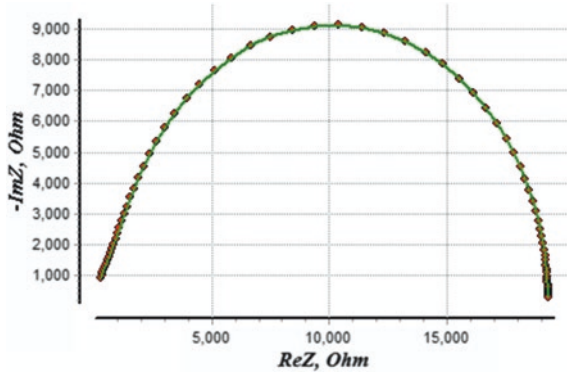


Fig. 3.28 EC1 fitted curve (30–90 °C)

Fig. 3.29 EC2 CNLS equivalent circuit for 91–150 °C

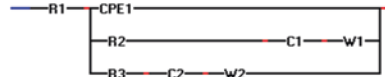


Fig. 3.30 EC2 fitted curve (91–150 °C)

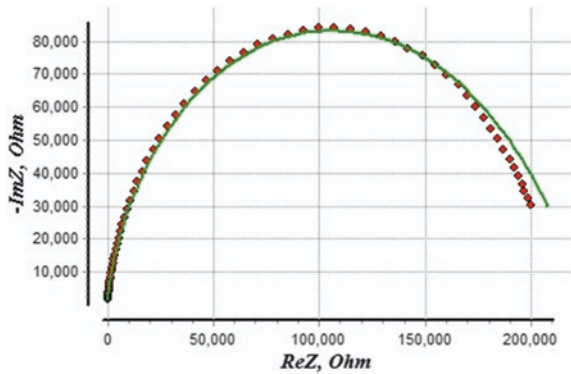


Fig. 3.31 EC3 CNLS equivalent circuit for 151–210 °C

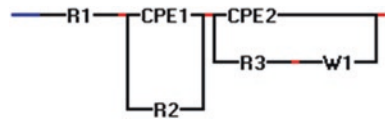


Fig. 3.32 EC3 fitted curve
(151–210 °C)

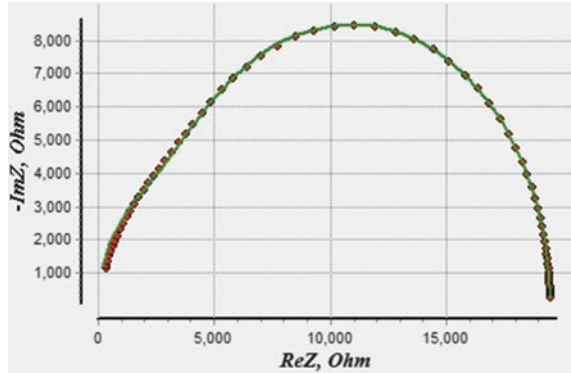


plate of a parallel plate capacitor with an insulative oxide layer of SiO_2 acting as a dielectric between electrodes giving rise to capacitive constant phase element. Constant Phase Elements (CPE1 and CPE2) behave as two capacitors connected in series separated by an insulation layer of the SiO_2 present on both sides of the sensor. The SiO_2 layers behave as R2 and R3 as shown in the equivalent circuit.

3.7.4 Principal Component Analysis (PCA)

Traditional analysis method requires separate examination between different circuit variable, for example, between constant phase element (CPE) parameter and time or resistance parameter and time on a two-dimensional plot, which can be misleading in the determination of valuable abstract mathematical correlations hidden in the impedance parameters. A better approach of PCA explores the orthogonal linear combinations of the original variables. These combinations, termed as principal components, represent different aspects of system variables and are helpful by eliminating redundancy and reduce noise in the data [33–35].

Principal component analysis is a statistical tool based on multivariate data analysis, introduced in 1901 by Pearson [36]. Later, Hotelling in 1933, further developed PCA independently [37]. PCA is a technique that reduces the dimensionality of a data set by linearly combining the original variables, in order to generate new axes known as principal components [38]. Each linear combination defines the variance in the data set, and then all linear combinations are uncorrelated to others. Eigenvalue associated with each principal component is a measure of variation in a dataset. Eigenvectors, usually expressed as a percentage of the total variation, are just linear combinations of the original variables (in the simple or rotated factor space) that described how variables “contribute” to each factor axis. Therefore, the PCA can be executed in five steps; Subtract the mean to produce a data set whose mean in zero; calculate the covariance matrix (or correlation); compute the eigenvectors and eigenvalues of the covariance matrix; choose

components and form a feature vector; and derive the new data set of less number of variables with redundant variables being truncated. PCA has been used to minimize dimensionality of data in impedance spectroscopy analyses by eliminating redundancy of data and without loss of information and without requiring substantial knowledge of test conditions for the impedance system under investigation [33, 39, 40].

IBM-SPSS PCA was applied to analyse various quality states of the system during annealing.

3.7.5 PCA Analysis—ECI (30–90 °C) Anneal

Complex nonlinear least squares curve fitting algorithm suggested Equivalent circuit I (EC1) by fitting the experimental data on hypothetically calculated electrical circuit representing electrochemical processes taking place inside the electrochemical cell. The suggested circuit displays six circuit components shown in Fig. 3.27. The variance in Table 3.4 displays 99.13 % cumulative eigenvalues for the system, explained by four principal components, pointing out the system scattering. The component plot shown in Fig. 3.33 displayed high variance and weak correlations of equivalent circuit components.

Physically, the instability observed in the impedance measurements executed by the as-is fabricated sensor depicts the system scattering evaluated by the PCA in the lower temperature range. The scree plot for EC1 is given in Fig. 3.34.

Principal component analysis of equivalent circuit I, that was deduced from the experimental results obtained at temperatures 30, 60 and 90 °C, portrays a system with high scattering. The system variables were scattered in four directions with a maximum convergence of 55.3 % observed in the first eigenvector. The second vector displayed a convergence of 19.8 %, third showing 13.67 % and the fourth one showed only 10.2 %. Due to the scattering of the system variables, the system did not display stability in the impedance measurements when tested with a sample ad depicted in the test results of 1-1-50A and 1-1-50B shown in Figs. 3.20 and 3.21 respectively. Interpreting these findings in terms of Physics and surface morphology of the electrodes, the PCA results show that although the

Table 3.4 Table of variance ECI (30–90 °C) anneal

PCA comp	Initial eigenvalues			Extraction sums of squared loadings		
	Total	% variance	Cumulative %	Total	% variance	Cumulative %
1	3.321	55.347	55.347	3.321	55.347	55.347
2	1.191	19.842	75.190	1.191	19.842	75.190
3	0.820	13.673	88.863	0.820	13.673	88.863
4	0.616	10.272	99.135	0.616	10.272	99.135
5	0.052	0.865	100.000	0.052	0.865	100.000
6	–1E–013	–1E–013	100.000	1E–013	1E–013	100.000

Fig. 3.33 Component plot
ECI (30–90 °C) anneal

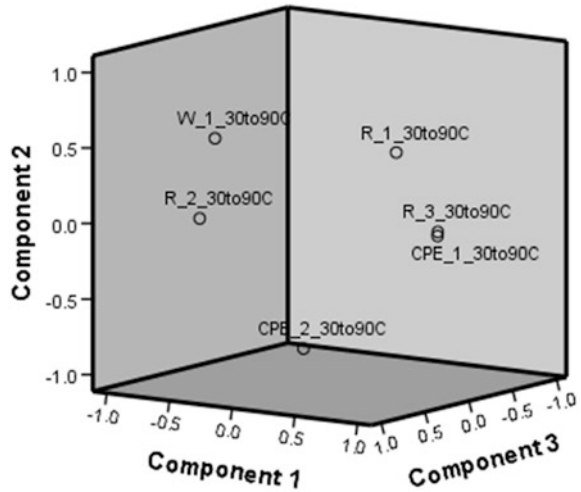
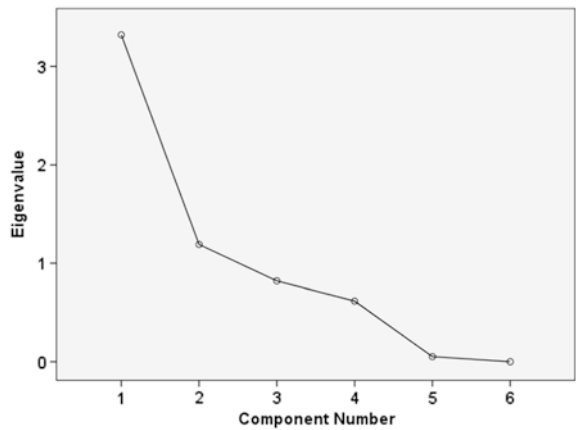


Fig. 3.34 Scree plot ECI
(30–90 °C) anneal



system has absorbed energy, yet it is not enough to remove the defects in the electrodes caused by sputtering and the electrodes surface still have grains and grain boundaries.

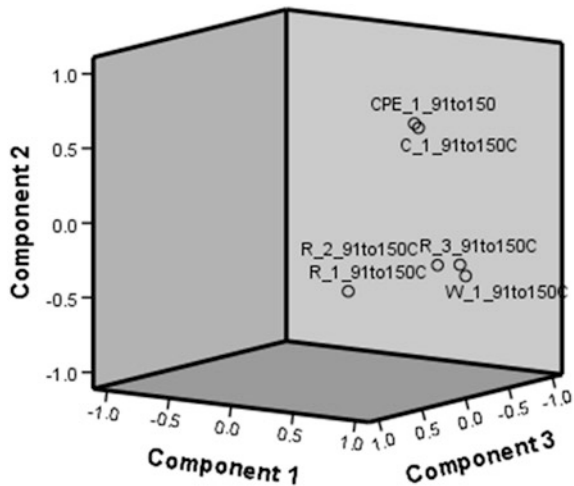
3.7.6 PCA Analysis—EC2 (91–150 °C) Anneal

Equivalent circuit 2 (EC2) displays eight circuit components shown in Fig. 3.29. The variance in Table 3.5 displays 98.422 % cumulative eigenvalues for the system, explained by three principal components. The system still displays scattering but is reduced compared to the scattering displayed by EC1.

Table 3.5 Table of variance EC2 (91–150 °C) anneal

PCA Comp	Initial eigenvalues			Extraction sums of squared loadings		
	Total	% of variance	Cumulative %	Total	% of variance	Cumulative %
1	3.840	63.996	63.996	3.840	63.996	63.996
2	1.310	21.834	85.830	1.310	21.834	85.830
3	0.756	12.593	98.422	0.756	12.593	98.422
4	0.072	1.196	99.619	0.072	1.196	99.619
5	0.021	0.349	99.968	0.021	0.349	99.968
6	0.002	0.032	100.000	0.002	0.032	100.000

Fig. 3.35 Component plot EC2 (91–150 °C) anneal

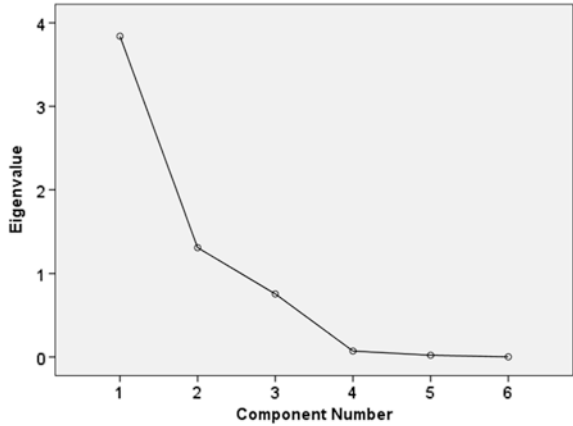


The PCA component plot is shown in Fig. 3.35 that displays mean variance and stronger correlations of equivalent circuit components. The analysis pronounces the system to drift from scattering to the stability of parameters.

The analysis defines three orthogonal eigenvectors to describe the system. PCA component 1 in EC2, only, is now defining 63.996 % of all the defined components as compared to the EC1 that displayed 55.34 %. The scree plot for EC2 is given in Fig. 3.36 that now defines only three elements to explain 99.422 % of system parameters, compared to EC1, which was just 88.863 % of the system variables clustered in three components. Though the entropy of the system is rising due to heat, yet the system is gaining stability in terms of electrical parameters. The physics of the system behaviour could be explained on the basis of energy balances gained due to the equalization of the bulk and surface energies [30].

Principal component analysis of equivalent circuit II, that was deduced from the experimental results obtained at temperatures 120 and 150 °C portrays a system with medium scattering. The system variables have now converged into three

Fig. 3.36 Scree plot EC2 (91–150 °C) anneal



eigenvectors with a percentage of variance 63.99, 21.83 and 12.59 % respectively. The system still displays scattering but relatively less as compared to untreated sensors.

3.7.7 PCA Analysis—EC3 (151–210 °C) Anneal

Equivalent circuit 3 (EC3) displays six components with a two-time constant circuit shown in Fig. 3.31. The variance in Table 3.6 displays 97.258 % cumulative eigenvalues for the system, explained by only two principal components with first component explaining 85.11 % system parameter depicting system convergence to stability. The component plot is shown in Fig. 3.37 depicting the clustered components.

The scree plot for EC1 is given in Fig. 3.38.

It is a proven result that in a set of m eigenvectors of an Eigen matrix, the eigenvectors corresponding to the largest eigenvalues, minimize the mean square reconstruction error over all choices of m orthonormal basis vectors. Such set of

Table 3.6 Table of variance EC3 (151–210 °C) anneal

PCA comp	Initial eigenvalues			Extraction sums of squared loadings		
	Total	% of variance	Cumulative %	Total	% of variance	Cumulative %
1	5.107	85.111	85.111	5.107	85.111	85.111
2	0.729	12.147	97.258	0.729	12.147	97.258
3	0.118	1.960	99.218			
4	0.046	0.769	99.987			
5	0.001	0.013	100.000			
6	1.000E–013	1.005E–013	100.000			

Fig. 3.37 Component plot
EC3 (151–210 °C) anneal

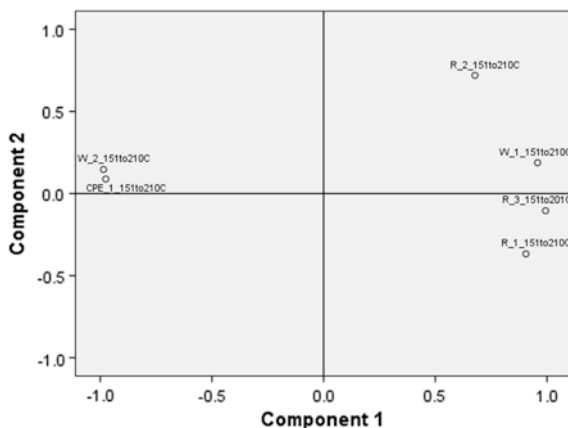
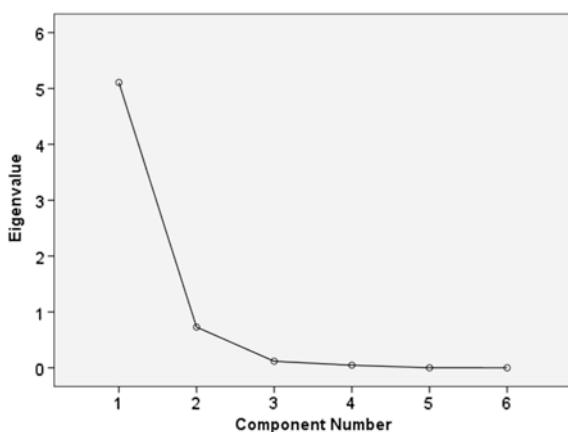


Fig. 3.38 Scree plot EC3
(151–210 °C) anneal



eigenvectors defines the new uncorrelated dimensions of a coordinate system. Therefore, the first principal component with the largest eigenvalues is the most discriminant one [34, 41]. The results obtained as an outcome of the Principal component analysis depict that annealing results in dramatic changes in the electrodes' gold layer morphology and improved surface smoothness. This objective was achieved by providing enough thermal energy to facilitate migration of defects on the gold surface and creating a balance between the surface and bulk energies in the gold lattice.

Švorčík et al. [31] studied the effects of annealing on the gold structures sputtered onto a glass substrate using AFM, UV-VIS and electrical measurements. They reported the formation of structures on the gold surface at 300 °C, which is different in the presented case since the annealing temperature reached is 210 °C, which is merely enough to achieve a balance in surface and bulk energies.

The fabricated post-annealed sensors are currently employed as a biosensor to detect food pathogens and bacteria in meat [33] and as a chemical sensor to detect the presence of endocrine disrupting compounds (EDCs) in beverages up to a trace level as low as two part per billion [42]. The achieved stability in impedance measurements used in conjunction with the characteristic high sensitivity of the sensor declares it a potential candidate for the commercial applications.

3.8 Conclusions

An enormous interest is found in the industrial sector for impedance spectroscopy due to its sensitivity. This requires an innovative approach to select samples, execute impedance measurements and perform data analysis. A reliable transducer is needed to interpret this sensitive technique to gain stability in measurements. The applied approach of designing, simulation and fabrication of interdigital sensors provided a reliable and novel tool for testing and achieving stability and reproducibility of the impedance spectroscopy results. This objective was achieved by providing enough thermal energy to facilitate migration of defects on the gold surface and creating a balance between the surface and bulk energies in the gold lattice.

The next phase of this work was to evaluate the sensitivity of the designed sensor. COMSOL simulations discussed in this chapter declared the highest level of sensitivity for the sensors with multiple (5 and 11) sensing electrodes and pitch length of 50 μm . The practical sensitivity of the designed sensor could be determined, only if, the system is exposed to the in-field tests and investigations. Experiments and analyses conducted in this respect are discussed in the next two chapters. Chapter 4 is dedicated to the test and analyses of the hormones pertaining to the reproductive cycle of the mammals and Chap. 5 discusses the detection of EDCs and reproductive toxins.

References

1. A. Mamishev, Y. Du, B. Lesieutre et al., Development and applications of fringing electric field dielectrometry sensors and parameter estimation algorithms. *J. Electrostat.* **46**(2), 109–123 (1999)
2. E. Bakker, Y. Qin, Electrochemical sensors. *Anal. Chem.* **78**(12), 3965–3984 (2006)
3. M.I. Prodromidis, Impedimetric immunosensors—a review. *Electrochim. Acta* **55**(14), 4227–4233 (2010)
4. S.C. Mukhopadhyay, C.P. Gooneratne, A novel planar-type biosensor for noninvasive meat inspection. *Sens. J. IEEE* **7**(9), 1340–1346 (2007)
5. S. Mukhopadhyay, S.D. Choudhury, T. Allsop et al., Assessment of pelt quality in leather making using a novel non-invasive sensing approach. *J. Biochem. Biophys. Methods* **70**(6), 809–815 (2008)
6. S.C. Mukhopadhyay, C.P. Gooneratne, G.S. Gupta et al., A low-cost sensing system for quality monitoring of dairy products. *Instrum. Meas. IEEE Transac.* **55**(4), 1331–1338 (2006)

7. S.C. Mukhopadhyay, G.S. Gupta, J.D. Woolley et al., Saxophone reed inspection employing planar electromagnetic sensors. *Instrum. Meas. IEEE Transac.* **56**(6), 2492–2503 (2007)
8. X.B. Li, S.D. Larson, A.S. Zyuzin et al., Design principles for multichannel fringing electric field sensors. *Sens. J. IEEE* **6**(2), 434–440 (2006)
9. M.E. Orazem, B. Tribollet, in *Electrochemical Impedance Spectroscopy*. Wiley, New York (2011)
10. D.D. Macdonald, Reflections on the history of electrochemical impedance spectroscopy. *Electrochim. Acta* **51**(8), 1376–1388 (2006)
11. B.-Y. Chang, S.-M. Park, Electrochemical impedance spectroscopy. *Ann. Rev. Anal. Chem.* **3**, 207–229 (2010)
12. A.R.M. Syaifudin, P. Yu, S. Mukhopadhyay et al., in *Performance Evaluation of a New Novel Planar Interdigital Sensors*, pp. 731–736
13. A.I. Zia, A. Mohd Syaifudin, S. Mukhopadhyay et al., in *Development of Electrochemical Impedance Spectroscopy Based Sensing System for DEHP Detection*, pp. 666–674
14. A.I. Zia, A.R. Mohd Syaifudin, S.C. Mukhopadhyay et al., in *MEMS Based Impedimetric Sensing of Phthalates*, pp. 855–860
15. A.I. Zia, A.M. Syaifudin, S. Mukhopadhyay et al., Electrochemical impedance spectroscopy based MEMS sensors for phthalates detection in water and juices. *J. Phys: Conf. Ser.* **439**, 012026 (2013)
16. S.E. Creager, L.A. Hockett, G.K. Rowe, Consequences of microscopic surface roughness for molecular self-assembly. *Langmuir* **8**(3), 854–861 (1992)
17. S.M. Radke, E.C. Alocilja, A microfabricated biosensor for detecting foodborne bioterrorism agents. *Sens. J. IEEE* **5**(4), 744–750 (2005)
18. D. Grieshaber, R. MacKenzie, J. Voros et al., Electrochemical biosensors—sensor principles and architectures. *Sensors* **8**(3), 1400–1458 (2008)
19. L. Ianeselli, G. Greci, C. Callegari et al., Development of stable and reproducible biosensors based on electrochemical impedance spectroscopy: three-electrode versus two-electrode setup. *Biosens. Bioelectr.* (2013)
20. M. Kitsara, D. Goustouridis, S. Chatzandroulis et al., Single chip interdigitated electrode capacitive chemical sensor arrays. *Sens. Actuators B: Chem.* **127**(1), 186–192 (2007)
21. J. Rairden, C. Neugebauer, R. Sigsbee, Interdiffusion in thin conductor films—chromium/gold, nickel/gold and chromium silicide/gold. *Metall. Transac.* **2**(3), 719–722 (1971)
22. V. Švorčík, O. Kvítek, O. Lyutakov et al., Annealing of sputtered gold nano-structures. *Appl. Phys. A* **102**(3), 747–751 (2011)
23. A. Zia, S. Mukhopadhyay, P. Yu et al., Post annealing performance evaluation of printable interdigital capacitive sensors by principal component analysis. *Sens. J. IEEE* **99**, 1–1 (2014)
24. E.C. Hioki, *HIOKI 3532-50 LCR HITESTER instruction manual* (HIOKI EE CORPORATION, JAPAN, 2001)
25. F. Lisdat, D. Schäfer, The use of electrochemical impedance spectroscopy for biosensing. *Anal. Bioanal. Chem.* **391**(5), 1555–1567 (2008)
26. Y.X. Wang, Z.Z. Ye, Y.B. Ying, New trends in impedimetric biosensors for the detection of foodborne pathogenic bacteria. *Sensors* **12**(3), 3449–3471 (2012)
27. J.E.B. Randles, Kinetics of rapid electrode reactions. *Discuss. Faraday Soc.* **1**, 11–19 (1947)
28. D. Hyman, M. Mehregany, Contact physics of gold microcontacts for MEMS switches. *Compon. Packag. Technol. IEEE Transac.* **22**(3), 357–364 (1999)
29. J.M. Delgado, J.M. Orts, J.M. Pérez et al., Sputtered thin-film gold electrodes for in situ ATR-SEIRAS and SERS studies. *J. Electroanal. Chem.* **617**(2), 130–140 (2008)
30. M. Giesen, G. Beltramo, S. Dieluweit et al., The thermodynamics of electrochemical annealing. *Surf. Sci.* **595**(1), 127–137 (2005)
31. V. Švorčík, J. Siegel, P. Šutta et al., Annealing of gold nanostructures sputtered on glass substrate. *Appl. Phys. A* **102**(3), 605–610 (2011)
32. A.I. Zia, M.S.A. Rahman, S.C. Mukhopadhyay et al., Technique for rapid detection of phthalates in water and beverages. *J. Food Eng.* (2013)

33. M.S. Abdul Rahman, S.C. Mukhopadhyay, P.-L. Yu et al., Detection of bacterial endotoxin in food: New planar interdigital sensors based approach. *J. Food Eng.* **114**(3), 346–360 (2013)
34. A. Miszczyk, K. Darowicki, Multispectral impedance quality testing of coil-coating system using principal component analysis. *Prog. Org. Coat.* **69**(4), 330–334 (2010)
35. M.A.M. Yunus, S.C. Mukhopadhyay, S. Ibrahim, Planar electromagnetic sensor based estimation of nitrate contamination in water sources using independent component analysis. *Sens. J. IEEE* **12**(6), 2024–2034 (2012)
36. K. Pearson, LIII. On lines and planes of closest fit to systems of points in space. *Lond. Edinburgh, Dublin Philos. Mag. J. Sci.* **2**(11), 559–572 (1901)
37. H. Hotelling, Analysis of a complex of statistical variables into principal components. *J. Educ. Psychol.* **24**(6), 417 (1933)
38. I. Jolliffe, in *Principal Component Analysis*. Wiley Online Library (2005)
39. H.-R. Tränkler, O. Kanoun, M. Min et al., Smart sensor systems using impedance spectroscopy. *Proc. Estonian Acad. Sci. Eng* **13**(4), 455–478 (2007)
40. A. Mohd Syaifudin, S.C. Mukhopadhyay, P.-L. Yu et al., Measurements and performance evaluation of novel interdigital sensors for different chemicals related to food poisoning. *Sens. J. IEEE* **11**(11), 2957–2965 (2011)
41. C.A. Olivati, A. Riul Jr, D.T. Balogh et al., Detection of phenolic compounds using impedance spectroscopy measurements. *Bioprocess Biosyst. Eng.* **32**(1), 41–46 (2009)
42. A.I. Zia, M.S.A. Rahman, S.C. Mukhopadhyay et al., Technique for rapid detection of phthalates in water and beverages. *J. Food Eng.* **116**(2), 515–523 (2013)

Chapter 4

Electrochemical Detection of Hormones

4.1 Introduction

The objective of this chapter is to investigate the capability of the designed sensors, and to explore the analytical powers of electrochemical impedance spectroscopy, in the detection of different hormones. The target hormones are related to the reproductive cycle of mammals. ‘Non-invasiveness of methodology’ and ‘real-time measurements of samples’ were the prime objectives of this research project. These characteristics of the presented research make this work unique in comparison to all available contemporary methodologies. Apart from that, it was envisaged that execution of the hormone quantification assay should be simple enough to be adapted by a common user without requiring a necessary scientific background.

The first part of this chapter discusses the application of the proposed system to detect estrone glucuronide, an excretory metabolite of estradiol, commonly known as E1G. This hormone plays a significant role in the reproductive fertility of human female. The information on the quantity of excretion of this hormone metabolite is useful in determining the window of fertility for a human female. The handy availability of this information is essential to achieve conception or contraception in the human reproductive cycle.

The second part of the chapter deals with the sensor’s response in the detection of progesterone hormone excreted in the milk of dairy cows. Obtaining urine samples, to gather the fertility information, is not feasible in the case of dairy animals. Though, milk owns a complex chemical matrix, yet it is the easiest and most non-invasive method to achieve the information on ‘window of fertility’ for the animal.

Electrochemical impedance analyses making use of bode plots, Nyquist plots, CNLS curve fitting, electrochemical equivalent circuit parameters and sensitivity of the sensor toward the analytes are discussed in this chapter.

4.2 Detection of Ovarian Hormone Estrone Glucuronide (E1G)

4.2.1 Motivation

The reproductive fertility of human male stays active for nearly all his adult life whereas woman's fertility is periodic and disappears completely at the later age of her life. The 'window of fertility' is termed for a part of the ovulatory menstrual cycle of a woman in which she owns the potential to conceive and reproduce. This period begins up to six days before and ends one day after ovulation. It is clinically determined by a series of ultrasound scans of the ovary or by a series of blood analysis comparing patterns of secretions of ovarian hormones estradiol, progesterone and luteinizing hormone (LH) [1, 2]. Analysis of the rate of excretion of hormonal metabolites, estrone glucuronide (EG) and pregnanediol glucuronide (PG) in urine has an advantage of being non-invasive over the serum analysis and has proved to be more closely correlated to the hormonal concentration in ovary. A marked rise of estradiol production occurs 36 h before ovulation followed by a peak of LH secretion which occurs 17 h before ovulation at average [2]. Classic mean curves for each hormone plotted after a hormonal study of 25 women is shown in Fig. 4.1 [1].

It is clinically agreed that the first rise in one out of three urinary metabolites of estrogen, E1G, is a natural marker for start of fertility window; it is not accepted the best maker widely for the beginning of fertility by the researchers, though [3, 4].

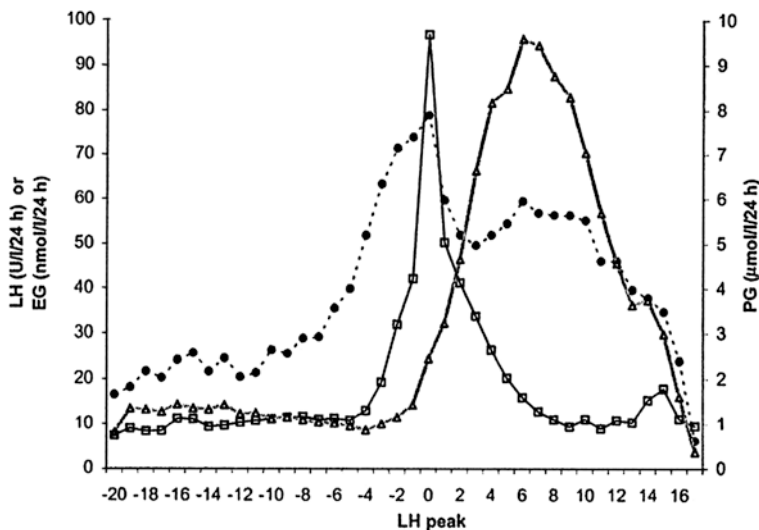


Fig. 4.1 Mean hormonal values of estrone glucuronide (EIG) (-•-), LH (-□-), and pregnanediol glucuronide (PG) (-△-) by cycle day throughout 78 ovulatory cycles from 25 women [1]

Presently, Radioimmunoassay (RIA) is the most commonly used method among the existing laboratory-based techniques to measure E1G and LH in urine samples in order to detect the beginning of the fertility in women. With an advantage of being the most accurate, this assay has major drawbacks of producing radioactive waste, expensive, time consuming along with a requirement of trained professionals carrying out the immunoassay in a laboratory environment under stringent conditions.

4.2.2 Point-of-Care Methods

The other methods currently in practice for the detection of fertility include Basal Body Temperature (BBT), Billings Ovulation Method, Symptothermal Method (STM) and Ovarian Monitor use. These methods serve as a tool to predict the window of fertility information in human females. The gathered information is equally useful for family planning as well as conception and pregnancy.

4.2.3 Basal Body Temperature Method (BBT)

During ovulation, the body temperature elevates by 0.2 °C for three days in comparison to the preceding six days of mensuration cycle. A special thermometer measures the BBT throughout each cycle to predict fertility starting from the 1st day of elevated temperature [5]. This data recording helps to estimate the window of fertility in women.

4.2.4 Billings Ovulation Method

This is a track and record method of checking the amount and quality of cervical mucus. Ovulation occurs within one or two days of the peak day of abundant wet and stretchy cervical mucus [6]. This method does not involve any scientific hormonal measurement yet provides training to predict fertility by track and record [5].

4.2.5 Symptothermal Method (STM)

This method is a combination BBT and Billings Ovulation Method to predict probable fertility window during each cycle [5]. Data is recorded after checking the amount and quality of cervical mucus in addition to the tracking of the elevated body temperature by basal body temperature measurements throughout the

ovulation period. This method involves the scientific body temperature measurements and track and record of the amount and thickness of the cervical mucus in order to predict a window of fertility in human females.

4.2.6 Ovarian Monitor

The Ovarian Monitor is used to measure E1G and PdG in urine samples. It uses pre-coated assay tubes following the principle of homogeneous enzyme immunoassay in a home or in a point-of-care environment. In this immunoassay, an antibody to a ligand specifically inhibits the enzyme activity of an enzyme-ligand conjugate to measure the E1G in the urine sample [7–9]. The Ovarian Monitor system uses a specially designed piece of handheld electronic device that is a rate colorimeter thermostatted at 40 °C with timer settings for the warm-up and enzyme reactions. The display read-out is given in three digits and is related to light transmission $\times 1000$. The device provides single instrument solution for a single assay that is tailored for home or point-of-care use. For multiple assays, a 48 assay tubes accommodative heating block fitted with a thermostat is supplied. The electronic read-out and measuring device is used as a colorimeter, and the assay timings are manually performed using a stopwatch. This setup allows up to 48 E1G assays or 20 PdG assays in a single run that can be clinically used. Validation study of Ovarian Monitor has found its results comparable to the laboratory standards [9] and is viewed as an alternative to more costly laboratory testing, but it requires timed urine samples (over 3 h minimum), dilution of urine test samples, takes around 40 min for E1G testing and lack of reusability of the sensor (assay tube).

In the presented research, the author used Electrochemical Impedance Spectroscopy based approach to measure E1G by using a new planar ID capacitive sensor for rapid results without involving any timed samples. The hormonal metabolites could be quantified, without any additional steps of sample preparation, in mere 5 min. The applied sensor can be reused for the next measurement after wash and dry cycle.

4.2.7 Materials and Methods to Detect E1G

Four concentrations of E1G, 8.33, 16.66, 33.33, and 55.55 nmol/L were prepared in a buffer solution. The non-spiked buffer solution was used as control reference for testing E1G samples. The samples were tested immediately after preparation in the laboratory environment at 47 % humidity and 23 °C temperature. The samples were kept refrigerated at 4 °C for further testing. The sensor was immersed in the 2 ml of control buffer solution to create a control reference for the measurement. Particular care was taken to immerse only the sensing part of the sensor in the solution. Figure 4.2 demonstrates the dip testing procedure. The samples were

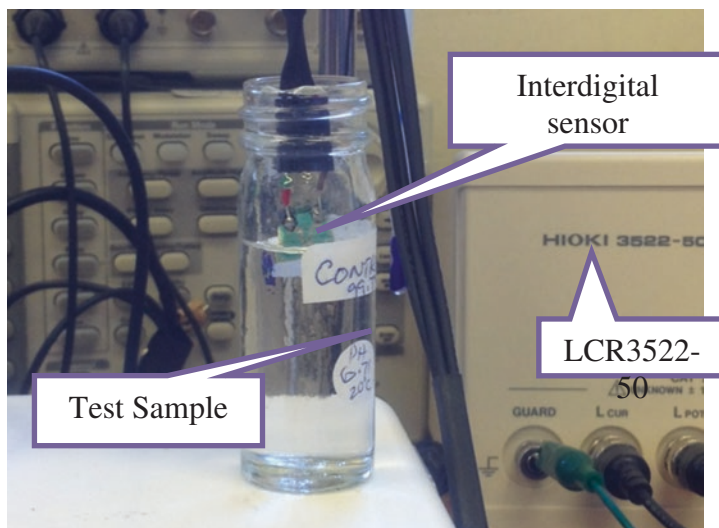


Fig. 4.2 Dip test method for EIG testing

tested in reverse order i.e. lowest to highest concentration in order to avoid saturation of the sensor. The sensor was cleaned with 99.7 % ethanol, rinsed with distilled water and dried with nitrogen after each test. Sensor's profile test in the air was carried out after cleaning procedure, and the results were compared with the reference in order to validate the cleaning procedure and to reset the sensor to its initial conditions.

EIS experiments were carried out using Hioki 3522-50 LCR Hi precision Tester (Japan) at ambient laboratory temperature (23 °C) at a controlled humidity level. All experiments were performed using slow mode of the testing equipment as to achieve an error rate of less than 0.05 % specified by the manufacturer. A sinusoidal signal of $1V_{\text{rms}}$ was applied to the sensor with a frequency sweep of 1 Hz to 10 kHz with 20 data points per decade on the log scale. LabView® data acquisition program was used to write the measured values in Microsoft excel® file for post-processing and analysis of the experimental data on the attached desktop computer. An average of three experiments was used to ensure reproducibility and reliability of the tests' results. Figure 4.3 shows the test bench setup for the experiments.

4.2.8 Results and Discussions

The impedance Z of the sample is determined by applying a small signal perturbation as a function of frequency and subsequent analysis of the resultant current



Fig. 4.3 Laboratory test bench for EIG testing

through the system in terms of amplitude and phase shift compared to voltage-time function. The complex value of impedance can thus be interpreted in terms of its real and imaginary parts at different frequencies. The samples were evaluated for real part (R_e) and Reactance (X) imaginary part of the impedance and were plotted against the excitation frequency for reference and sample solutions as shown in Fig. 4.4. The primary axis shows the average real R_e impedance in $k\Omega$. The real impedance of the sample reads the ionic concentration in the test samples as compared to the control buffer. It is obvious from the plot that as the concentration of EIG increases in the sample solution, the real impedance drops as compared to the preceding concentration. This happens due to a higher concentration of ions in the following sample of higher concentration of EIG. The secondary axis shows the reactance X ($k\Omega$) of the sample solutions plotted against frequency. The change in this parameter is a measure of the dielectric properties of the EIG molecule. The results of an impedance measurement can be graphically demonstrated using bode and Nyquist plot for all applied frequencies with the real part of impedance Z plotted along X-axis, and Imaginary part plotted along Y-axis in the later.

The Nyquist plot for the equivalent circuit comprises a semi-circular region followed by a straight line as shown in Fig. 4.5. The straight line at an angle of 45° represents a faster mass-transfer limited process at lower frequencies, whereas, the semi-circular portion describes a relatively slower charge transfer limited process at higher frequencies. It can be seen from the plot that the diameter of the curve reduces with growing concentration of EIG, indicating an increase in the conductance of the samples. The values of the charge transfer resistance decreased with

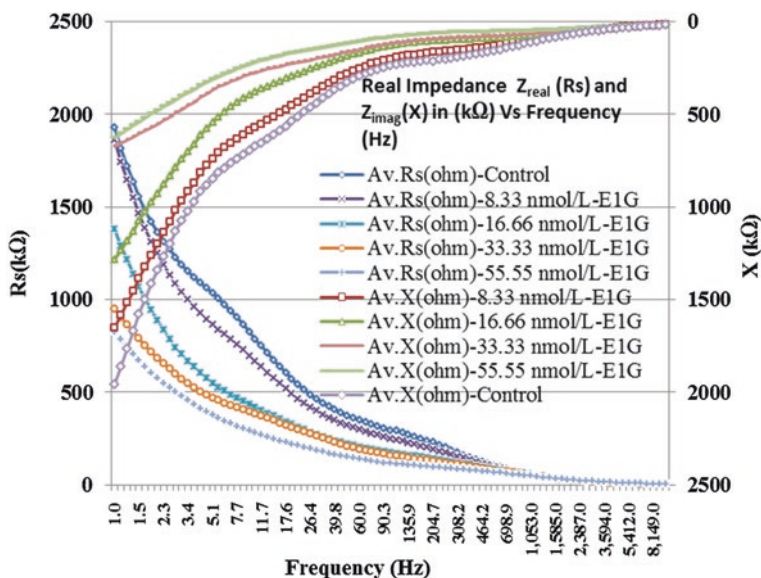


Fig. 4.4 Real and imaginary parts of the measured impedance for E1G

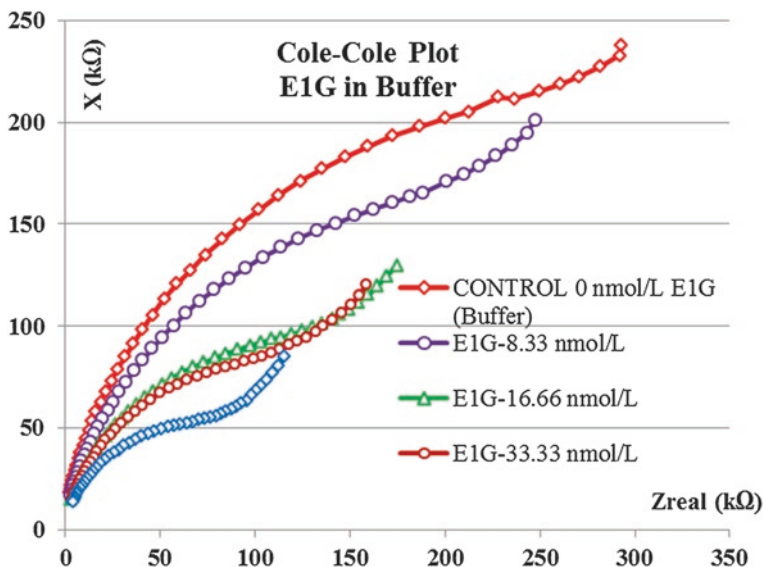


Fig. 4.5 Nyquist (Cole-Cole) plot for the impedance measurements of E1G

the increasing concentration of the analyte, which is responsible for the rise in the double layer capacitance appearing at the electrode-electrolyte interface.

4.2.9 Electrochemical Impedance Spectroscopy Analyses for EIG

The experimental data is used for characterization of surface, layers and concentrations with a detailed insight to the system kinetics. This is achieved by analysing the impedance spectrum on the basis of an equivalent series/parallel circuit commonly consisting of resistances and capacitances representing the different electrochemical and physicochemical properties of the system under analysis [10].

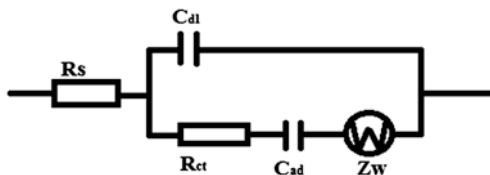
Figure 4.6 shows the equivalent circuit obtained as an interpretation of the experimental findings by using the complex nonlinear least squares curve fitting (CNLS) technique. The experimental impedance spectrum not only interprets the exchange and diffusion processes taking place in the electrochemical cell but it provides a necessary characterization of surface, layers and concentrations when analysed on the basis of Randle's model by CNLS algorithm. It shows uncompensated solution resistance R_s in series with a parallel combination of double layer capacitance C_{dl} to the charge transfer resistance R_{ct} in series with Warburg impedance Z_w [11].

C_{dl} can be calculated from the frequency at the maximum of the semi-circular region in the Nyquist plot using $\omega = 2\pi f = 1/R_{ct}C_{dl}$, whereas, R_{ct} is calculated by extrapolating the semicircle to real impedance axis. Using Randle's cell model, the real and imaginary impedance at the electrode-solution interface could be derived as shown by the Eq. 4.1.

$$Z(\omega) = R_s + \frac{R_{ct}}{1 + \omega^2 R_{ct}^2 C_{dl}^2} - \frac{j\omega R_{ct}^2 C_{dl}}{1 + \omega^2 R_{ct}^2 C_{dl}^2} \quad (4.1)$$

The equivalent circuit was estimated using theoretical calculations by electrochemical spectrum analyser algorithm. The algorithm performs statistical analysis to calculate the residual mean square for experimentally observed values in measured spectra. The results are compared to the calculated values based on the theoretical response of suggested equivalent circuit. The fitted Nyquist plot is shown in Fig. 4.7.

Fig. 4.6 Electrochemical equivalent circuit extracted by CNLS curve fitting



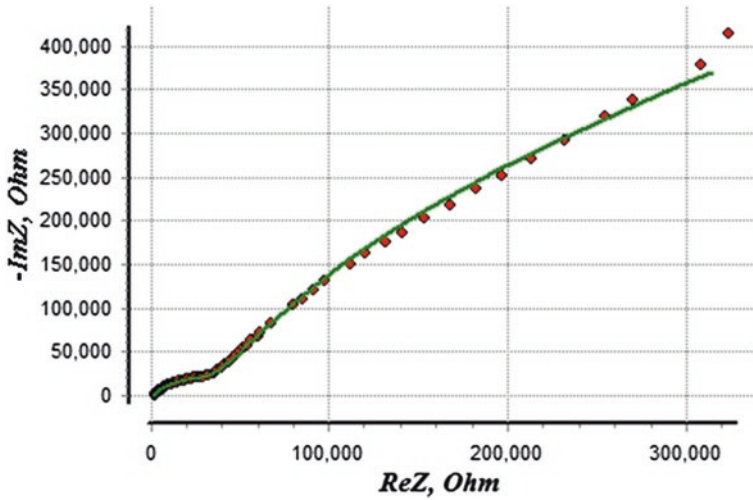


Fig. 4.7 CNLS curve fitting of Nyquist plot by spectrum analyser for the highest concentration of EIG 55.55 nmol/L

The bold line curve displays the modelled behaviour of the equivalent circuit whereas; the markers represent the experimentally observed response from the electrochemical cell. The optimization of the calculated data is achieved by the number of iterations it takes to solve the mathematical model for the proposed equivalent circuit. It took 500 iterations to extract the equivalent component values for the equivalent circuit shown in Fig. 4.6. The table of values at different concentrations of EIG is given in Table 4.1.

It should be noted that CNLS was applied to three concentrations of EIG only.

4.2.10 EIG Sensitivity Analysis

Characterization of each sensor was performed on the basis of Bode and Nyquist plots. The sensitivity of the sensor was calculated by using the real impedance and reactance data using following relations.

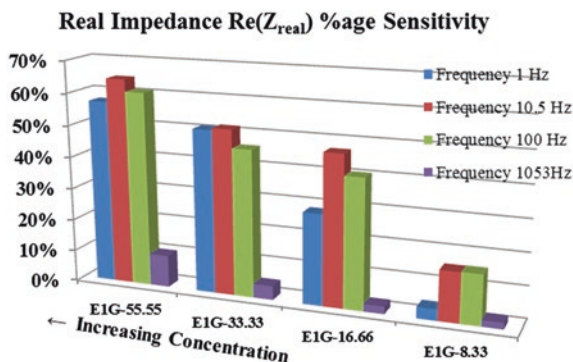
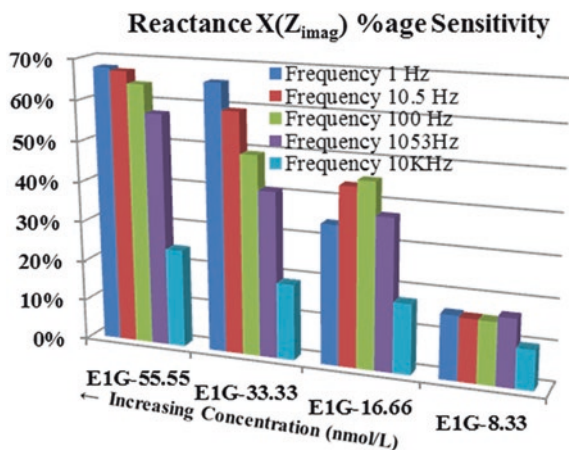
$$Z_{real}Sensitivity = \frac{Z_{real}(control) - Z_{real}(sample)}{Z_{real}(control)} \times 100 \tag{4.2}$$

$$X_{imag}Sensitivity = \frac{X(control) - X(sample)}{X(control)} \times 100 \tag{4.3}$$

The sensitivity was plotted against concentration with reference to the control solution for five chosen values of frequency to observe its effect at minimum and

Table 4.1 Equivalent circuit components' parameters deduced by CNLS curve fitting technique for electrochemical spectrum analysis

Component parameter (unit)	Concentration of E1G solution in buffer		
	8.33 nmol/L	16.66 nmol/L	33.33 nmol/L
C_{ad} (F)	1.825E-07	1.45E-07	1.58E-07
R_s (Ω)	1.14E+02	1.01E+02	0.30E+02
R_{ct} (Ω)	1.7304E05	1.61E+05	1.57E+05
Z_w (Ω)	2.4431E06	1.90E+06	1.79E+06
C_{dl} (F)	6.95E-09	8.69E-09	9.20E-09

Fig. 4.8 %age sensitivity of the real part of impedance (Re)**Fig. 4.9** %age sensitivity of capacitive reactance (X)

maximum values. These values were chosen one frequency per decade with a minimum of 1 Hz through to 10 kHz. The sensitivity plots for reactance and real impedance are shown in Figs. 4.8 and 4.9, respectively. The plots demonstrate that the sensor is fairly sensitive in a frequency range of 10–100 Hz. This is due

to the fact that the sensor owns capacitive properties due to the electrode geometry and the thin film passivation layer of Si_3N_4 ; therefore, its capacitance value is higher during this range as simulated and predicted by Finite Element Modelling as discussed earlier. At higher frequencies, its capacitive response to the periodic perturbation reduces as it behaves as a high-pass filter at those frequencies.

Comparing the sensitivities of Re and X, it is concluded that the imaginary part of impedance (X) provides better sensitivity, in terms of magnitude and incident frequency band, for the detection of the hormone metabolite E1G [12].

4.3 Electrochemical Detection of Progesterone Hormone

4.3.1 Motivation

The poor reproductive performance of dairy cattle is one of the most difficult and expensive problems for dairy and livestock producers. The profitability of the dairy industry is mainly dependent upon the satisfactory reproductive management of the herd. An ideal model followed in dairy farming states that a dairy herd is termed reproductively efficient when it follows a calving interval of 365 days, in a 10 week period 90 % of cows calve and when 5 % or fewer animals are culled due to reproductive failure [13, 14]. Statistics shows that even in well-managed dairy farms in New Zealand, the reproductive failure rate is much higher than 5 %. The main problem faced in this context is the poor detection of estrus. Estrus is a phase in the reproductive cycle of the dairy cow prior to ovulation when it is reproductively receptive ('in heat'). Figure 4.10 shows the progesterone concentration level during 21 days reproductive cycle of dairy cows dictating the estrus window targeted in this research. Extended calving intervals, veterinary costs, milk loss, etc. are the major adverse outcomes of incorrect detection of estrus which causes loss of profit in the dairy business.

Measurements of progesterone concentration in the blood or milk are an accurate indicator of estrus [15–17], but monitoring progesterone level in milk

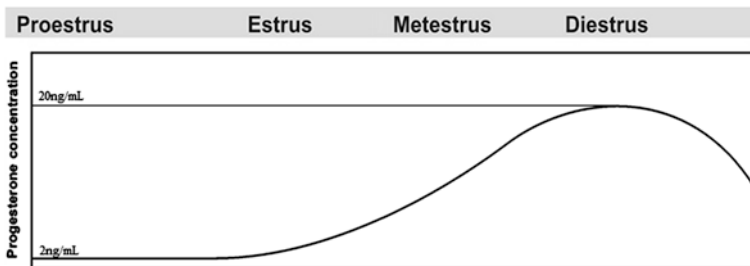


Fig. 4.10 Progesterone concentration level during 21 days reproductive cycle of dairy cows [12]

rather than blood has an advantage of the easy sampling method. The concentration of progesterone in the blood is correlated closely with its concentration in milk. In fact, since progesterone is a steroid hormone, it has an affinity for milk fat: thus progesterone in milk is somewhat in higher concentration than in blood [18]. Elevated progesterone concentrations indicate luteal dominance while low amounts of progesterone are associated with estrus [18].

Methods used presently for estrus detection such as pedometry, teaser bull or observed behavior of cow, are not precise and accurate. Farmers often achieve a heat detection rate of only 35–70 % and up to 20 % of cows presented for insemination are not in heat [19]. Progesterone detection test based on enzyme-linked immunoassays (ELISA) is available as kits on farm use [16], but most of these tests are manual, indicative and designed for qualitative measurement to confirm estrus and determination of pregnancy or non-pregnancy only. These tests are unable to quantify the precise concentration of progesterone in the sample, therefore; can only be used for ‘estrus confirmation’, not for ‘estrus detection’. Various other immunoassay formats have been proposed for progesterone detection in bovine milk such as BIAcore™ biosensor based on surface plasmon resonance (SPR) [20], Heap et al. [21] quantified progesterone concentration using radioimmunoassay (RIA), a rapid enzyme immunoassay (EIA) based on horseradish peroxidase was developed by Claycomb et al. [22], a competitive immunochromatographic assay of milk progesterone was developed by Laitinen and Vuento [23] and Total internal reflection fluorescence-based detection of milk progesterone [24]. All these methods are expensive, time-consuming, require highly skilled personnel and need laboratory environment to perform. Moreover, livestock producers are not much benefited from these techniques as the farmers have to invest extra effort, resources and time in order to get access to these methods. Above all, these techniques cannot be used for continuous monitoring of milk progesterone in bovine milk for estrus detection.

According to Senger [13] an ideal system for detection of estrus in dairy animal should: (i) have continuous surveillance characteristics; (ii) automatically detect estrus; (iii) operative during whole productive lifetime of a cow; (iv) have minimal labor requirements; (v) be highly accurate and efficient (95 %). Unfortunately, there is no such detection system available at the farm level, which may scientifically detect and inform the farm manager, the right time for artificial insemination (AI), for the better reproductive efficiency of the dairy animals. Farmers, to-date, have to rely on centuries old methods for this important parameter of their industry. This inadequacy had provided the necessary motivation to apply the fabricated interdigital capacitive sensor and impedance spectroscopy technique for real-time measurement of progesterone in aqueous media to mimic bovine milk whey, which is usually used for such kind of detection and quantification. Another objective of this research was to develop a rapid real-time assay technique by applying impedance spectroscopy based novel interdigital sensor technology and to model and evaluate the performance of the proposed system.

Table 4.2 Progesterone in deionized water-samples' nomenclature and concentration

Sample name	Progesterone concentration (ng/mL)
Sample-B	0.02
Sample-C	2
Sample-D	20
Sample-E	200

4.3.2 Materials and Methods for Progesterone Detection

Research grade progesterone hormone was procured from Sigma-Aldrich, GmbH, Germany for testing. The hormone is not water soluble. Therefore, 20 mg of progesterone was dissolved in 0.5 ml of 99.6 % Ethanol, and the solution was poured in 999.5 ml of purified Milli-Q water to make the stock solution. The concentration of progesterone in stock solution is 20 $\mu\text{g/ml}$. Using series dilution method 200, 20, 2 and 0.02 ng/ml concentration of progesterone was achieved in successive steps. The samples were tested immediately after preparation in the laboratory environment at 47 % humidity and 23 °C temperature. The samples were kept refrigerated at 4 °C for further testing. A control solution was prepared with 999.5 ml MilliQ and 0.5 ml 99.6 % ethanol for calibration of sensors and to obtain a reference for sensitivity calculations. The sensing part of the sensor was immersed in the 2 ml of control solution to create a control reference for the measurement. EIS experiments were carried out using Hioki 3522-50 LCR Hi precision Tester (Japan). All experiments were performed using slow mode of the testing equipment as to keep error rate less than 0.05 % as specified by the manufacturer in the specification. A constant voltage sinusoidal signal of 1V_{rms} was applied to the sensor with a frequency sweep of 10 Hz to 200 kHz with 20 data points per decade on the log scale. Experiments were conducted to analyse the performance of 1-11-50 parylene coated sensor at different concentration levels of progesterone in deionized water. The concentration levels tested for detection of progesterone in MilliQ water are given in Table 4.2 and results for sample-B, sample-C and sample-D are plotted as bode and Nyquist plots. Sample-C and sample-D were chosen due to the target range of progesterone concentration in bovine milk whereas; sample-B was tested to figure out the limit of detection (LOD) for progesterone. In order to ensure removal of any residual hormone from the sensing surface, it was cleaned with ethanol and dried under nitrogen flow before the next run. Therefore, to make sure that the sensor has attained its initial conditions, the sensor was a profile in the air. Each test was run three times and average of three sets was taken for all applied frequencies.

4.3.3 Electrochemical Impedance Analyses for Progesterone

Characterization of each sample was performed on the basis of Bode and Nyquist plots. The plot of real and imaginary impedance versus frequency for 1-11-50

sensor in Fig. 4.11 showed the relative change in impedance varying with different concentration levels of progesterone. This change was prominent at lower frequencies as compared to the higher frequency range.

With increasing concentration of progesterone the imaginary impedance decreases which could be attributed to the conductance of the progesterone molecule in the solution. This dictates the capacitive behaviour of the sensor at low frequencies. The real part of the impedance which is the dissipative part changes in a considerable amount providing a direct relationship between the conductivity of the medium to the increasing concentration levels of progesterone in the solution.

Figure 4.12 shows the Bode Plot impedance spectra. It was observed that the change in absolute impedance occurred, even, for 0.02 ng/ml concentration and is read by the sensor. It provided a close agreement to the Bode plot for a system where electrode polarization is due to kinetic processes taking place at the electrodes' surface. This can be validated by modelling an equivalent circuit. The measured impedance value applied to the equivalent circuit can generate a fitting impedance spectrum to match the experimental observations.

Figure 4.13 shows Nyquist plot for the electrochemical impedance spectra of the sensor at different concentration levels of progesterone hormone samples. The plot depicts that a 45° line starts appearing with the plots as soon as the concentration of hormone increases in the solution. This line represents the presence of ionic concentration with the increasing concentration of the hormone in the sample. The decrease in reactance with increasing concentration of progesterone is due to the dielectric properties of the hormone. Therefore, it could be concluded that the concentration could be correlated with reactance or conductance of the progesterone hormone. However, reactance is the more dominating part of impedance change.

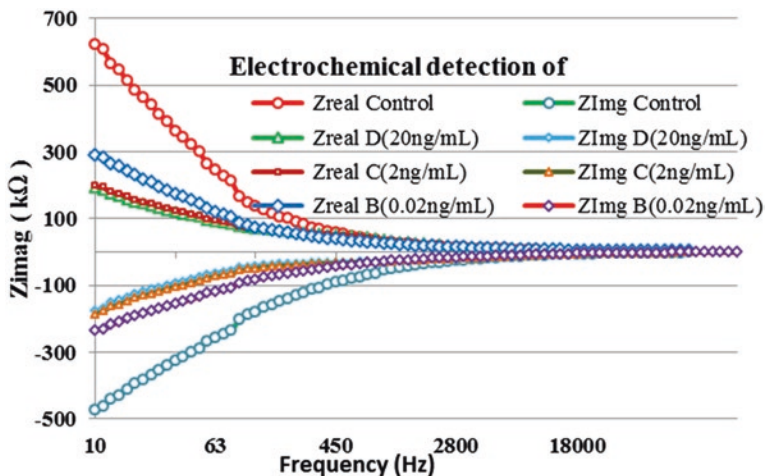


Fig. 4.11 Real and imaginary impedance (reactance) characteristics

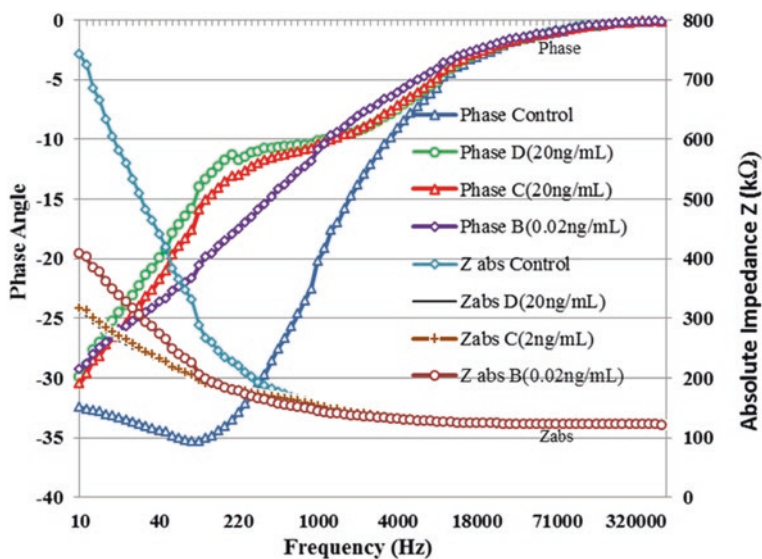


Fig. 4.12 Bode plot for progesterone detection in deionized water

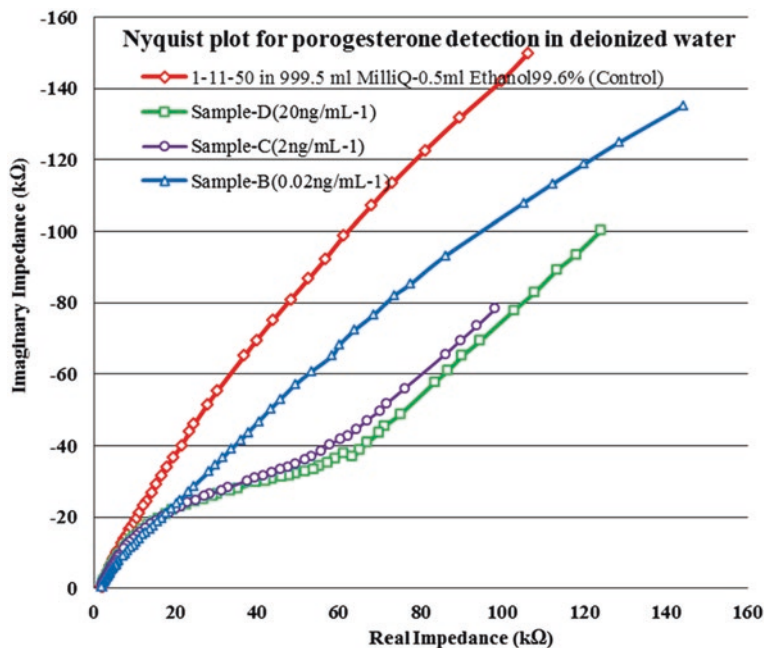


Fig. 4.13 Nyquist plot for progesterone detection in DI water

It is noticed from Fig. 4.13 that each of three impedance spectra includes a semicircle and a linear line portion at an angle of 45° . The diameter of the semicircle represents the electron transfer resistance at the surface of the electrodes whereas; the linear portion corresponds to a diffusion process leading to Warburg resistance at the electrode-solution interface. It was observed that the sensor can distinctively distinguish between concentrations of progesterone especially at low frequencies. This feature defines the sensitivity of the sensor for progesterone concentration in the solution as observed in Fig. 4.14. The sensitivity curves (Figs. 4.14 and 4.15) were plotted using Eqs. 4.2 and 4.3 respectively which calculated the sensitivity values with reference to the control solution. The results

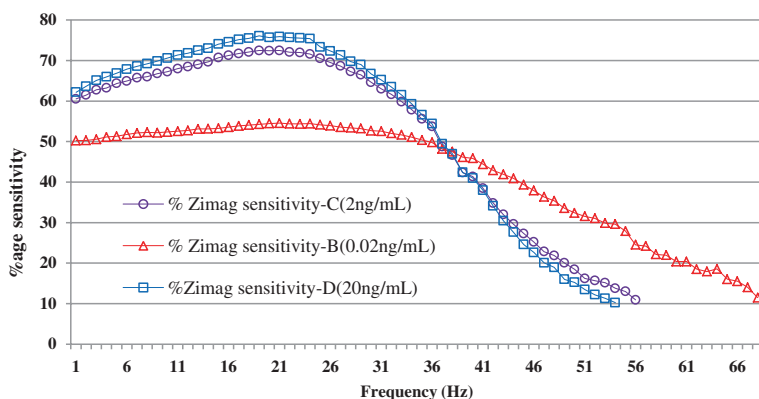


Fig. 4.14 $Z_{\text{imag}}(X)$ % sensitivity

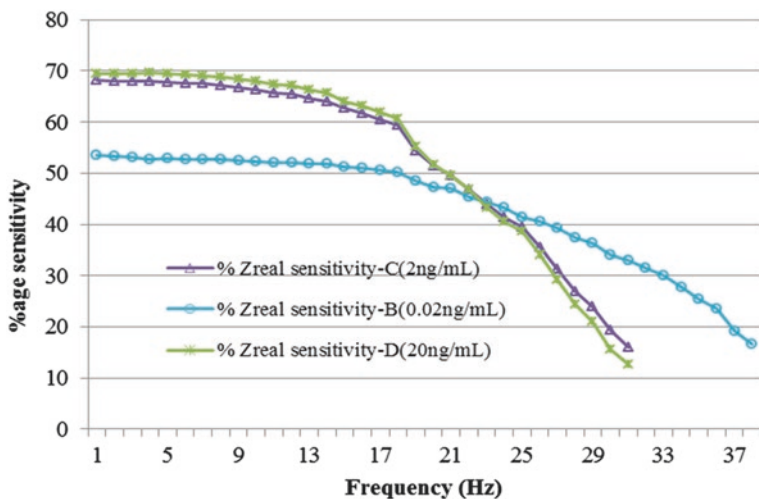


Fig. 4.15 $Z_{\text{real}}(R_s)$ % sensitivity

display that the reactance percentage sensitivity stays till considerable range of frequency whereas conductance percentage sensitivity approaches lower values in the smaller part of the incident spectrum.

In view to the response of the sensor at low frequencies, the sensitivity of the sensor was plotted in a frequency range of 1–50 Hz to figure out the most sensitive frequency value. The sensor displayed the sensitivity value well above 50 % to the progesterone concentration as low as 0.02 ng/ml in the deionized water [25].

4.4 Conclusions

The response of the proposed sensing system was analysed for progesterone hormone and hormone metabolite E1G. The analyses depicted that the sensing system had enough potential to detect the presence of analytes in the deionized aqueous medium. The sensitivity analyses for both types of molecules proclaimed the capability of the sensor and sensing system to differentiate between different concentrations of the analytes. It should be noted that the tested analyte concentrations were just trace level and detecting such minute quantities was quite promising for further research and developments in the project. In the next phase of this research endeavour, couple of endocrine disrupting compound were tested for rapid detection using the developed sensing system and electrochemical analyses were carried out to deduce meaningful information.

References

1. M.E. Allende, Mean versus individual hormonal profiles in the menstrual cycle. *Fertil. Steril.* **78**(1), 90–95 (2002)
2. L.F. Blackwell, J.B. Brown, D. Cooke, Definition of the potentially fertile period from urinary steroid excretion rates. Part II. A threshold value for pregnanediol glucuronide as a marker for the end of the potentially fertile period in the human menstrual cycle. *Steroids* **63**(1), 5–13 (1998)
3. W.H. Organization, Temporal relationships between indices of the fertile period. *Fertil. Steril.* **39**(5), 647–654 (1983)
4. W.P. Collins, The evolution of reference methods to monitor ovulation. *Am. J. Obstet. Gynecol.* **165**(6 Pt 2), 1994–1996 (1991)
5. G. Freundl, I. Sivin, I. Batár, State-of-the-art of non-hormonal methods of contraception: IV. Natural family planning. *Eur. J. Contracept. Reproduct. Health Care* **15**(2), 113–123 (2010)
6. M.C. Weissmann, L. Foliaki, E. Billings et al., A trial of the ovulation method of family planning in Tonga. *The Lancet* **300**(7781), 813–816 (1972)
7. J. Brown, L. Blackwell, J. Holmes et al., New assays for identifying the fertile period. *Suppl. Int. J. Gynecol. Obstet.* **1**, 111 (1989)
8. J.B. Brown, J. Holmes, G. Barker, Use of the home ovarian monitor in pregnancy avoidance. *Am. J. Obstet. Gynecol.* **165**(6 Pt 2), 2008–2011 (1991)
9. L.F. Blackwell, J.B. Brown, P. Vigil et al., Hormonal monitoring of ovarian activity using the Ovarian Monitor, Part I. Validation of home and laboratory results obtained during ovulatory cycles by comparison with radioimmunoassay. *Steroids* **68**(5), 465–476 (2003)

10. F. Lisdat, D. Schäfer, The use of electrochemical impedance spectroscopy for biosensing. *Anal. Bioanal. Chem.* **391**(5), 1555–1567 (2008)
11. M.I. Prodromidis, Impedimetric immunosensors—a review. *Electrochim. Acta* **55**(14), 4227–4233 (2010)
12. A. Zia, S.C. Mukhopadhyay, P.L. Yu, I.H. Al Bahadly, *Ovarian Hormone Estrone Glucuronide (E1G) Quantification-Impedimetric Electrochemical Spectroscopy Approach*, pp. 22–27
13. P. Senger, The estrus detection problem: new concepts, technologies, and possibilities. *J. Dairy Sci.* **77**(9), 2745–2753 (1994)
14. E. Strandberg, P.A. Oltenacu, Economic consequences of different calving intervals. *Acta Agriculturae Scandinavica* **39**(4), 407–420 (1989)
15. J. Laing, R. Heap, The concentration of progesterone in the milk of cows during the reproductive cycle. *Br. Vet. J.* **127**(8), xix–xxii (1971)
16. R. Nebel, On-farm milk progesterone tests. *J. Dairy Sci.* **71**(6), 1682–1690 (1988)
17. G. Otava, C. Mircu, H. Cernescu et al., Comparative relations between progesterone blood concentration and appearance of oestrus in cows. *Vet. glas.* **61**(1–2), 37–42 (2007)
18. R. Koelsch, D. Aneshansley, W. Butler, Milk progesterone sensor for application with dairy cattle. *J. Agric. Eng. Res.* **58**(2), 115–120 (1994)
19. M.G. Diskin, J.M. Sreenan, Expression and detection of oestrus in cattle. *Reprod. Nutr. Dev.* **40**, 481–491 (2000)
20. Y. Wu, J. Mitchell, C. Cook et al., Evaluation of progesterone-ovalbumin conjugates with different length linkers in enzyme-linked immunosorbant assay and surface plasmon resonance-based immunoassay. *Steroids* **67**(7), 565–572 (2002)
21. R.J. Heap, J.E. Gadsby, J.A. Laing et al., Pregnancy diagnosis in the cow from milk progesterone concentration. *Br. Vet. J.* **132**(5), 445–464 (1976)
22. R.W. Claycomb, M.J. Delwiche, C.J. Munro et al., Rapid enzyme immunoassay for measurement of bovine progesterone. *Biosens. Bioelectron.* **13**(11), 1165–1171 (1998)
23. M. Laitinen, M. Vuento, Affinity immunosensor for milk progesterone: identification of critical parameters. *Biosens. Bioelectron.* **11**(12), 1207–1214 (1996)
24. N.D. Käppel, F. Pröll, G. Gauglitz, Development of a TIRF-based biosensor for sensitive detection of progesterone in bovine milk. *Biosens. Bioelectron.* **22**(9), 2295–2300 (2007)
25. A.I. Zia, A. Mohd Syaifudin, S. Mukhopadhyay et al., *Sensor and Instrumentation for Progesterone Detection*, pp. 1220–1225

Chapter 5

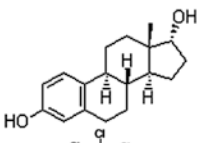
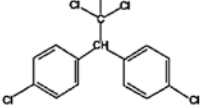
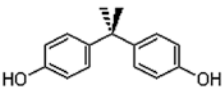
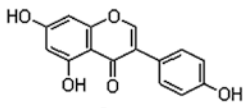
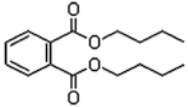
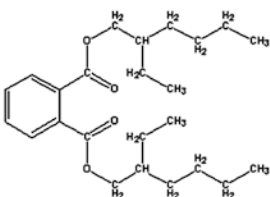
Electrochemical Detection of Endocrine Disrupting Compounds

5.1 Introduction

Endocrine disrupting compounds are exogenous chemicals or mixture of chemicals that interfere the normal functioning of the endocrine system and cause hormonal imbalances in living organisms. These hormonal imbalances can cause cancers, birth defects, developmental disorders, nutritional malfunctions and impotency, especially in males. EDC can block the receptor cells by stopping them to respond or can cause an adverse response by getting attached to the receptor in place of a hormone cell. Table 5.1 shows molecular structures of the most ubiquitous endocrine disruptors on earth.

Phthalates, chemically known as 1-2-Benzenedicarboxylic acid esters, are internationally recognized as key industrial chemicals with a large number of commercial uses, such as additives, solvents, and plasticizers due to their low cost [1]. Phthalates with higher molecular weight i.e. DINP (Diisononyl phthalate) and DEHP constitute about 80 % of the phthalate production for the reason of their use as plasticizer in almost every plastic product including food and beverage packaging and medical applications, while low molecular weight phthalates, such as diethyl phthalate (DEP) and dimethyl phthalate (DMP), are used in cosmetics, insecticides, paints and pharmaceutical applications [2]. Phthalates added as plasticizers; do not covalently bond to the molecular structure of the resulting product. Therefore, their potential for non-occupational exposure to the environment is high. They leach and migrate into packed food and beverages, gas out in the atmosphere or enter directly into human body fluids through medical products [3]. Human exposure to phthalates is a major concern for adverse human health risk. Phthalates have been characterized as environmental endocrine-disrupting compounds (EDCs) by many health monitoring agencies in the world due to their observed reproductive and developmental defects in rodents [4]. It was concluded that DEHP poses highest toxicity threat to the human race, especially to children under 12 months of age and pregnant and nursing mothers [1]. A number of recent researchers have suggested declining trend in the reproductive hormones levels in male adults [5] and elevated risk of breast cancer in females [6].

Table 5.1 List of the most ubiquitous EDCs

Compound	Structure	Description
Estradiol		Endogenous Estrogen
DDT		Pesticide
BPA		Plastics Component
GEN		Phytoestrogen
DBP		Phthalate
DEHP		Phthalate

Human beings come in contact with phthalates in environmentally by three major routes; Dermal, Inhalation, and oral (dietary) intake [7]. The oral route is the most important among all as it contributes the highest phthalate exposure rates to the human beings. Dietary exposures occur by accumulating phthalates either during the food processing and packaging from processing equipment or leaching into fatty foods, including dairy products and from packaging during storage. Dairy products consumption by children per kilogram body weight is higher as compared to the adults, posing a greater risk of reproductive and developmental toxicities for young children [7]. Polymer toys softened with DINP were estimated exposures ranged from 5–44 $\mu\text{g}/\text{kg}$ body weight/day with 99th percentiles up to 183 $\mu\text{g}/\text{kg}$ body weight/day for infants via mouthing activities [8]. Due to the leachability several researchers reported migration of phthalates from food packaging [8], PET (PETE, polyethylene terephthalate) bottled beverages and mineral water [9] and from glass bottles corks [10]. World Health Organization (WHO) and the European Union have limited DEHP in their water policy by setting the guideline value at 8.0 $\mu\text{g}/\text{L}$ in fresh and drinking waters in a published list of

Table 5.2 Risk assessment of phthalates by world agencies [3]

Phthalate type	Risk assessment of phthalates			
	Country, region	Committee/year	mg/kg body weight/day	MRL ^a /TDI ^b /RfD ^c
DEHP	USA	US-EPA, 1993b	0.02	RfD
DEHP	USA	ATSDR, 2002	0.1	MRL
DEHP	Canada	Health Canada, 1994	0.044	TDI
DEHP	EU	CSTEE, 1998a, b	0.050	TDI
DINP	EU	CSTEE, 1998a, b	0.25	TDI
DEP	USA	ATSDR, 1995	7	MRL
DBP	USA	ATSDR, 2001	0.5	MRL
DBP	USA	US-EPA, 1990	0.1	RfD

^a minimal risk level; ^b tolerable daily intake; ^c reference dose levels

priority compounds posing endocrine disrupting hazard to human [11]. Table 5.2 shows risk assessment of phthalates by agencies in EU, US, and Canada.

5.2 Impedimetric Detection of DEHP and DINP

In May 2011, Ministry of Health Taiwan reported the illegitimate addition of phthalates by a drink manufacturing company into its products to make the juice look cloudy [12]. DEHP was added as a clouding agent in the drink. Later, on investigations, phthalates were found in certain medicines, foods and beverages manufactured in Taiwan. DEHP has legitimately been used as plasticizers in PVC food contact packaging material, but its use as a food additive has never been allowed due to its health risk. It should be noted that the Tolerable Daily Intake (TDI) limit for DEHP in Taiwan and Hong Kong is 1.5 ppm [13]. Long-time ingestion of DEHP with food at levels above the TDI can create a hormonal imbalance in the human body that may result in the decrease of male reproductive ability, and female precocious puberty, breast cancer and loss of gender uniqueness [6, 14–16]. This incident created a huge wave of suspicion for all packed beverages throughout the world. Importers demanded testing certifications from the manufacturing companies which caused huge workload on the test laboratories. Due to expensive and time-consuming testing, manufacturers had to face production loss and paid additional costs.

Phthalates' detection and measurement are purely a laboratory-based procedure. The ubiquitous presence of this compound as a contaminant seriously limits its minimal detection level. Even in most controlled laboratory setup, it cannot generally be accurately quantified below about 2 ppb [17]. Gas chromatography (GC) is the most commonly used technique for detection and quantification of phthalates metabolites [18]. High-performance liquid Chromatography (HPLC) is used to measure phthalate concentrations in blood plasma and urine sample at low

detection limits [19, 20]. Chromatography technique is used to separate complex mixtures of organic compounds with each compound quantified by its individual detector. DEHP is measured using Electron Capture Detector (ECD) [18] and Flame Ionization Detector (FID) [21]. Liquid Chromatography (LC) coupled with mass spectrometry (MS) and ultraviolet (UV) detection are also a few commonly used techniques for detection of phthalates.

5.2.1 Motivation

Almost all contemporary analytical techniques used to detect phthalates in food products and beverages require laboratory environment with stringent conditions oversampling procedures. There is a paramount requirement for a low-cost real-time testing system which could be used for instant screening of food and beverage products to detect the presence of phthalates that could readily be installed in an automated setup. The discussed design and methodology of the developed sensing technique possesses properties of speed, in situ testing with an additional benefit of low cost. The objective of this part of the research was to test the detection response of the fabricated sensor for the two phthalate esters; di(2-ethylhexyl) phthalate (DEHP) and diisononyl phthalate (DINP). The molecular structures of DEHP and DINP are shown in Figs. 5.1 and 5.2 respectively.

Fig. 5.1 Molecular structure DEHP

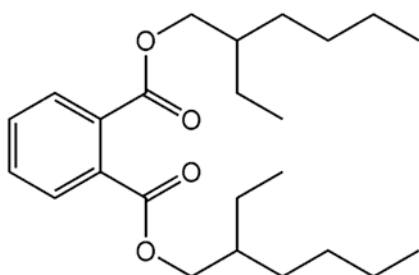
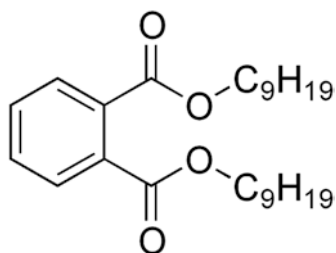


Fig. 5.2 Molecular structure DINP



5.2.2 Materials and Methods

Gravimetrically prepared 99.5 % pure solutions of DEHP and DINP at a concentration of 100 $\mu\text{g/mL}$ (100 ppm) in ethanol were procured from ChemService® USA. Two set of working solutions of these compounds were prepared by serial dilution method. The first set was prepared with deionized water MilliQ® (MILLIPORE USA) at a concentration of 0.002–2 ppm concentration levels of DEHP. The second round of samples was prepared at a concentration level of 0.1, 0.5, 1 and 20 ppm of DINP in ethanol. 20 ppm concentration from this set was used as stock solution. 99.7 % pure research grade ethanol was used to dilute serially the stock to achieve lower concentrations. pH of control and working solutions were tested using IQ Scientific Instrument Inc. USA, after calibration with the buffer solutions provided by the manufacturer.

Hioki 3522-50 LCR Hi precision Tester (Japan) was used for the EIS experiments. The equipment was interfaced with a desktop computer through RS-232C hardware interface device. Automatic data acquisition software programmed in Lab view® was used to generate Microsoft excel® data file in real time. The LCR tester was calibrated with built-in open circuit and short circuit tests in order to offset any stray capacitance appearing due to the testing leads. Figure 5.3 shows the test bench setup and Fig. 5.4 shows bulk sample testing using the dip-test method.

All experiments were performed using slow mode of testing to achieve an error rate of <0.05 %. For reliable results, the device was set to write an average of 8 readings of impedance values at each single frequency applied to the sensor. A $1V_{\text{rms}}$ sinusoidal signal was applied to the sensor with a frequency sweep of 10 Hz to 100 kHz with 20 data points per decade on a log scale. An average of three experiments was used to ensure further reproducibility and reliability of the results. The sensor was cleaned with acetone, rinsed with deionized water and dried in nitrogen in before next test.

Fig. 5.3 Test bench setup

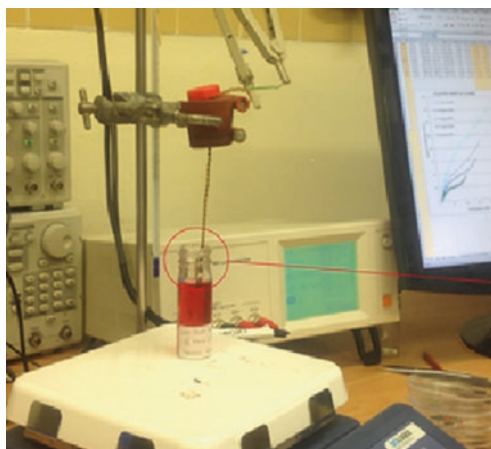


Fig. 5.4 Dip-test (bulk)

5.2.3 DEHP Detection Test in Deionized Water

Deionized Milli-Q water (18 M Ω cm) with 2 ppm ethanol (99.7 % purity) was used as a control solution. The pH of the control was 7.3 at 23 °C in the laboratory environment. 2 ppm concentration of DEHP was used as a stock solution to obtain the lower concentrations of 0.2, 0.02, and 0.002 ppm by serial dilution of the stock solution. This range of the DEHP concentration in the test samples was chosen to check the response of the sensing system for the trace level detection of DEHP. The pH of the stock solution was measured to be 6.95 at 23 °C. Experiments were conducted immediately after sample preparation at 23 °C with a humidity level of 47 % in a laboratory environment. Figure 5.5 shows the plot of imaginary and real part of impedance vs. frequency for all the four concentrations of DEHP.

The capacitive reactance (Z_{imag}) showed a good variation with changing concentrations of DEHP especially at a lower frequency range (10–400 Hz). At higher frequencies (500 Hz–5 kHz) the rate of change in impedance was observed to be extremely low. This change is described in terms of sensitivity in the analysis discussed in later part of this chapter. The corresponding change in Z_{real} was not dominant, and its rate of change was much less in comparison to its counterpart; capacitive reactance (Z_{imag}). This showed the increase in capacitance of the sensor with an increase in DEHP concentration which was due to the inherent dielectric properties of the DEHP target molecule. The real part represented the static resistance of the solution appearing due to the ionic currents passing through the electrochemical cell. The coated polymer stopped the ion exchange through the electrode surface. The Nyquist plot shown in Fig. 5.6 demonstrates; a mass transfer process in the form of a straight line at 45° which corresponded to the Warburg resistance and a charge transfer process displayed as a semi-circular region of different diameters. Each semi-circle corresponded to the DEHP concentrations in test solutions.

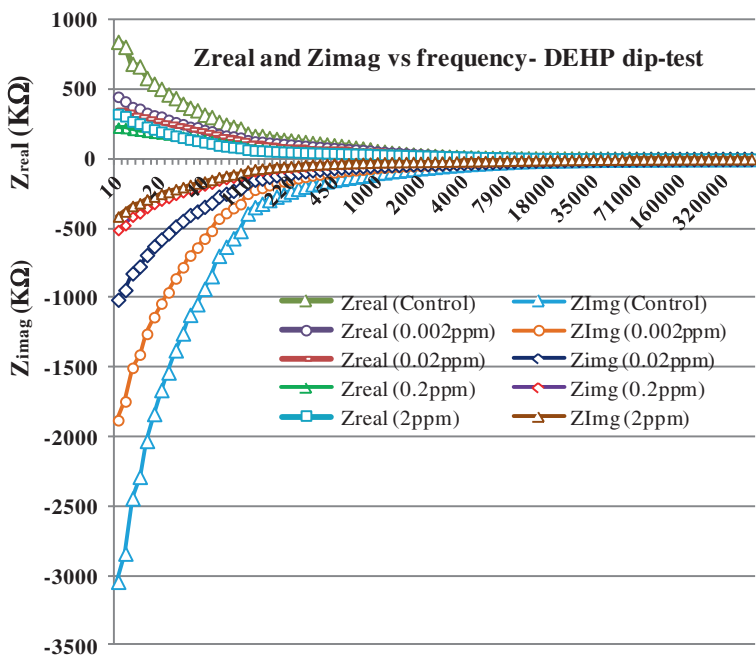


Fig. 5.5 Imaginary and real parts of impedance measurements for DEHP dip-test

The diameter of the semicircle dictated the value of the charge transfer resistance R_{ct} . Correspondingly, R_{ct} changes the double layer capacitance C_{dl} , at the electrode-solution interface which showed the ability of the sensor to monitor the variation of DEHP as low as 0.002 ppm in the deionized water.

5.2.4 Experimental Data Analyses by CNLS Curve Fitting

The equivalent circuit was estimated using theoretical calculations by electrochemical spectrum analyzer algorithm. The circuit parameters were estimated by a non-linear least square fitting technique which fits the measured impedance data on theoretically estimated values. The algorithm performs statistical analysis to calculate the residual mean square $r_{amplitude}^2$ for experimentally observed values in measured spectra against the calculated values based on the theoretical response of suggested equivalent circuit. $r_{amplitude}^2$ determines the deviation of the experimentally observed data from the optimal solution. The optimization of the calculated data is achieved by the number of iterations it takes to solve the mathematical model for the proposed equivalent circuit. The value of $r_{amplitude}^2$ in the range of 10^{-4} shows optimal fitting with an error rate of less than 5% in calculating the

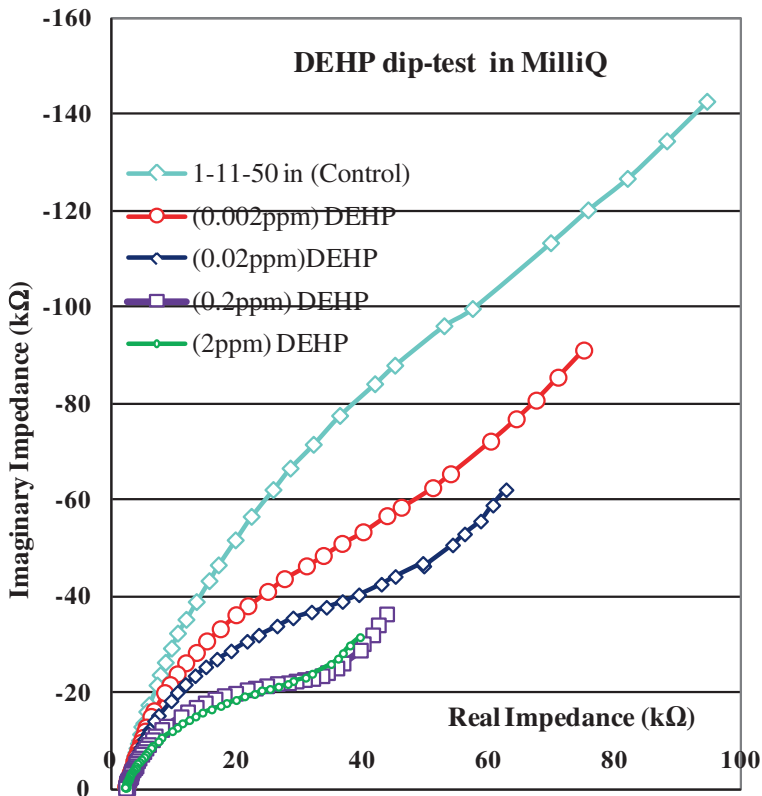
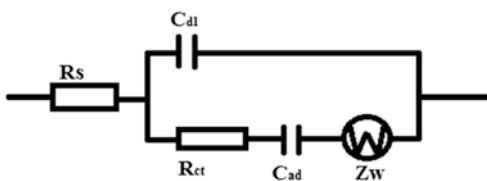


Fig. 5.6 Nyquist plot for detection of DEHP in DI water

Fig. 5.7 Equivalent circuit proposed by CNLS curve fitting



values of equivalent circuit components. Figure 5.7 shows the equivalent circuit interpreting the kinetics of the electrochemical model obtained in consequence of non-linear least square fitting. Figure 5.8 depicts the fitting plot for absolute value of Z . Figure 5.9 shows curve fitting for Nyquist plot and Fig. 5.10 displays the curve fitting for the phase shift. It should be noted that the solid line in all curve fitting plots sketches the theoretically calculated values and the markers display the plot of the experimentally observed values respectively [22].

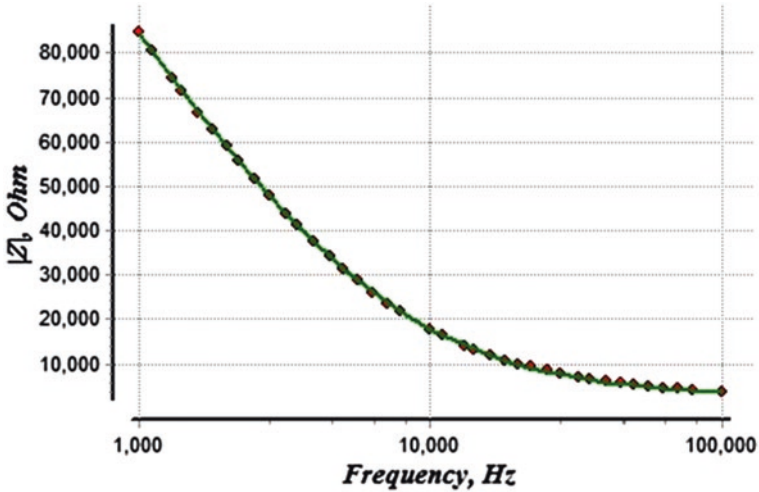


Fig. 5.8 CNLS curve fitting plot for absolute value of impedance

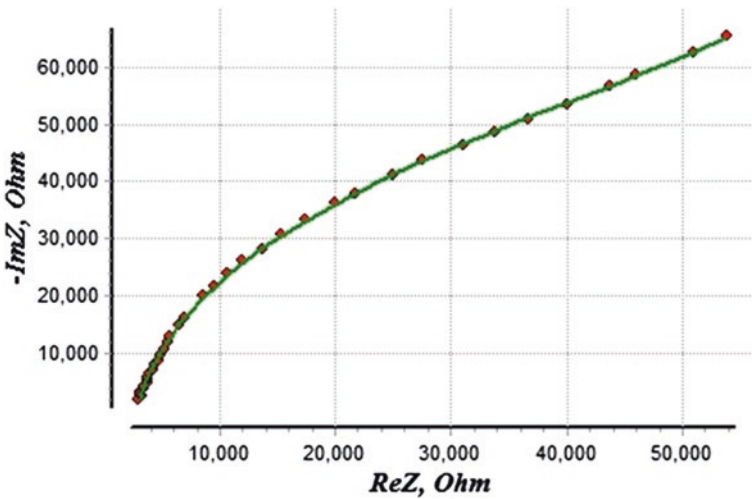


Fig. 5.9 CNLS curve fitting plot for imaginary value of impedance

Table 5.3 represents the equivalent circuit components' parameters, error %ages, and residual mean square values obtained from non-linear least square fitting for DEHP concentrations from 0.002 to 2 ppm in 1–100 kHz frequency range.

The analysis showed that the double layer capacitance C_{dl} increased from 1.5 to 10 pF with increasing concentration of DEHP, which verified the inherent

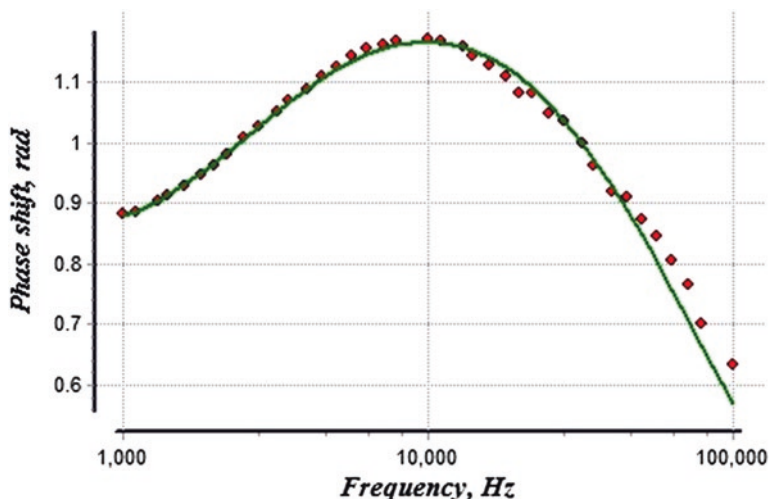


Fig. 5.10 CNLS curve fitting plot for phase shift (θ)

Table 5.3 Equivalent circuit parameters evaluated by CNLS algorithm

Eq. Circuit Para.	Units	DEHP concentrations in deionized water							
		0.002 ppm DEHP		0.02 ppm DEHP		0.2 ppm DEHP		2 ppm DEHP	
		Value	Error (%)	Value	Error (%)	Value	Error (%)	Value	Error (%)
C_{dl}	F	1.5E-9	0.322	1.7E-9	0.93	2.31E-9	0.425	1.01E-8	0.5
C_{ad}	F	5.8E-9	2.72	1.32E-8	4.05	1.29E-8	2.452	1.14E-8	4.03
R_{ct}	Ω	911	0.57	6458	1.29	42,339	0.416	48,805	0.68
Z_w	Ω	2.1E+6	1.61	1.70E+6	3.41	5.13E+5	2.60	2.9E+5	4.47
R_s	Ω	288.9	2.826	2845	4.47	2681.6	1.98	2021.1	3.10
$r_{amplitude}^2$		0.00075375		0.0009797		0.0003502		0.0002925	
Iterations		300		300		300		300	

dielectric properties of DEHP molecule present in the sample solutions. The charge transfer resistance R_{ct} decreased from 91.1 to 48.8 k Ω . Same kind of decrease is observed in Warburg impedance Z_w that reduced from 2.1 to 0.29 M Ω with increasing molecular density of DEHP in the sample solutions. The solution resistance R_s value, which depends on the ionic concentration in the sample solution, also fell from 2.8 to 2 k Ω indicating an increase in conductivity of the sample solutions with increasing concentration of DEHP. Another parameter C_{ad} was observed to build up with increasing concentration of DEHP in samples from 5.8 to 11.4 nF, which is attributed to the formation of adsorbed layer of DEHP on the gold electrode surface. It is caused by the diffusion of ions from the electrode

surface into the solution as a result of the transfer of charges (electrons) into the electrode from the bulk solution [23].

5.2.5 Sensitivity Analysis—DEHP

The sensitivity of the sensor was evaluated on the basis of capacitive reactance which is dominant over the change in the real part of the measured impedance spectra. The real part was unable to provide useful information on impedance change induced by DEHP concentration. This occurred due to the fact that DEHP is a dielectric material, therefore did not contain any ionic concentration in the test samples.

The calculated values of sensitivity (%) plotted in Fig. 5.11 Reactance percentage sensitivity for DEHP in DI water.

The plot depicted that the sensor remains sensitive to the DEHP concentration in MilliQ during a decent range of frequency i.e. 10–1400 Hz. Figure 5.11 accounts for the calculated percentage sensitivity values using sensitivity relationship discussed in the previous chapter plotted against different concentrations of DEHP in the test solutions at 200, 790, 1400 and 5000 Hz frequencies. It is

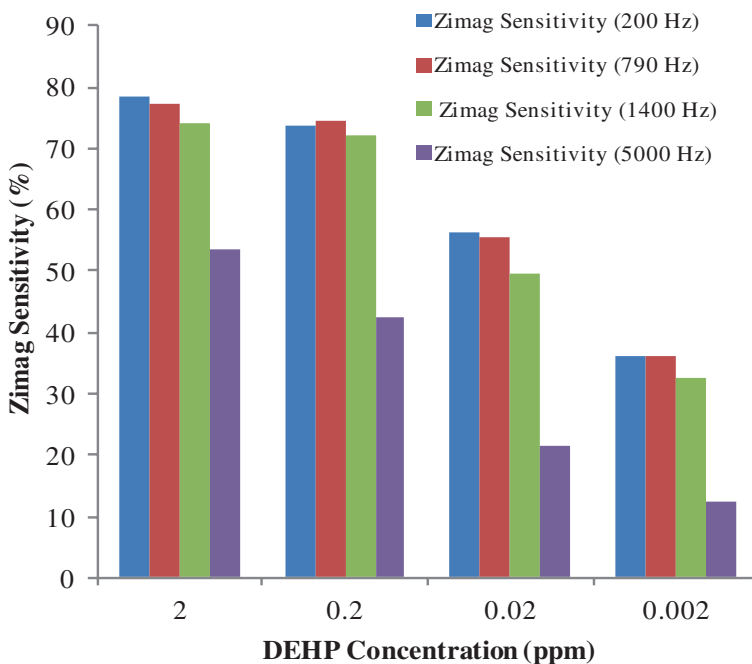


Fig. 5.11 Reactance percentage sensitivity for DEHP in DI water

obvious from the plot that the sensitivity deteriorates drastically after 5 kHz due to the sensor properties. The sensor's size and pitch plays a major role for dictating the sensitivity window for the sensor.

5.2.6 DEHP Detection in Commercially Sold Energy Drink

Due to the strict control by Ministry of Health in New Zealand, it was assumed that the beverages available in the local New Zealand markets are phthalate free. The sensor's response was tested with added DEHP in one of the locally available energy drink, branded "Lift Plus Extra". This drink is supplied in glass bottle packaging. PET bottled drink was not selected for test due to the uncertainty of leached phthalate in the drink. Figure 5.12 shows the test bench used to verify DEHP-spiked energy drinks.

Three spiked working solutions with 2, 6 and 10 ppm concentrations of DEHP were prepared at 23 °C temperature and were tested immediately after sample preparation. These concentration levels were selected to note the detection response of the sensor below and above the MRL limit set by ATSDR, USA. The un-spiked original drink was used as the reference control solution for comparison [24].

The sensor displays change of impedance in the capacitive reactance dominating the corresponding real impedance (Z_{real}) change through a frequency range of 10 Hz to 1.3 kHz. Figure 5.13 shows the plot for real and imaginary part of impedance spectra for the energy drink spiked with DEHP as compared to the un-spiked



Fig. 5.12 Test bench setup for DEHP-spiked energy drinks

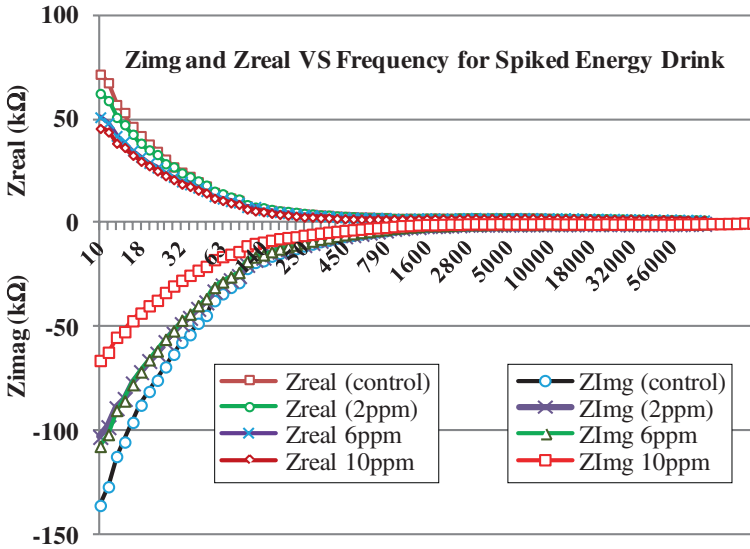


Fig. 5.13 Z_{real} and Z_{imag} for DEHP dip-test of spiked energy drink

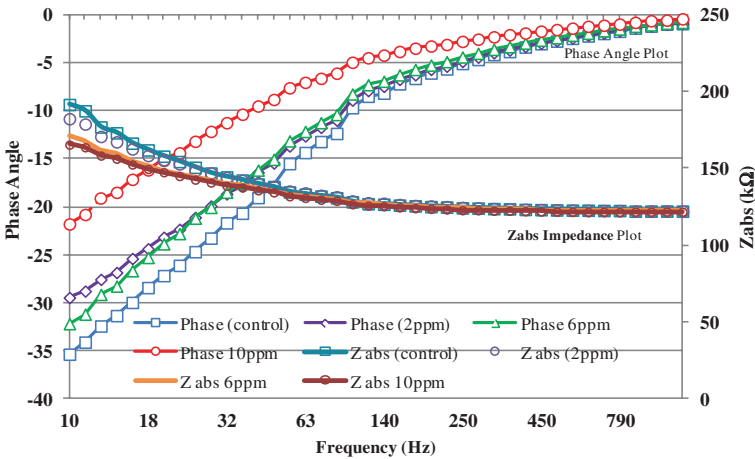


Fig. 5.14 Bode plot showing measured spectra for the spiked drink

drink. Figure 5.14 displays the bode plot for DEHP spiked drink in the said frequency range.

It has been observed that the change in the absolute Impedance Z_{abs} is visible only at the lower frequency range, whereas, the phase shift is distinctive for pure and spiked samples, especially for DEHP concentration as high as 10 ppm. The magnitude of change in imaginary impedance for 2 and 6 ppm of spiked energy

drink did not show much difference due to the fact that energy drink contains many other chemicals apart from the spiked DEHP, that also contribute in the impedance measurements. The solution to this problem required the selectivity characteristics to be induced in the sensor for the specific analyte molecule (DEHP in this case).

5.2.7 Impedance Measurements of DINP-Spiked Ethanol Samples

All phthalates including DINP are synthetic oily compounds that do not dissolve in an aqueous medium. On the other hand, are soluble in all organic solvents. Experiments were conducted to investigate the capability of the sensing system for phthalate detection in alcohol-based beverages. Although, alcohol based drinks are supplied in glass bottles yet research has declared that the cork stopper used in glass bottled drinks leach phthalates, and the migration is even faster in this case by virtue of the solubility properties of alcohol [10].

Four different concentrations of DINP-in-Ethanol; 0.1, 0.5, 1 and 20 ppm were tested at room temperature using the designed real-time detection system.

Control solution is 99.6 % pure ethanol with pH 6.71. It was observed that addition of DINP in the working solutions did not alter their pH level and their average pH value observed was 6.52 at 20 °C. The sensor was profiled in the air before its exposure to the different DINP concentrations. Figure 5.15 shows the Nyquist plot for the impedance spectrum obtained. It was observed that the plot did not display diffusion-limited process (Warburg Resistance) in the selected frequency range which is attributed to Si_3N_4 coating on the sensing area and absence of redox-active compound in the solution [16] The high value of charge transfer resistance (R_{ct} is 5 M Ω for air and control) calculated from the plot depicts the

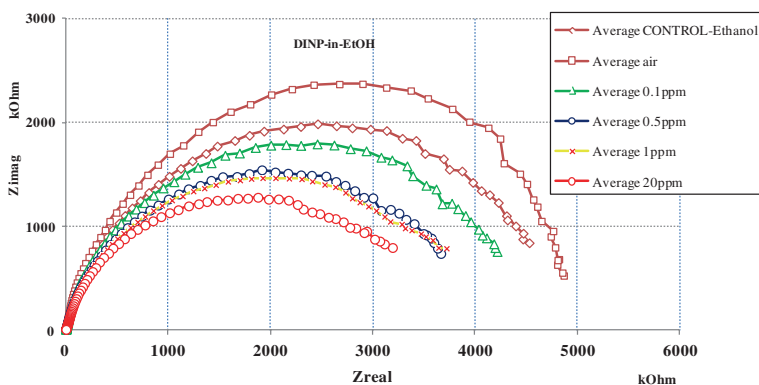


Fig. 5.15 Nyquist plot for DINP concentration test in EtOH

charge transfer process. The double layer capacitance (C_{dl}) appears due to the layer of charges formed at the electrode-solution interface, at this point, it had a value of 0.115 nF for air and 0.113 nF for the control solution. The corresponding values of C_{dl} for 0.1, 0.5, 1 and 20 ppm DINP concentrations are calculated to be 7.7, 96.95, 100 and 113.2 nF respectively. The change in the value of the C_{dl} corresponded to the change in the concentration of DINP in ethanol. It is observed that the sensor is highly sensitive at low frequencies (6–100 Hz). The reactance (imaginary Impedance) of the sensor dominates the real impedance showing its capacitive behavior. Figures 5.16 and 5.17 show the real and imaginary impedance plotted against frequency respectively.

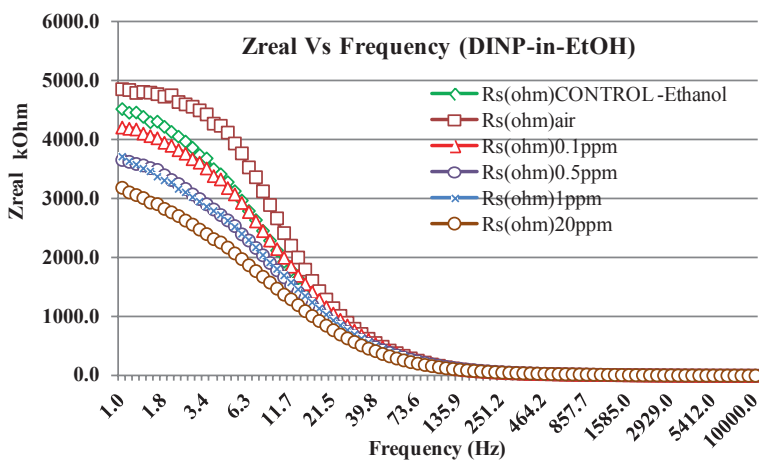


Fig. 5.16 Real part of impedance for DINP-in-EtOH

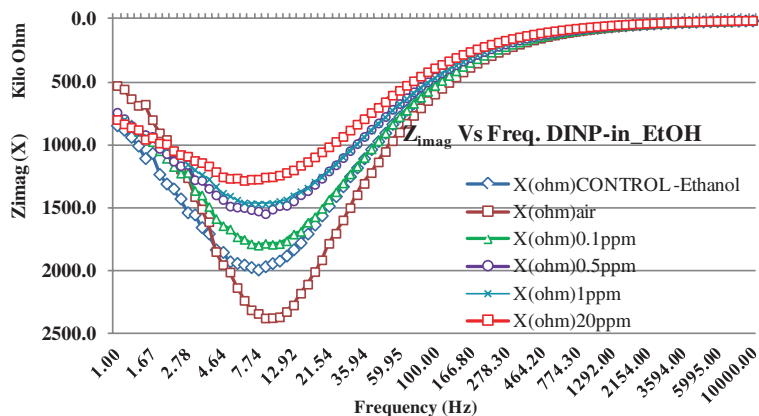


Fig. 5.17 Imaginary part of impedance for DINP-in-EtOH

A sequential decrease in the reactance is observed with the increasing concentration of DINP in EtOH as illustrated in Fig. 5.17.

5.2.8 Impedance Measurements of DINP-Spiked Orange Juice

Assuming that glass bottled juices are phthalate-free in New Zealand, 5, 10 and 20 ppm DINP was added to a locally available orange juice (average pH of 3.47 at 20 °C). Control for this set of samples was un-spiked (no added DINP) juice [25]. Figure 5.18 shows the Z_{real} impedance plot for the results which show that the sensor was able to translate the DINP concentration in the samples in terms of reactance.

It was observed that the acidic medium has reduced the solution resistance ten folds as compared to the test in ethanol medium. It happened due to the presence of ionic concentration in the medium; therefore, the process of ionic diffusion takes place in the solution at the electrode-solution interface on the application of electrical perturbations. Consequently, it caused a drastic decrease in the solution resistance. Figure 5.19 shows the imaginary part of impedance measured in testing spiked orange juice with the proposed detection system.

The presence of other chemicals in the complex matrix like orange juice has drastically affected the sensitivity of the sensor, which can be seen from the plotted imaginary impedance curves for different concentrations of DINP in orange juice. The range of frequency for which the sensor has shown the presence of DINP (6.31–39.81 Hz) has reduced; additionally, the magnitude of change in

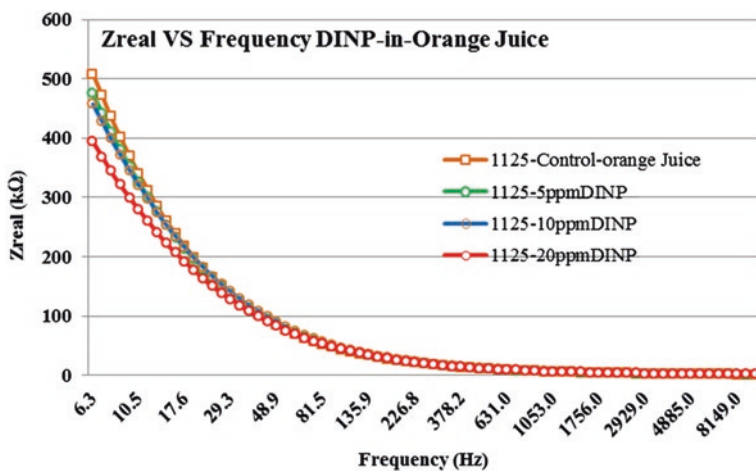


Fig. 5.18 Real part of measured impedance for DINP in orange juice

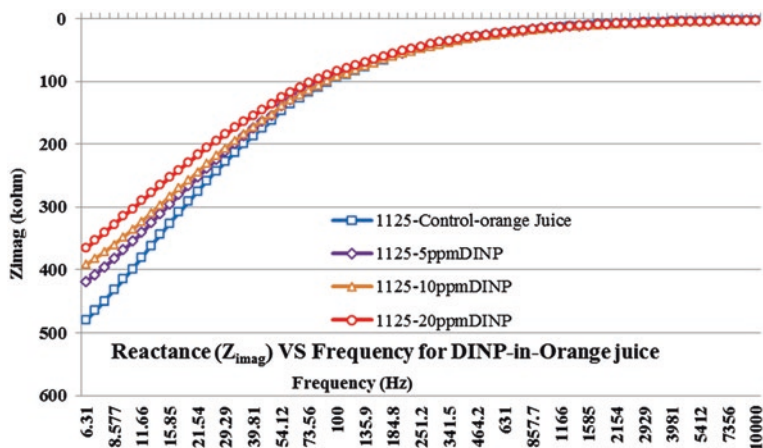


Fig. 5.19 Reactance plot for DINP-in-Orange juice

reactance of the sensor has eroded. The test results of DINP in orange juice were not too different to the test results of DEHP in the energy drink. The system was unable to detect the trace level concentrations of phthalates in complex solutions like drinks and juices.

5.3 Conclusions

The developed sensor and sensing system was employed to detect two types of phthalates spiked in different kinds of mediums. The tests were performed in real-time and the sensor performed successfully in the detection of phthalates in the pure polar medium. The system was able to detect the presence of DEHP and DINP even to a trace level in the polar medium, but the outcomes of the investigation made for electrolytic and acidic media were not up to the mark. Although, the sensitivity analysis of the system displayed a high level of sensitivity in pure aqueous and organic solvent media yet, the system sensitivity deteriorated drastically in complex solutions. This led the sensing system research to the next stage of development. In order to adapt the sensor and sensing system for complex chemical matrices like beverages, milk and urine, selectivity for analyte molecules was an absolute requirement. Different options to pave the way to selective adsorption of phthalates on the sensing surface have been explored.

Published research provides a number of methods to detect selectively analyte from a complex matrix by extraction, absorption, adsorption, biological separation and filtration. Unfortunately, all these techniques are laboratory based and require certain skills and expertise to perform. On the other hand, these techniques are extremely delicate and require certain environmental conditions to execute.

One of the main objectives of this research was to develop an assay system that is robust enough to have an in-field application without any technical expertise requirement for the user. In order to achieve this objective, a robust assay technique was tailored and applied to induce selectivity in the designed sensing system. The discussion on inducing selectivity for the target molecules is carried out in the next chapter.

References

1. T. Schettler, Human exposure to phthalates via consumer products. *Int. J. Androl.* **29**(1), 134–139 (2005)
2. U. Heudorf, V. Mersch-Sundermann, J. Angerer, Phthalates: toxicology and exposure. *Int. J. Hyg. Environ. Health* **210**(5), 623–634 (2007)
3. R. Hauser, S. Duty, L. Godfrey-Bailey et al., Medications as a source of human exposure to phthalates. *Environ. Health Perspect.* **112**(6), 751 (2004)
4. Toxicity Uscpsc, *Review of DEHP* (Bethesda, MD, USA, 2010)
5. J.D. Meeker, A.M. Calafat, R. Hauser, Urinary metabolites of di (2-ethylhexyl) phthalate are associated with decreased steroid hormone levels in adult men. *J. Androl.* **30**(3), 287 (2009)
6. L. López-Carrillo, R.U. Hernández-Ramírez, A.M. Calafat et al., Exposure to phthalates and breast cancer risk in northern Mexico. *Environ. Health Perspect.* **118**(4), 539 (2010)
7. V. Triantafyllou, K. Akrida-Demertzi, P. Demertzi, A study on the migration of organic pollutants from recycled paperboard packaging materials to solid food matrices. *Food Chem.* **101**(4), 1759–1768 (2007)
8. M.R. Lee, F.Y. Lai, J. Dou et al., Determination of trace leaching phthalate esters in water and urine from plastic containers by solid-phase microextraction and gas chromatography-mass spectrometry. *Anal. Lett.* **44**(4), 676–686 (2011)
9. P. Montuori, E. Jover, M. Morgantini et al., Assessing human exposure to phthalic acid and phthalate esters from mineral water stored in polyethylene terephthalate and glass bottles. *Food Addit. Contam.* **25**(4), 511–518 (2008)
10. R. Sendón, A. Sanches-Silva, J. Bustos et al., Detection of migration of phthalates from agglomerated cork stoppers using HPLC-MS/MS. *J. Sep. Sci.* **35**(10–11), 1319–1326 (2012)
11. WHO, *WHO Guidelines for Drinking-water Quality*, 4th edn. (World Health Organization, 2011)
12. J. Yang, R. Hauser, R.H. Goldman, Taiwan food scandal: the illegal use of phthalates as a clouding agent and their contribution to maternal exposure. *Food Chem. Toxicol.* **58**, 362–368 (2013)
13. A. Schecter, M. Lorber, Y. Guo et al., Phthalate concentrations and dietary exposure from food purchased in New York State. *Environ. Health Perspect.* **121**(4), 473 (2013)
14. J.A. Colacino, A.S. Soliman, A.M. Calafat et al., Exposure to phthalates among premenstrual girls from rural and urban Gharbiah, Egypt: a pilot exposure assessment study. *Environ. Health* **10**(1), 40 (2011)
15. J.D. Meeker, A.M. Calafat, R. Hauser, Di (2-ethylhexyl) phthalate metabolites may alter thyroid hormone levels in men. *Environ. Health Perspect.* **115**(7), 1029 (2007)
16. H.M. Koch, R. Preuss, J. Angerer, Di (2-ethylhexyl) phthalate (DEHP): human metabolism and internal exposure—an update and latest results I. *Int. J. Androl.* **29**(1), 155–165 (2006)
17. X.L. Cao, Determination of phthalates and adipate in bottled water by headspace solid-phase microextraction and gas chromatography/mass spectrometry. *J. Chromatogr. A* **1178**(1–2), 231–238 (2008)
18. A.D. LaFleur, K.A. Schug, A review of separation methods for the determination of estrogens and plastics-derived estrogen mimics from aqueous systems. *Anal. Chim. Acta* **696**(1), 6–26 (2011)

19. J. Li, Y. Cai, Y. Shi et al., Analysis of phthalates via HPLC-UV in environmental water samples after concentration by solid-phase extraction using ionic liquid mixed hemimicelles. *Talanta* **74**(4), 498–504 (2008)
20. Z. Guo, D. Wei, M. Wang et al., Determination of six phthalic acid esters in orange juice packaged by PVC bottle using SPE and HPLC-UV: application to the migration study. *J. Chromatogr. Sci.* **48**(9), 760–765 (2010)
21. S. Hird, Mass spectrometry in food safety: methods and protocols methods in molecular biology (vol. 747), in *Rapid Communications in Mass Spectrometry*, vol. 26, no. 9, ed. by J. Zweigenbaum (Springer, New York, 2012), pp. 1162–1164
22. A.I. Zia, M.S.A. Rahman, S.C. Mukhopadhyay et al., Technique for rapid detection of phthalates in water and beverages. *J. Food Eng.* **116**(2), 515–523 (2013)
23. Z. Kerner, T. Pajkossy, Measurement of adsorption rates of anions on Au (111) electrodes by impedance spectroscopy. *Electrochim. Acta* **47**(13), 2055–2063 (2002)
24. A.I. Zia, A.M. Syaifudin, S. Mukhopadhyay et al., Electrochemical impedance spectroscopy based MEMS sensors for phthalates detection in water and juices. *J. Phys. Conf. Ser.* **439**, 012026 (2013)
25. A.I. Zia, A.R. Mohd Syaifudin, S.C. Mukhopadhyay et al., MEMS based impedimetric sensing of phthalates. pp. 855–860

Chapter 6

Inducing Analyte Selectivity in the Sensing System

6.1 Introduction

The need for the development of fast, sensitive and highly selective chemical and biochemical sensors for applications related to complex matrices of medical, environmental and industrial interests has been a subject of ultimate research and development recently. A number of chemical and biochemical sensors have been designed by making use of enzymes, antibodies, membranes, carbon nanotubes, magnetic nanoparticles and supramolecular assemblies to realize the sensing elements for chemical and biochemical analytes [1–3]. However, the availability of biocomponent required, or the mandatory requirement of stability and reproducibility in chemical and biochemical recognition remained unachieved. Therefore, all the techniques and assays developed stayed restrained to laboratories. The aim of rapidness and robustness in chemical and biochemical recognition had been an ambition for the researchers in this field.

Recent studies in polymer science demonstrated that use of analyte (organic template) could create imprinted cavities in cross-linked polymers and has proved to be the most efficient way of polymerizing synthetic materials bearing selective molecular recognition sites for the analyte. Since the chemical, physical and electrical properties of the polymers may be tailored over a wide range of characteristics, sophisticated and hi-tech electronic and electrical sensing devices have a huge potential of placing polymers at a permanent collaborative position in the field of chemical and biochemical sensing [4, 5].

The developed methodology is based on chemical, physical or electrical interaction of the analyte, called print molecule or template, with a functional monomer to polymerize together. A rigid, cross-linked, macro-porous polymer is formed that contains the analyte packed in the synthesized polymer. On removal of the print molecule by elution, specific sites are left behind that are complementary to the print molecule in shape and arrangement with an outstanding capability of rebinding the template and structurally related analytes. The polymer with the “memory” of the analyte hence gets the name of ‘Molecular Imprinted Polymers’ (MIPs) [6–8].

Molecular imprinted polymers (MIPs) are specially designed polymerized materials owing valuable molecular recognition capabilities. These possess specific cavities designed for a target molecule, privileged by unique advantages like high selectivity, physiochemical stability and specific recognition of analyte and structurally related compounds.

Molecular imprinted polymers could be synthesized by applying a number of approaches like precipitation, bulk, suspension, swelling, miniemulsion and core-shell polymerizations depending on the application [7]. Figure 6.1 shows the steps involved in the synthesis of MIP and Fig. 6.2 shows the extraction process making molecular recognition sites available in the polymer matrix for selective extraction.

Latest research depicts that molecular imprinting technique has rigorously been used to extract the phthalate analytes from the samples as an application for sample clean-up to quantify DEHP by using gas chromatography [9–11]. The entrapment of target molecules is achieved by two established strategies using covalent or non-covalent interactions of the target molecule with the functional monomer. Non-covalent approach makes use of instinctive intermolecular forces present between the target and monomer molecule. This molecular recognition selectivity

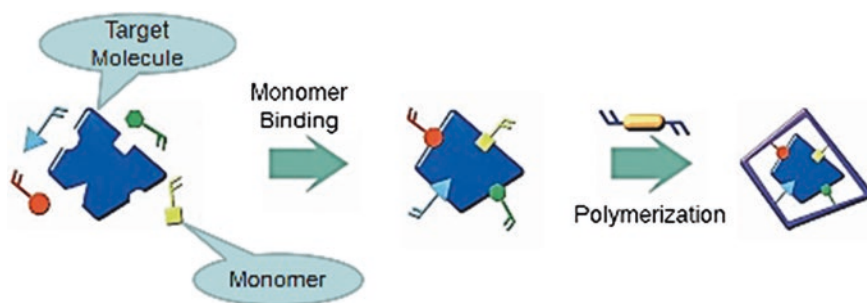


Fig. 6.1 Synthesis process of molecular Imprinted Polymer

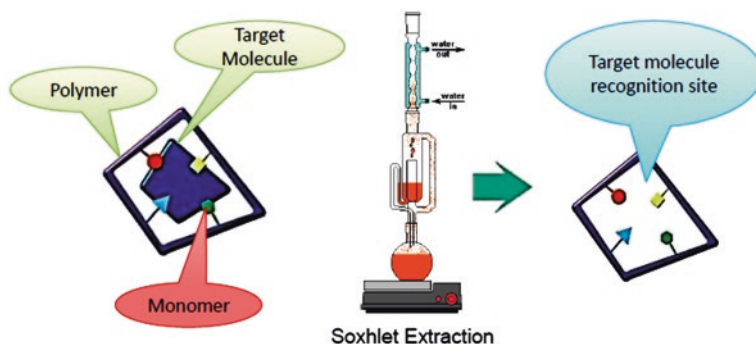


Fig. 6.2 Extraction of template molecule forming molecular recognition site in MIP

has proved to be an attractive predominant advantage for separation and analyses of complicated samples and has been applied in several contexts e.g. solid phase extraction (SPE) [10, 12], chromatography [13], electro-chromatography [14], membrane filtration and sensing. It has obvious advantages over biological receptors and antibodies of more number of target molecule capturing sites [13]. MIPs are intrinsically stable robust and reusable. These relatively weak forces could be hydrogen bonding, ion pair, dipole-dipole interactions or van der Waals forces between the two molecules. This is the most commonly used approach since it requires minimal effort to remove the entrapped molecules from the molecular recognition sites whereas the covalent bonding requires additional steps to release the entrapped molecules [15]. Molecular imprinted micro and nano-spheres applied for DEHP determination have been reported as a product of precipitation polymerization for MIP [16]. The microspheres exhibited a strong DEHP molecular affinity and the authors evaluated an imprinted factor (IF) of higher than 8 in their reported research [16]. Yan et al. reported the synthesis of a new imprinted microsphere for DINP by precipitation polymerization and determined the PAEs in plastic bottled beverages as an application. The average recovery of the five PAEs at three different spiking levels was found to be ranging from 84.3 to 96.2 % for different phthalate molecules [17].

In the presented research, a selective MIP for DEHP was synthesized by the process of suspension polymerization with the use of methacrylamide as a functional monomer. DEHP molecule was used as template with N,N-methylene-bis-acrylamide behaving as a cross-linker molecule to polymerize the MIP. The adsorbed DEHP was extracted using soxhlet extraction method through methanol. The MIP was air dried and immobilized on the ID sensor for rapid quantification of DEHP in aqueous medium by electrochemical impedance spectroscopy application studies.

6.2 Materials and Methods

Di(2-ethylhexyl) phthalate (DEHP). N,N-methylene-bis-acrylamide, methacrylamide, ammonium persulfate, methanol, ethanol, acetonitrile, chloroform, dimethyl formamide (DMF), dichloromethane and 3-aminopropyltriethoxysilane (APTES) were procured from Sigma Aldrich, Germany. Deionized (DI) water MilliQ® was obtained from MILLIPORE water system (USA)–18 M Ω cm. Gravimetrically prepared di (2-ethylhexyl) phthalate (DEHP) solution at a concentration of 200 $\mu\text{g}/\text{mL}$ (200 ppm) in ethanol (99.5 % purity) was ordered and received from ChemService® USA. Other working solutions of lower concentrations were achieved by serial dilution method in the deionized water MilliQ®. Pure deionized water with a 100 ppm concentration of ethanol was used as control solution for the experiments. pH meter from IQ Scientific Instrument Inc. USA was used to measure pH levels of the spiked and control solutions. The device was calibrated with buffer solutions provided by the manufacturer.

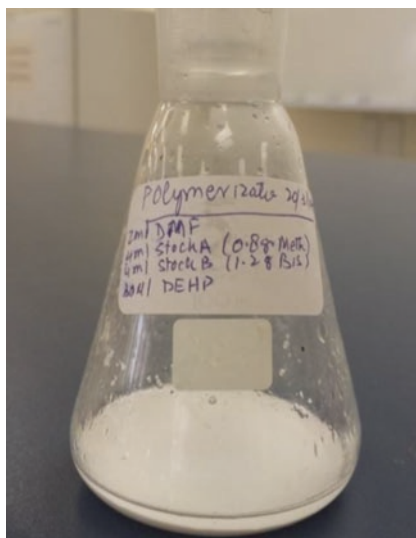
6.2.1 Synthesis of DEHP Imprinted Polymer

A DEHP selective molecular imprinted polymer was synthesized by suspension polymerization using methacrylamide as a functional monomer attaching itself to DEHP molecule via hydrogen bonds. N,N-methylene-bisacrylamide was used as crosslinker for polymerization reaction. Ammonium persulfate was used as initiator for synthesis of the polymer. A solution of 2.5 mL DMF, 7.5 mL MilliQ water, 14.5 mmol methacrylamide and 1 mL DEHP was prepared in an ice bath and functional monomer and template (DEHP) molecules were allowed to generate hydrogen bonds between DEHP and methacrylamide (monomer) in the presence of nitrogen atmosphere. 5.3 mmol N,N-methylene-bisacrylamide (cross linker) and 0.7 mmol ammonium persulfate (initiator) were added to the mixture and stirred until dissolved in the solution in a flask installed with a reflux condenser and a magnetic stirrer as shown in Fig. 6.3. The cold water circulation in the reflux condenser was used to avoid any evaporation from the polymerization flask. The solution was kept at 50 °C for 8 h in order to complete the polymerization reaction.

MIP was filtered, washed with deionized water and dried under nitrogen flow (Fig. 6.4). MIP was ground and sieved to obtain 90 μm particle size. DEHP (template) was extracted out of the MIP powder encapsulated in 0.22 μm filter caplet by Soxhlet extraction in 12 h with methanol as shown in Fig. 6.5. Extraction of DEHP in 0.22 μm filter is shown in Fig. 6.6.

Fig. 6.3 Polymerisation reaction



Fig. 6.4 Polymerized MIP

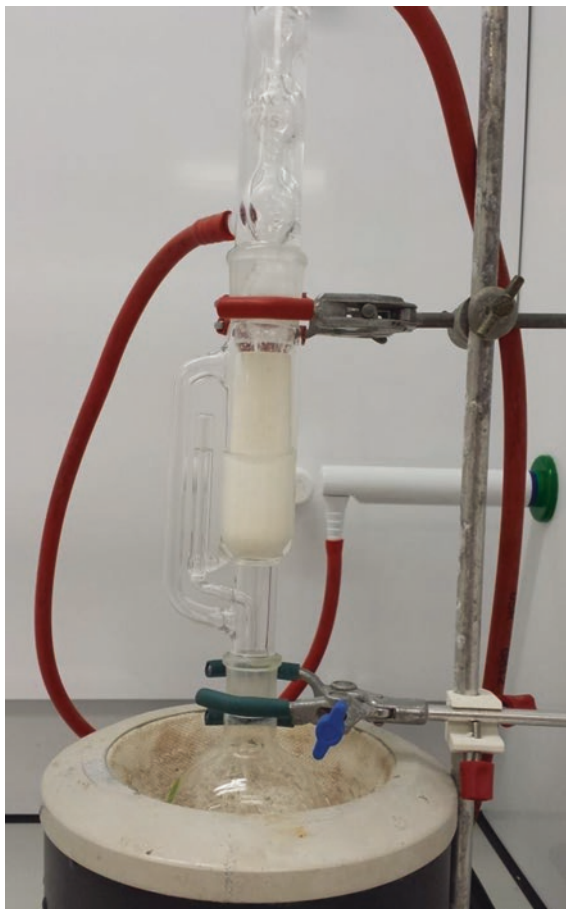
MIP powder was dried under nitrogen at room temperature. Self-assembled monolayer of 3-aminopropyltriethoxysilane (APTES) was used to immobilize MIP functional coating on the sensing surface of the sensor by dip coating method. 2 g MIP powder was mixed with 2.5 mL APTES and 1.5 mL of DI water to prepare a coating suspension. The sensor was dipped in the suspension and was withdrawn at a slow rate of 2.5 mm per minute to achieve a uniform coating on the sensing surface. The dip coated sensor was dried for 18 h under nitrogen at room temperature prior to testing. Figure 6.7 shows the MIP in 90 μm sieved powdered form after extraction of template (DEHP) (Fig. 6.8).

The coating was observed under optical microscope for surface morphology and porosity. Figure 6.9 shows confocal micrograph image of MIP-coated sensor depicting that the MIP embedded Self-Assembled Monolayer coating on the sensing surface is uniform and porous.

Two identical sensors 1-11-50A and 1-11-50B were coated and profiled in an inert atmosphere at 24 % humidity and 23.3 $^{\circ}\text{C}$ temperature. Figure 6.10 shows the dip coating process of the sensors and Fig. 6.11 shows drying under an inert atmosphere for 18 h in a desiccator.

6.3 EIS for Detection of DEHP in MilliQ

Electrochemical Impedance Spectroscopy technique owns high sensitivity with limitation of stable and reversible system in equilibrium. Therefore for non-stationary systems instantaneous impedance measurements are mandatory. In case of non-compliance, system linearity, stability and repeatability could not be ensured.

Fig. 6.5 Soxhlet extraction

In order to overcome these challenges all experiments were conducted under identical temperature, humidity, and pH boundary condition in controlled laboratory environment. The sensor was connected to Hioki 3522-50 LCR Hi precision tester (Japan) by gold contact clamp pin connector. The device was run with built in open and short calibration tests to nullify any stray capacitance due to connecting leads. LCR tester was set to slow mode of testing to achieve error rate of $<0.05\%$ as recommended by the manufacturer. The sensor setup was formed in a desiccator to achieve the required controls of 24% humidity and inert atmosphere. To obtain a reference, the sensor was profiled in air for a frequency sweep of 2 MHz to 42 Hz with ten measurements per decade change in frequency at the log scale. Three different concentrations of DEHP— 1 , 10 , and 50 mg L^{-1} (ppm) in deionized water were tested at initial temperature ($23.3\text{ }^{\circ}\text{C}$) and humidity (24%) conditions. Control solution was $18\text{ M}\Omega\text{ cm}$ deionized MilliQ water with pH 6.71 .

Fig. 6.6 Filter caplet
0.22 μm



Fig. 6.7 DEHP extracted
MIP

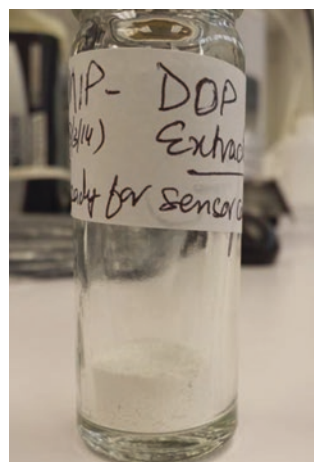


Fig. 6.8 MIP coated sensor using SAM of APTES

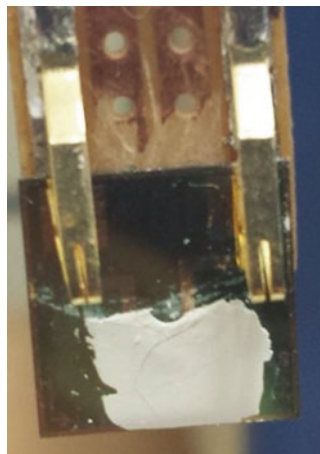
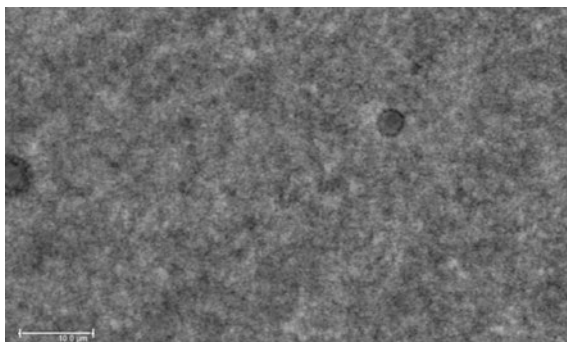


Fig. 6.9 Confocal micrograph image of MIP coated sensor



It was observed that addition of DEHP in the working solutions did not alter pH level and average pH value measured was 6.52 at 23.3 °C. The sensor was profiled in air before its exposure to the different DEHP concentrations to create an experimental reference curve for sensor performance. The immobilized MIP sensor was pipetted with 10 μL of MilliQ water and the test was run to generate control reference curve, later the MIP functionalized sensor was pipetted with 10 μL 1 ppm solution. A seven minutes time period was allowed for polymer to entrap DEHP molecules from the test sample. Figure 6.12 shows the lab test bench set up for MIP coated sensor testing.

The MIP was washed with acetone and rinsed with distilled water in order to remove excess/un-bound DEHP molecules and the EIS testing was executed thrice under same initial temperature and humidity conditions. The MIP-coated sensor was sonicated in dichloromethane for half an hour to remove the entrapped DEHP molecules and regenerate the functionalized MIP coating. The eluent was preserved and later tested with HPLC for validation of DEHP entrapment. The



Fig. 6.10 Dip Coating process

Fig. 6.11 Drying in nitrogen flow



sensor surface was dried with nitrogen and profiled in air in order to evaluate and ensure achievement of initial conditions of the EIS testing system before each run. Each concentration was tested with the proposed system following the described procedural steps. The control reference was plotted by executing experiment after pipetting 10 μl control solution on the MIP functionalized sensing area of the sensor.



Fig. 6.12 Laboratory test bench setup for MIP coated sensor

6.3.1 Results and Discussions

Molecular imprinted polymers (MIP) are specially designed polymer materials owing valuable target molecules recognition sites, privileged by unique advantages like high selectivity, physiochemical stability, robustness, longer shelf life, reusability and specific recognition of analyte and structurally related compounds. This molecular recognition selectivity has proved to be an attractive predominant advantage over biological receptors and antibodies for more number of target molecule capturing sites [13]. MIPs have been applied in SPE, chromatography, electro-chromatography, membrane filtration and sensing [18, 19]. Lately molecular imprinting technique has rigorously been applied to extract phthalate analytes as a sample clean up prior to quantification of DEHP by gas chromatography [9]. The analyte could be entrapped by MIP either by covalent or non-covalent bonding, which is accepted as a well-established technique for analyte capture for sample clean-up [14]. Non covalent bonding makes use of relatively weak forces like hydrogen bonding, ion pair, dipole–dipole interactions or van der Waal forces to entrap target molecules. This approach is more appreciated because it requires minimal efforts to remove the target molecules from the recognition sites, whereas, covalent entrapment requires energy transfers to break the bond in order to remove the analyte [9, 20, 21].

6.4 Adsorption Studies of DEHP to MIP

The extraction of adsorbed DEHP from the sensor's functionalized coating was carried out in an equal volume (2 mL) of dichloromethane by sonication process of 15 min at all instances. The solvent was evaporated and 50 μL dichloromethane was used for HPLC testing of the eluent. Luna C18 column was used in DIONEX HPLC system to test the samples at a wavelength of 224 nm for diode array detector (DAD) with a mobile phase of methanol/acetonitrile (1:9 v/v). The binding isotherms of DEHP to MIP were determined in the concentration range of 1–100 $\mu\text{g mL}^{-1}$. Adsorption studies helped us to determine two important parameters about the functionalized coating on the sensing surface. Firstly, we can determine the highest concentration that could be adsorbed by the immobilized MIP and secondly, time of adsorption could be determined for the amount of MIP immobilized on the sensing surface. Highest adsorption concentration can be studied by static adsorption investigation (Sect. 6.4.1) whereas, uptake kinetic studies (Sect. 6.4.2) can provide the information about the time of adsorption which is an important parameter to know for quasi-static electrochemical cell in order to keep the system in steady-state for EIS measurements.

6.4.1 Static Adsorption of DEHP to MIP

The static adsorption of MIP was calculated using Eq. 6.1.

$$Q = \frac{(C_i - C_f)V}{m} \quad (6.1)$$

where Q (mg g^{-1}) is the mass of DEHP adsorbed per gram of MIP, C_i (mg L^{-1}) is the initial concentration of DEHP; C_f (mg L^{-1}) is final concentration of DEHP after adsorption. V (l) is the total volume of the adsorption mixture and m (g) is the mass of the polymer used. The isotherm for the static adsorption studies of DEHP to MIP is shown in Fig. 6.13.

The plot depicts that the amount of DEHP bound to the polymer increases with the increase in concentration of the DEHP in the test samples below a concentration level of 50 mg l^{-1} (ppm). The polymer saturates as the concentration level increases above the said limit and the curve becomes parallel to concentration axis. This is due to the fact that the miniature size of sensor allows very less MIP immobilized on the sensing surface. Since the targeted range of detection is lower to the saturation limit therefore, it is deemed acceptable [22].

Fig. 6.13 Isotherm for the static adsorption studies of DEHP to MIP

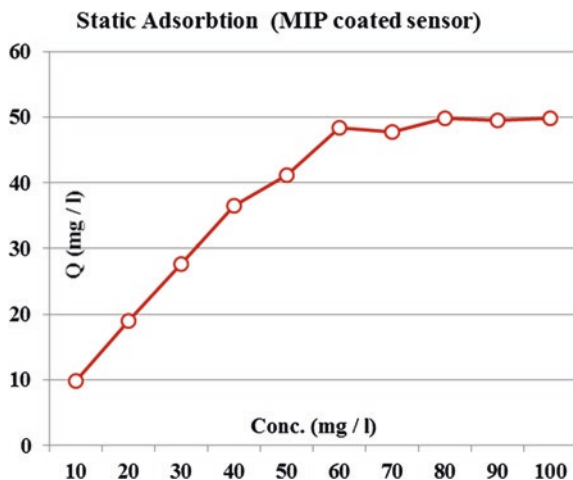
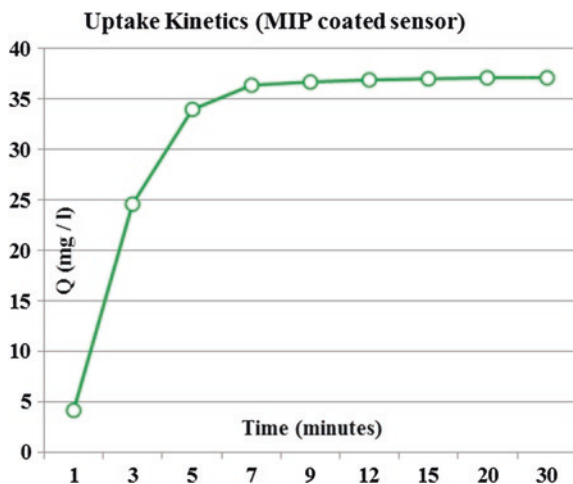


Fig. 6.14 Isotherm for adsorption uptake kinetics of DEHP to MIP



6.4.2 Uptake Kinetics of MIP Coated Sensor to DEHP

Figure 6.14 presents the plot for adsorption uptake kinetics of DEHP to MIP. This study was helpful to determine the adsorption time required by DEHP present in the sample to get trapped at the molecular recognition sites in the MIP. The coated sensor was dipped in 5 mL test solution with a concentration of $50 \mu\text{g mL}^{-1}$.

The concentration level was chosen in the light of static adsorption studies undertaken in Sect. 6.4.1. The results showed that the MIP owns fast entrapment kinetics, and the binding equilibrium was reached in almost 7 min. The rapid adsorption capability of the MIP is an advantage for using the polymer with

electrochemical impedance spectroscopy where rapid impedance measurements are mandatory for non-stationary systems.

6.5 Data Analyses Using Nonlinear Least Square Curve Fitting

Figure 6.15 shows the Nyquist plot for the experimentally obtained real and complex impedance. The decreasing diameter of the Nyquist plot indicates the increasing concentration of the phthalate in the sample. It is observed that the sensor is sensitive to the adsorbed phthalate molecules at low frequencies. The mass transfer of ions in the electrode surface is a fast kinetic process which is taking place at low frequency range, on the other hand the capacitive behaviour of the sensor is observed at relatively high frequency range. The semi-circular portion describes a relatively slower charge transfer limited process at higher frequencies. C_{dl} can be calculated from the frequency at the maximum of semi-circular region in the Nyquist plot using $\omega = 2\pi f = 1/R_{ct}C_{dl}$ whereas, R_{ct} is calculated by extrapolating the semicircle to Z_{real} axis. The double layer capacitance C_{dl} and charge transfer resistance R_{ct} are the key electrical parameters in determination of impedance change for analytical studies of the system kinetics in the detection of the phthalates. The values of R_{ct} decreases to 80 k Ω from 130 k Ω as the concentration of DEHP increases from 0 ppm to 50 ppm as shown in Fig. 6.15.

The equivalent circuit was estimated using theoretical calculations by electrochemical spectrum analyser algorithm as illustrated in Fig. 6.16.

The circuit parameters were estimated by a complex non-linear least square fitting technique which fits the measured impedance data on theoretically estimated

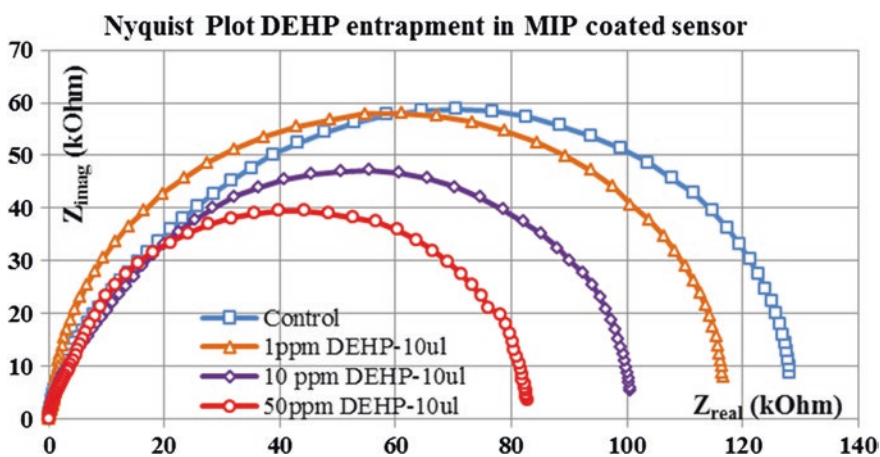


Fig. 6.15 Nyquist plot for EIS testing of MIP coated Sensor

Fig. 6.16 Equivalent circuit estimated by CNLS analysis

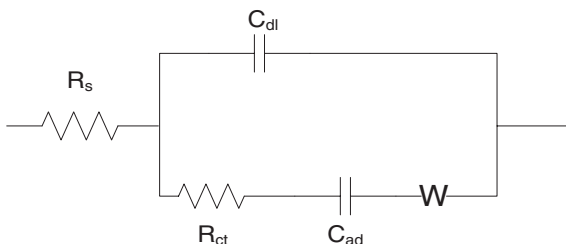


Table 6.1 CNLS curve fitted equivalent circuit parameters

Parameter (unit)	DEHP test samples in DI water					
	1 ppm		10 ppm		50 ppm	
	Value	Error (%)	Value	Error (%)	Value	Error (%)
C_{ad} (F)	3.37E-08	2.43	3.77E-08	2.72	5.50E-08	1.96
R_s (Ω)	7.2	3.42	6.00	2.61	1.32	2.44
R_{ct} (Ω)	1.29E+05	3.95	9.97E+04	4.07	8.42E+04	4.42
Z_w (Ω)	1.78E-06	13.96	1.57E-06	14.68	9.52E-05	15.44
C_{dl} (F)	1.01E-09	3.64	9.03E-10	3.79	7.07E-10	18.97
r^2	5.859E-04		4.395E-04		6.782E-04	

values. The algorithm performs statistical analysis to calculate the residual mean square $r_{amplitude}^2$ for experimentally observed values in measured spectra against the calculated values based on the theoretical response of suggested equivalent circuit. (Table 6.1).

The results of curve fitting show that the adsorption capacitance increases with the rise in the concentration of the analyte in the test samples whereas; the charge transfer resistance is decreasing with the increasing concentration. The new results with the selective coating are in compliance to the earlier experiments with DEHP in an aqueous medium. The Warburg resistance has reduced to zero due to the self-assembled monolayer of APTES embedded with MIP particles. APTES provides good adhesion with the silicon dioxide layer present at the sensing surface. Since ionic concentration in the test sample is not present and the SAM of APTES provides sound insulation between the sensing surface and the electrolyte. Therefore the existence of Warburg resistance is nominal which proves that the capacitive characteristics of the sensor have enhanced due to the coating of MIP.

6.6 Results Validation by HPLC

The eluent collected after the extraction of adsorbed DEHP from sensing surface was filtered with 0.22 μm filter, solvent was evaporated and 50 μl methanol was used for HPLC testing of the eluent. Luna C18 column was used in

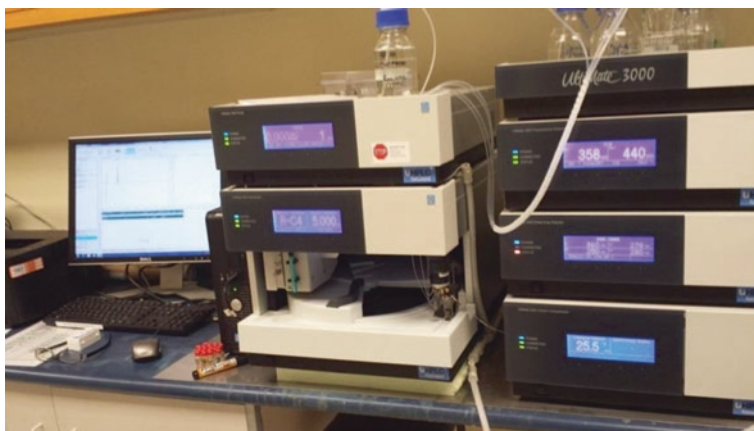
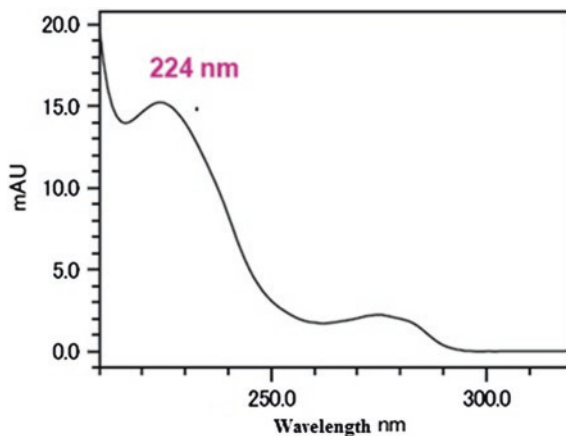


Fig. 6.17 DIONEX-Ultimate 3000 HPLC apparatus

Fig. 6.18 Absorption spectrum of DEHP



DIONEX HPLC system to test the samples at a wavelength of 224 nm for DAD with a mobile phase of methanol/acetonitrile (1:9 v/v) in order to validate the EIS results. Figure 6.17 shows the DIONEX HPLC apparatus in the Micro-suite laboratory which is a programmable self-injecting semi-automatic piece of equipment.

Figure 6.18 shows the peak absorption wavelength in absorption spectrum of DEHP.

The HPLC peak was observed at 6.19 min with C18 (1504.6 mm) column at a flow rate of 1 mL/min of the mobile phase. Un-spiked methanol was used as a control reference for detecting concentrations of 1 mg/L to 100 mg/L in methanol. The plots for the observed DEHP peaks are shown in Fig. 6.19. The area under the peaks determined the concentration of DEHP in the sample.

Fig. 6.19 MIP eluent tested with HPLC for EIS results validation

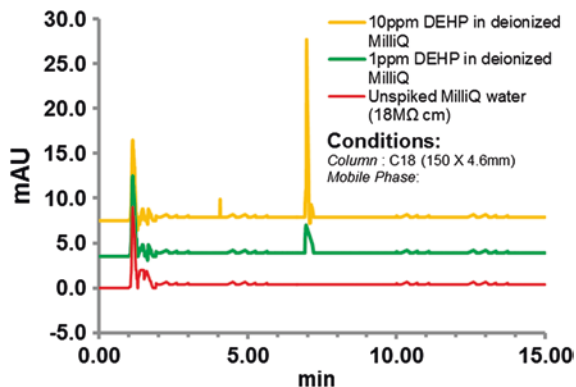
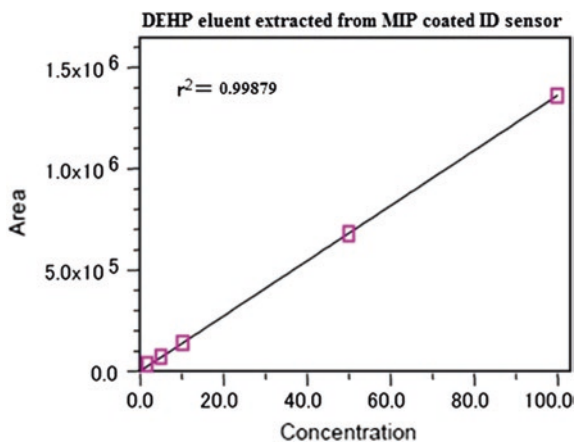


Fig. 6.20 DEHP eluent extracted from MIP immobilized on ID sensor



The chromatograph shows a few peaks at 1.2 min which correspond to the solvent. The DEHP concentrations read by HPLC in the eluent are marked in Fig. 6.20.

The calibration curve shown in Fig. 6.20 was plotted using samples of known concentration in MeOH. The square marks indicated on the plot represent the concentration read by the HPLC.

6.7 DEHP in Energy Drink—MIP Coated Sensor

Commercially available energy drink (Lift Plus) was spiked with DEHP at a concentration of 1, 5, and 10 ppm. The drink is sold in New Zealand markets in glass bottle packaging. Therefore, the possibility of the addition of leached DEHP from the packaging was ruled out. The spiked drink samples were tested with MIP

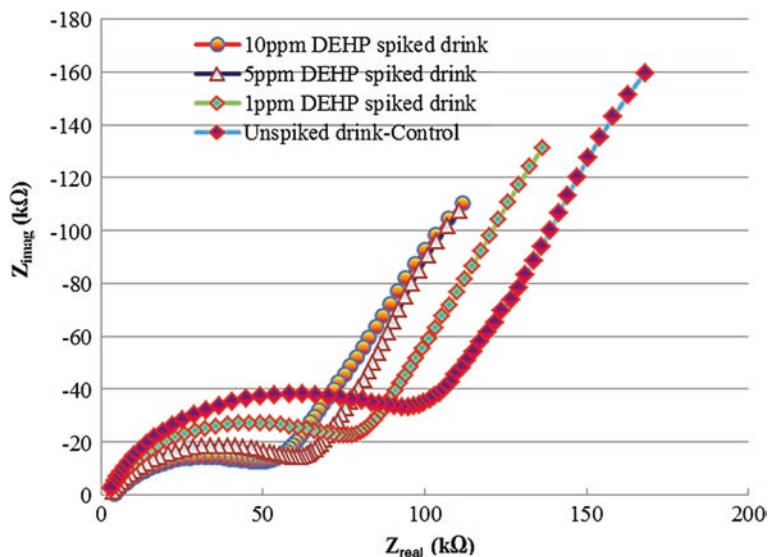


Fig. 6.21 Nyquist plot for DEHP spiked drink by MIP coated sensor

functionalized interdigital sensor by electrochemical impedance spectroscopy and the eluent after extraction of DEHP from the sensor's coating was injected to HPLC for validation.

Figure 6.21 shows the Nyquist plot for the impedance data measured by the MIP functionalized sensor. It should be noted that all the steps in the test procedure were identical to the test with spiked deionized water as explained in Sect. 6.3.

The change in the impedance read by the developed EIS system showed that the concentration of the analyte is changing in the spiked drink. The 45° tail line with the semi-circular curve in the plot showed the presence of Warburg resistance in the equivalent circuit. The appearance of Warburg resistance strictly dictated the presence of ions in the spike samples that is attributed to the electrolytes present in the energy drink. The correlation plot for the reactance read by the MIP coated sensor in energy drink tainted with DEHP at various concentration levels is illustrated in Fig. 6.22. The coefficient of determination with a value of 0.9592 illustrates a good compliance between the actual and read concentration levels. The obtained results were validated by injecting desorbed eluent from the MIP coating for all concentrations using HPLC.

The current flowing through the circuit due to conductive medium dictated the value of the resistance. The equivalent circuit parameters are shown in Table 6.2.

The smart system results were validated by HPLC analysis. The chromatogram in Fig. 6.23 shows DEHP peaks at 6.91 min. The peaks that appeared before DEHP peak are due to the presence of other chemicals in the eluent. These might get attached to the MIP due to its porous nature. This problem could be rectified by increasing the

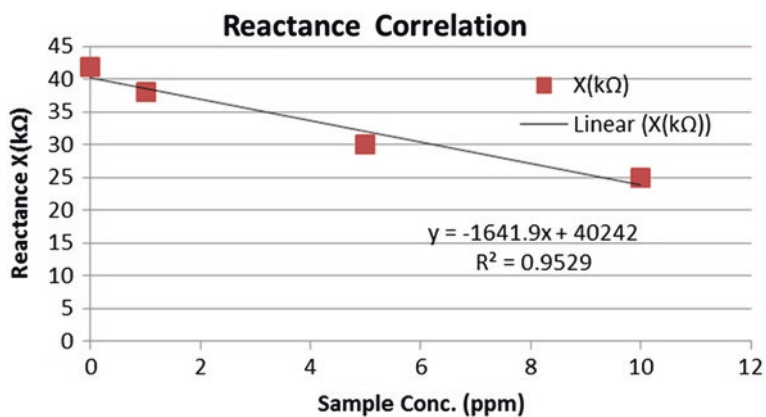
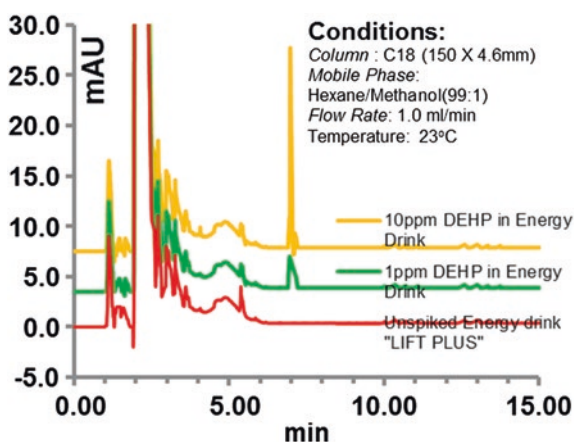


Fig. 6.22 Reactance correlation chart for DEHP concentration in tainted energy drink read by the proposed system

Table 6.2 Equivalent circuit parameters evaluated by CNLS fitting for DEHP detection in 'Lift Plus' drink by MIP functionalized sensor

Eq. circuit parameters (unit)	DEHP spiked energy drink—MIP functionalized sensor		
	1 ppm	5 ppm	10 ppm
C_{ad} (F)	1.81E-07	1.35E-07	1.46E-07
R_s (Ω)	1.14E+02	1.33E+02	1.58E+02
R_{ct} (Ω)	8.23E04	6.21E+04	5.57E+04
Z_w (Ω)	2.43E06	1.92E+06	1.64E+06
C_{dl} (F)	7.95E-09	8.79E-09	9.25E-09

Fig. 6.23 HPLC chromatogram showing the DEHP peaks in the eluent extracted out of the functionalized MIP



density of the DEHP recognition sites in the MIP matrix by adding more template molecules. The quantity of the template compound added in the pre-polymerization complex determines the density of the recognition sites formed in resulting MIP.

6.8 Conclusions

Non-invasive, real-time detection technique for ubiquitous environmental endocrine-disrupting compounds in water has been discussed. Optimization of design for MEMS-based interdigital sensors has been achieved on the basis of mathematical modeling using finite element modeling software COMSOL Multiphysics®. Optimized designs of sensors have been fabricated using thin film semiconductor device fabrication techniques. The sensing surface was functionalized by a self-assembled monolayer of 3-aminopropyltriethoxysilane (APTES) with embedded molecular imprinted polymer (MIP) to introduce selectivity for the di (2-ethylhexyl) phthalate (DEHP) molecule. Various concentrations (1, 10 and 50 ppm) of DEHP in deionized MilliQ water were tested using the functionalized sensing surface to capture the analyte. The frequency response analyzer (FRA) algorithm was used to obtain impedance spectra so as to determine sample conductance and capacitance for evaluation of phthalate concentration in the sample solution. Spectrum analysis algorithm interpreted the experimentally obtained impedance spectra by applying complex nonlinear least square (CNLS) curve fitting in order to obtain equivalent electrochemical circuit and corresponding circuit parameters describing the kinetics of the electrochemical cell. The results achieved by the testing system were validated using commercially used HPLC-DAD.

References

1. K. Cammann, B. Ross, A. Katerkamp et al., Chemical and biochemical sensors. Ullmann's Encycl. Ind. Chem. (1994)
2. M.E. Tess, J.A. Cox, Chemical and biochemical sensors based on advances in materials chemistry. *J. Pharm. Biomed. Anal.* **19**(1), 55–68 (1999)
3. S. Shtykov, T.Y. Rusanova, Nanomaterials and nanotechnologies in chemical and biochemical sensors: capabilities and applications. *Russ. J. Gen. Chem.* **78**(12), 2521–2531 (2008)
4. B. Adhikari, S. Majumdar, Polymers in sensor applications. *Prog. Polym. Sci.* **29**(7), 699–766 (2004)
5. T. Panasyuk-Delaney, V.M. Mirsky, M. Ulbricht et al., Impedometric herbicide chemosensors based on molecularly imprinted polymers. *Anal. Chim. Acta* **435**(1), 157–162 (2001)
6. A. Merkoci, S. Alegret, New materials for electrochemical sensing IV. Molecular imprinted polymers. *TrAC Trends Anal. Chem.* **21**(11), 717–725 (2002)
7. V.B. Kandimalla, H. Ju, Molecular imprinting: a dynamic technique for diverse applications in analytical chemistry. *Anal. Bioanal. Chem.* **380**(4), 587–605 (2004)
8. C. Alexander, H.S. Andersson, L.I. Andersson et al., Molecular imprinting science and technology: a survey of the literature for the years up to and including 2003. *J. Mol. Recognit.* **19**(2), 106–180 (2006)

9. H. Shaikh, N. Memon, H. Khan et al., Preparation and characterization of molecularly imprinted polymer for di (2-ethylhexyl) phthalate: application to sample clean-up prior to gas chromatographic determination. *J. Chromatogr. A.* (2012)
10. K. Yongfeng, D. Wuping, L. Yan et al., Molecularly imprinted polymers of allyl- β -cyclodextrin and methacrylic acid for the solid-phase extraction of phthalate. *Carbohydr. Polym.* **88**(2), 459–464 (2012)
11. P. Qi, J. Wang, Y. Li et al., Molecularly imprinted solid-phase extraction coupled with HPLC for the selective determination of monobutyl phthalate in bottled water. *J. Sep. Sci.* **34**(19), 2712–2718 (2011)
12. F. Tamayo, E. Turiel, A. Martín-Esteban, Molecularly imprinted polymers for solid-phase extraction and solid-phase microextraction: recent developments and future trends. *J. Chromatogr. A* **1152**(1), 32–40 (2007)
13. L. Ye, K. Mosbach, Molecular imprinting: synthetic materials as substitutes for biological antibodies and receptors†. *Chem. Mater.* **20**(3), 859–868 (2008)
14. A. Bossi, F. Bonini, A. Turner et al., Molecularly imprinted polymers for the recognition of proteins: the state of the art. *Biosens. Bioelectron.* **22**(6), 1131–1137 (2007)
15. A. Mayes, M. Whitcombe, Synthetic strategies for the generation of molecularly imprinted organic polymers. *Adv. Drug Deliv. Rev.* **57**(12), 1742–1778 (2005)
16. J.-P. Lai, M.-L. Yang, R. Niessner et al., Molecularly imprinted microspheres and nanospheres for di (2-ethylhexyl) phthalate prepared by precipitation polymerization. *Anal. Bioanal. Chem.* **389**(2), 405–412 (2007)
17. H. Yan, X. Cheng, G. Yang, Dummy molecularly imprinted solid-phase extraction for selective determination of five phthalate esters in plastic bottled functional beverages. *J. Agric. Food Chem.* **60**(22), 5524–5531 (2012)
18. G. Díaz-Díaz, D. Antuña-Jiménez, M. Carmen Blanco-López et al., New materials for analytical biomimetic assays based on affinity and catalytic receptors prepared by molecular imprinting. *TrAC Trends Anal. Chem.* **33**, 68–80 (2012)
19. G. Sun, P. Wang, S. Ge et al., Photoelectrochemical sensor for pentachlorophenol on microfluidic paper-based analytical device based on molecular imprinting technique. *Biosensor. Bioelectron.* (2014)
20. J. Wolska, M. Bryjak, Sorption of phthalates on molecularly imprinted polymers. *Sep. Sci. Technol.* **47**(9), 1316–1321 (2012)
21. J. He, R. Lv, J. Zhu et al., Selective solid-phase extraction of dibutyl phthalate from soybean milk using molecular imprinted polymers. *Anal. Chim. Acta* **661**(2), 215–221 (2010)
22. A.I. Zia, S.C. Mukhopadhyay, P.-L. Yu et al., Rapid and molecular selective electrochemical sensing of phthalates in aqueous solution. *Biosens. Bioelectron.* **67**, 342–349 (15 May 2015)

Chapter 7

Portable Low-Cost Testing System for Phthalates' Detection

7.1 Introduction

A portable low-cost microcontroller-based testing system was designed and constructed to detect phthalates in aqueous media. Frequency response analyser (FRA) approach was used to develop the rapid response, non-invasive electrochemical impedimetric system for phthalate detection in field. A smart thin film gold interdigital electrodes capacitive sensor with enhanced penetration depth was used with the proposed system for detection of the said EDC. The performance of the developed system was evaluated by comparing the results to the commercially available electrochemical Impedimetric frequency response analyzer equipment. Complex nonlinear least square (CNLS) curve fitting algorithm was used to deduce the equivalent circuit for the developed system. The DEHP detection results by the developed system were validated using high performance liquid chromatography (HPLC) diode array detection confirming that the proposed system was able to detect the concentration of phthalates in aqueous medium [1].

7.2 Motivation

After ingestion, the phthalates are rapidly hydrolyzed to the corresponding monoester by the digestive system and excreted in urine and feces. In humans, short alkali chain phthalates are eliminated mostly within hours but long chain phthalates like DEHP require further metabolism via ω - and ω -1-oxidation of the aliphatic side chain [2]. Blood and urine are the most common matrices used for biomonitoring of EDCs, but the results of these biomonitors do not provide the complete picture of EDC intake, rather just provide the quantity of metabolites excreted losing information about the amounts of phthalate that have become the body burden. Therefore, it is necessary to have a hand-held portable sensing system which may detect the quantity of phthalates present in food and beverages as initial intake via the oral route [3, 4]. Food and beverages are deemed to be the biggest

source of human phthalate exposure due to the extensive use of food plastics packaging in our everyday lifestyle. The objective of this research is to develop a low-cost portable real-time testing system which is rapid, highly sensitive and involves minimal support electronics and should have a minimal level of complication in the application. Presented design of portable, low-cost FRA device with interdigital capacitive sensor design that was developed to detect selectively phthalates possesses properties of speed, real time and in situ testing in aqueous medium [5].

7.3 Development of Portable FRA Device

With an enormous research in the field of impedance measurements, frequency response analyser (FRA) has achieved a de facto standard for electrochemical impedance measurements. A dc potential overlaid by a small amplitude (5–15 mV) AC sine wave applied to the excitation electrode and the subsequent measurement of resulting AC current made is commonly termed as FRA [6].

7.4 System Design

Direct digital synthesis (DDS) was used to produce the sine wave at a digital-to-analogue (DAC) interface. This is implemented by breaking a waveform into discrete points allowing for the waveform to be digitally replicated; the more points were taken and the higher precision the DAC, the higher the resolution becomes compared to an analogue signal. 256 (8 bit) points were used to produce a sine wave that gave a compromise between resolution and frequency; as resolution increases, max frequency achievable decreases. The ability of Arduino microcontroller to set a whole port in one instruction allowed to be sent to the DAC attached to an 8 pin microcontroller port producing a reliable sine wave up to 1 kHz, an R2R ladder DAC connected to an 8 pin port was used to generate the sine wave due to unavailability of built-in DAC in the Arduino microcontroller. This removed the need for a filter and allowed for a controllable range of frequencies. However, it gave issues when there were many interrupts present to monitor the sensor, which deformed the waveform. A second Arduino microcontroller was used for sine wave generation to overcome this allowing precise and reliable frequency control. The waveform required to be about the ground reference having positive and negative features to give the desired input. This was achieved by using a Non-inverting op-amp with a negative offset to both push the waveform down, and to attenuate it to the required voltage. The op-amp needed to be attached to a negative voltage supply to output a negative voltage. This was achieved using a single power supply by using a 555 IC. Three operational amplifiers were used around the sensor to collect the signal and the current through the system was measured through a series resistor. Due to the sensor following resistors' small size the

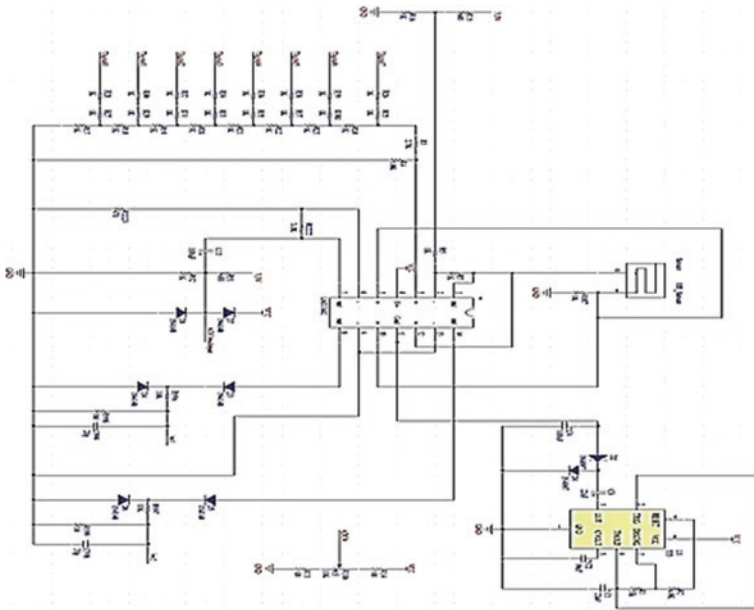


Fig. 7.1 Circuit diagram for the designed Arduino microcontroller based portable FRA

voltage drop across the resistor was significantly low, affecting the accuracy of the ADC. To reduce this issue, an op-amp was used to give a positive gain of 7 times to amplify the signal. This op amp also isolated the sensor from any circuitry used in front of this op-amp. This was important not to affect the capacitance of the sensor as this is the main factor being measured. A DC offset needed to be added to the signal before Arduinos’ ADC as it cannot handle a negative voltage. This offset was produced by a simple voltage divider, and a capacitor to decouple the offset from the output of the op-amp as shown below. Two diodes before the ADC were used to make sure the voltage stayed between 0 and 5 V. If they went higher or lower than this, the voltage would be dumped into the supply lines protecting the ADC. The diagram for the designed circuit is shown in Fig. 7.1,

The phase shift was obtained by using two zero-crossing circuits and two rising edge external interrupts on the Arduino. The output of this circuit is then sent through a diode (D3 and D5) to limit the negative current to 0.7 V and a resistor (R996 and R997) to limit the current to 0.5 mV. A second diode pair (D4 and D6) are meant to provide extra protection against negative high voltage. The RC combination (R998, C999, R999, and C998) were inspired by Oscilloscope probes that use the same circuit. The effect produced is not losing the signal at high frequencies due to noise and spikes.

A GUI interface was written in C++ that listens to the Serial port waiting for the starting frequency and collects data until the frequency of departure occurs again. The Microcontroller formats the data being output in the following way “F#n” “#n” “#n” for each reading. This allows the GUI to identify the starting

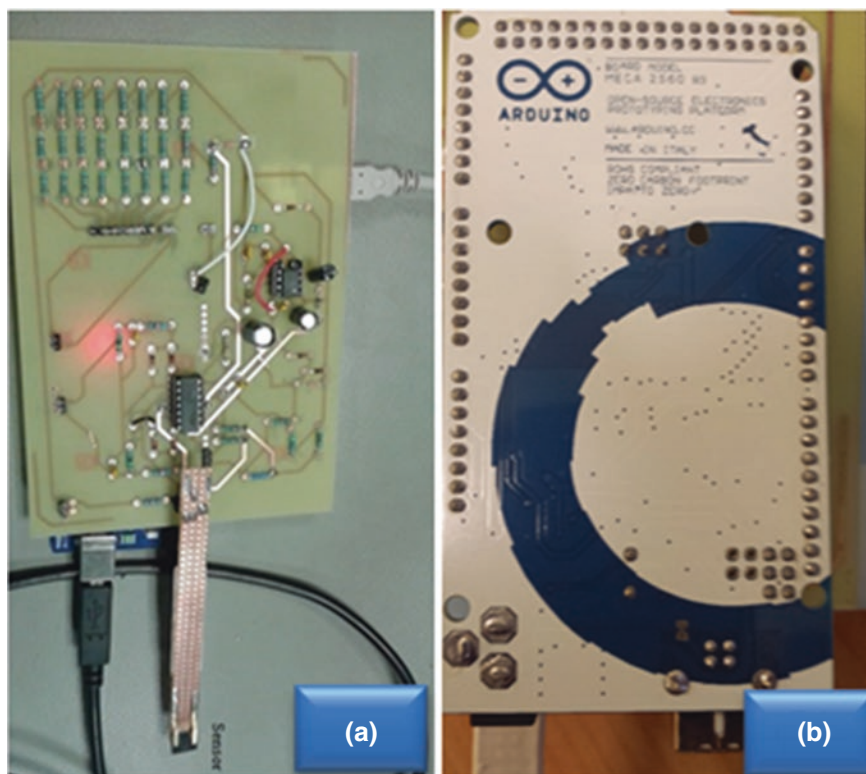


Fig. 7.2 Circuit board. **a** Component side with attached sensor. **b** Arduino microcontroller board for portable FRA

point of the data with the F, and each measurement ends with a line character i.e. print line (F + Frequency), print line (RMS), and print line (phase shift). Figure 7.2 illustrates the assembled and fully operational testing system.

The information read by the GUI was converted for analytical use. The output of the device read is the Frequency, V_{rms} , and Phase shift (θ). The absolute value of Impedance is calculated as follows $|Z| = 1.18 V_{\text{rms}}/70,000$.

However, this RMS value was amplified by 7 to make it readable by the ADC. Therefore it is really 7 times smaller; hence 70,000, rather than 10,000 (the resistor value).

7.5 Materials and Methods

Di (2-ethylhexyl) phthalate (DEHP) solution prepared gravimetrically at a concentration of 200 $\mu\text{g}/\text{mL}$ (200 ppm) in ethanol was received from ChemService[®] USA. Deionized water 18.2 $\text{M}\Omega\text{-cm}$ (MilliQ[®]) from Millipore USA was used to

prepare the samples of lower concentration by serial dilution method. Pure deionized water with a 200 ppm concentration of ethanol was used as control solution for the experiments. pH meter from IQ Scientific Instrument Inc. The USA was used to measure pH levels of the test and control solutions. The pH meter was calibrated with buffer solutions provided by the manufacturer prior to the testing of pH of the test samples [7].

Three different concentrations of DEHP—1, 10, and 50 mg l⁻¹ (ppm) in deionized water were tested at controlled temperature (20.3 °C) and humidity (44 %) conditions. The control solution was 18 MΩ-cm deionized MilliQ water with pH 6.71. The average pH value measured for all three samples was measured to be 6.52 at 20.3 °C. The sensing system was profiled in the air before its exposure to the different DEHP concentrations to create an experimental reference curve for the sensor performance. This curve plays a significant role in resetting the sensor to its initial conditions after testing each concentration.

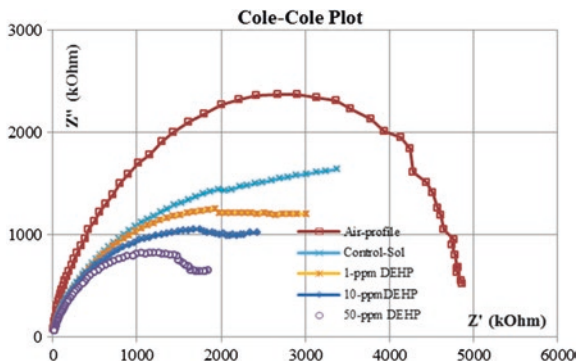
7.6 Results and Discussions

To verify the functionality of the designed device, the phase and V_{rms} measurements were compared to an oscilloscope. It should be noted that only the V_{rms} response was expected to match as the Oscilloscope measured peak-peak, which is very susceptible to noise. The phase shift between the input and the output of the sensor is the most critical parameter in determining the impedance. The comparison results in Table 7.1 shows an error less than 2 % for the designed device as compared to the phase shift measured by Hioki (Japan) high precision LCR meter.

Table 7.1 Performance parameters of the measured parameters

F (Hz)	Phase (°)		%error	V _{rms}		%error
	Portable tester	LCR (Hioki)		Portable tester	LCR (Hioki)	
10	1.72	1.75	1.72	0.57	0.58	1.7
100	1.07	1.05	1.90	0.57	0.58	1.72
200	-4.95	-5.0	1	0.615	0.62	0.80
300	-11.98	-12.0	0.16	0.63	0.64	1.56
400	-16.1	-16.0	-0.62	0.68	0.67	-1.4
500	-21.15	-21.1	-0.23	0.69	0.69	0
600	-25.3	-25.1	-0.79	0.73	0.73	0
700	-29.4	-29.2	-0.68	0.74	0.75	1.333
800	-32.95	-32.8	-0.45	0.81	0.80	-1.25
900	-35.32	-35.3	-0.05	0.82	0.81	-1.23

Fig. 7.3 Nyquist plot for data measured by the designed Arduino microcontroller based portable FRA



7.7 Electrochemical Impedance Spectroscopy Characterization

The outcome of an impedance measurement is represented as bode and Nyquist (Cole-Cole) plot which is further analyzed on the basis of Randle's equivalent circuit model in order to deduce electrical equivalent of exchange and diffusion processes describing the system kinetics by complex nonlinear least square curve fitting (CNLS) curve fitting of the experimental data. Nyquist plot for the portable testing system is given in Fig. 7.3. The decreasing diameter of the Nyquist plot indicates the increasing concentration of the phthalate in the sample [1].

It is observed that the sensor is sensitive to the adsorbed phthalate molecules at the electrode-solution interface at low frequencies. The real part of impedance curve dominates due to the presence of ionic concentration in the sample. The diffusion of ions in the electrode surface is a fast kinetic process which is taking place at the low-frequency range, on the other hand, the capacitive behavior of the sensor is observed at the relatively high-frequency range. Due to the dielectric properties of DEHP, the corresponding change in real and imaginary impedance values causes the diameter of the Nyquist plot to decrease with increasing concentration of DEHP in the sample solution. In order to investigate the dominance of ionic concentration in the test samples, real and imaginary parts of impedance are plotted against frequency which provide a clear picture of the nature of the material under test [8]. Figure 7.4 shows real part of the impedance plotted against frequency using new designed portable tester. It can be seen from the plot that the concentration change in analyte changes the real impedance, but it is not as dominating as the imaginary part of the impedance. The change in imaginary impedance represents the dielectric nature of the material under test consequently increasing the capacitance value of the sensor. The plot for the imaginary part of impedance is shown in Fig. 7.5. The plot shows that with the increasing concentration of DEHP the imaginary impedance of the system is decreasing which describes the dielectric nature of the analyte molecule.

Figures 7.6 and 7.7 shows the HPLC chromatograph for eluent after testing 1 and 10 ppm spiked aqueous samples respectively. A DEHP peak is observed at

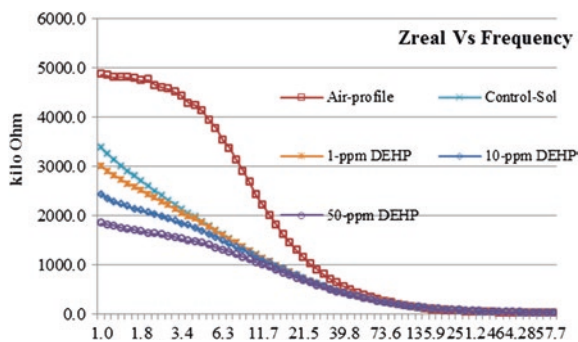


Fig. 7.4 Z' versus F (Hz) plot for the data acquired by portable FRA

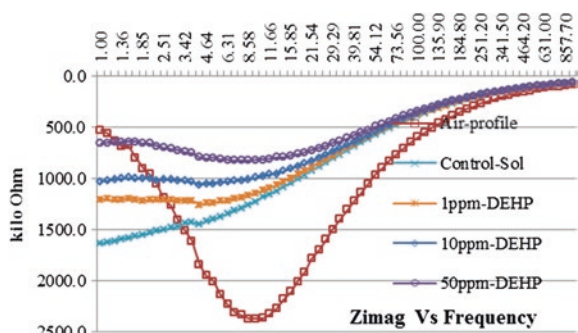


Fig. 7.5 Z'' versus F (Hz) plot for the data acquired by portable FRA

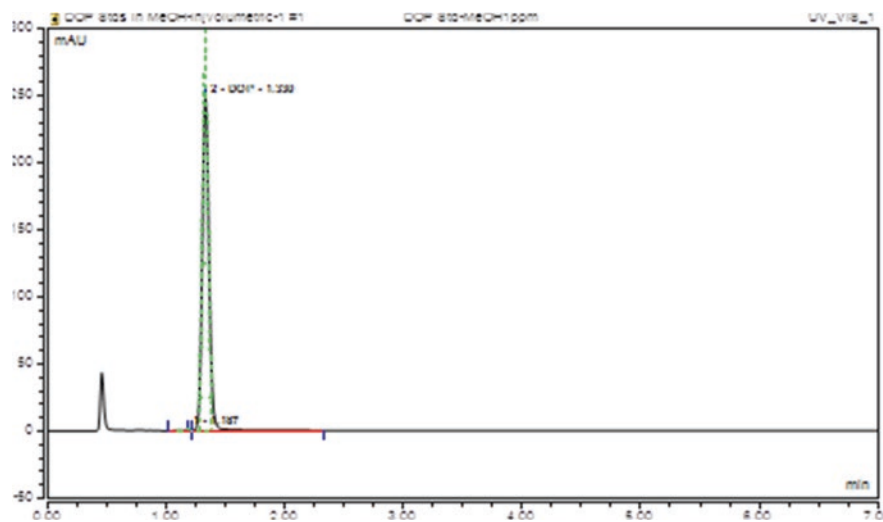


Fig. 7.6 HPLC-DAD for eluent from 1 ppm DEHP in spiked DI water

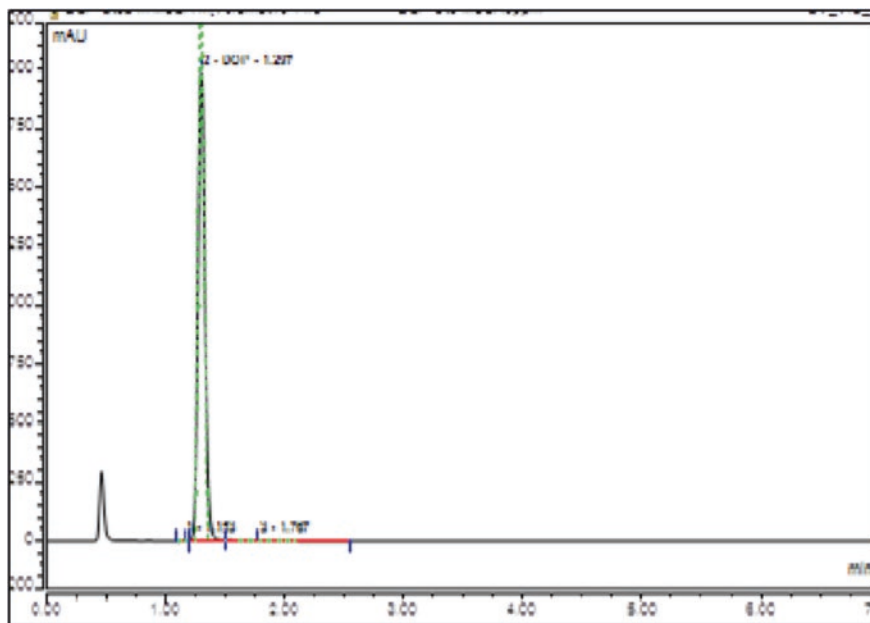


Fig. 7.7 HPLC-DAD for eluent from 10 ppm DEHP in spiked DI water

1.91 min with few initial noise peaks. The noise observed before the appearance of the DEHP peak is predominantly due to the presence of traces of solvent in the eluent which appears even in the HPLC chromatograph obtained for the control solution. The insolubility of DEHP in polar medium dictates the requirement for the use of a solvent to dissolve it in the aqueous medium.

7.8 Conclusions

A portable, low-cost microcontroller-based testing system has been designed and developed to detect phthalates in aqueous media. The frequency response analyser (FRA) approach has been used to develop the rapid response, a non-invasive electrochemical impedimetric system for phthalate detection. A smart thin film gold interdigital electrodes capacitive sensor with enhanced penetration depth was used with the proposed system for detection of the said EDC. The performance of the developed system has been evaluated by comparing the results to the commercially available electrochemical Impedimetric frequency response analyzer equipment. The DEHP detection results by the developed system have been validated using high-performance liquid chromatography (HPLC) diode array detection confirming that the proposed system was able to detect the concentration of phthalates in an aqueous medium.

References

1. A.I. Zia, M.S.A. Rahman, S.C. Mukhopadhyay et al., Technique for rapid detection of phthalates in water and beverages. *J. Food Eng.* **116**(2), 515–523 (2013)
2. H.M. Koch, A.M. Calafat, Human body burdens of chemicals used in plastic manufacture. *Philos. Trans. R. Soc. B Biol. Sci.* **364**(1526), 2063–2078 (2009)
3. A.I. Zia, A. Mohd Syaifudin, S. Mukhopadhyay et al., *Development of Electrochemical Impedance Spectroscopy Based Sensing System for DEHP Detection*, pp. 666–674
4. A.I. Zia, A. Mohd Syaifudin, S. Mukhopadhyay et al., *Sensor and Instrumentation for Progesterone Detection*, pp. 1220–1225
5. A.Z.S.C. Mukhopadhyay, P.L. Yu, I.H. Al Bahadly et al., *Ovarian Hormone Estrone Glucuronide (E1G) Quantification- Impedimetric Electrochemical Spectroscopy Approach*, pp. 22–27
6. A. Zia, S. Mukhopadhyay, P. Yu et al., Post annealing performance evaluation of printable interdigital capacitive sensors by principal component analysis. *IEEE Sensors J.* (2014)
7. A.I. Zia, S. Mukhopadhyay, I. Al-Bahadly et al., *Introducing Molecular Selectivity in Rapid Impedimetric Sensing of Phthalates*, pp. 838–843
8. A.I. Zia, S.C. Mukhopadhyay, P.-L. Yu et al., Rapid and molecular selective electrochemical sensing of phthalates in aqueous solution. *Biosens. Bioelectron.* **67**(15), 342–349 (2015)

Chapter 8

Conclusions and Future Research

8.1 Summary and Conclusions

This manuscript contributed to the impedance spectroscopy research for the development of novel interdigital sensors by applying this technique to hormone and chemical detection. The research work required to do a substantial addition to the existing knowledge includes, but not limited to the literature surveys in this and allied fields, design and design developments, simulations and fabrications, experimentation and analyses, measurements and hypothesis, functionalization and immobilization, selectivity and sensitivity, detailed mathematical and statistical analyses and result validations. The presented research work has successfully been applied to develop an exciting transducer that could not only selectively detect its target but is capable enough to quantify harmful synthesized organic impurities in our food stuff. This research work has not only provided a real-time tool to perform week-long chemical and biochemical assays in minutes yet, but it had also been operating as a source of community awareness about the said chemicals that we keep ingesting knowing or unknowingly. Consequently, these teratogenic, endogenic and carcinogenic chemicals become our body burden, and we fall prey to some incurable diseases that cause to shorten our life span.

The research work executed in this capacity is a set of sequential moves to this accomplishment, described as follows.

The first chapter defines and highlights the problem and its gravity. In the introduction part it briefly describes the good and the bad; hormones, that are the proper chemicals generated by a living body naturally, to help it grow, nurture and nourish and endocrine disrupting compounds, the dangerous chemicals that when enter the living body, mimic hormones, damage and destroy the natural balances and cause devastating malfunctions in body metabolisms. The author then tried to find some way to detect these silent killers in the existing human knowledge-base by reviewing the up-to-date research published in this context. The basic objective of the author in this search was to find out some method that may be smart enough to identify these chemicals to a trace level of parts per million to parts per billion,

in addition to a rapid and real-time execution of the investigation. During this endeavour, the author came across a few excellent approaches to the solution of the problem but, unfortunately, none of those could qualify the condition of rapid detection. Over and above, all these technologies required stringent test conditions and large machines worth millions of dollars. These methodologies may be affordable to the elite class of the community, but an average member may afford it once in a blue moon only. At the end of the chapter a comprehensive comparison of all the related technologies have been discussed in order to emphasize the scarcity of a sensitive and rapid technique for chemical and biochemical assay.

The next milestone to this journey was to search out some technique that may have the throbbing potential to fulfil the targeted conditions but has not yet been so developed to cater for it. Chapter 2 described the methods and methodologies, merits and demerits, dos and don'ts, pros and cons of the electrochemical impedance spectroscopy (EIS) technique. The author selected it to proceed further on researching it because it had enough potential for sensitivity, rapidness and did not require any bulky test equipment due to which it was one of the lowest cost technologies ever known. The author tried to make the reader of this book well versant with the equipment used, methodologies, conditions and analytical methods applied in this technique to deduce the results of Chap. 2.

After an explanation to build a standalone EIS data acquisition system that may work semi-automatically using a computer, the author started working on the development of a transducer that could interpret the material information extracted by EIS into readable electrical signals. This transducer was supposed to be the heart and soul of the detection system. Therefore, it had to be highly sensitive, precisely selective, carefully designed and thoroughly tested and tried.

Planar interdigital capacitive sensors have been under extensive research and development for last two decades. They have shown a high level of accuracy and excellent sensitivity of measurements in the evaluation of near-surface properties like permeability, conductivity, dielectric properties of materials, non-invasive testing, label-free detection of biological species and analysis of chemical compounds. The coplanar structure provides freedom of in situ and single side access feature for the sensor along with acceptable signal-to-noise ratio in measurements. The capacitance and conductance between the sensors' electrodes is dependent on the material, geometry and dielectric properties of the analyte. When these sensors operate in conjunction with the Electrochemical Impedance Spectroscopy (EIS), a technique applied alternating electromagnetic perturbations fringe through the material sample producing capacitive effects as a result of the presence of analyte molecule in the sample under test. The impedance Z of a system is determined as a function of frequency and by analysing the resultant current through the system in terms of amplitude and phase shift compared to voltage–time function.

Chapter 3 detailed the steps involved in design and simulation of the interdigital capacitive transducer. It explained the worked out improvements in the design of the sensor that was simulated to assure virtually the sensitivity and operation. Smart fruitful collaborative partnerships were established to fabricate these sensors at King Abdullah University of Science and Technology, Saudi Arabia. These

sensors were fabricated on single crystal silicon wafer widely used in the ICs fabrication in semiconductor fabrication industry. The sensors were designed simulated in a miniature size with multiple configurations of sensing electrode structures. Silicon based sensors provided low-cost fabrication opportunity where 36 sensors could be fabricated on a single 4-in. silicon wafer. High sensitivity, low impedance and better sensing signal to low noise ratio were the most important characteristics requirements for these sensors.

The details of fabrication and initial testing of known materials are discussed. A therapeutic post-fabrication heat treatment was applied to the interdigital sensor to achieve improvement in its performance, but keeping the fabrication cost to the bare minimum level. A combination of sputtered gold electrodes deposition and post-annealing procedure served the dual purpose of low cost and better performance of the sensor. The shortcomings marked out in testing and the remedial actions taken to overcome those shortcomings have been discussed in Chap. 3.

The objective of Chap. 4 was to investigate the capability of the designed sensors, and to explore the analytical powers of electrochemical impedance spectroscopy, in the detection of different hormones. The target hormones are related to the reproductive cycle of mammals. ‘Non-invasiveness of methodology’ and ‘real-time measurements of samples’ were the prime objectives of this research project. These characteristics of the presented research make this work unique in comparison to all available contemporary methodologies. Apart from that, it was envisaged that execution of the hormone quantification assay should be simple enough to be adapted by a common user without requiring a necessary scientific background.

The first part of this chapter discussed the application of the proposed system to detect estrone glucuronide, an excretory metabolite of estradiol, commonly known as E1G. This hormone plays a significant role in the reproductive fertility of human female. The information on the quantity of excretion of this hormone metabolite is useful in determining the window of fertility for a human female. The handy availability of this information is essential to achieve conception or contraception in the human reproductive cycle.

The second part of the chapter dealt with the sensor’s response in the detection of progesterone hormone excreted in the milk of dairy cows. Obtaining urine samples, to gather the fertility information, is not feasible in the case of dairy animals. Though, milk owns a complex chemical matrix, yet it is the easiest and most non-invasive method to achieve the information on ‘window of fertility’ for the animal.

Electrochemical impedance analyses making use of bode plots, Nyquist plots, CNLS curve fitting, electrochemical equivalent circuit parameters and sensitivity of the sensor toward the analytes were discussed in Chap. 4.

Endocrine disrupting compounds are exogenous chemicals or mixture of chemicals that interfere the normal functioning of the endocrine system and cause hormonal imbalances in living organisms. These hormonal imbalances can cause cancers, birth defects, developmental disorders, nutritional malfunctions and impotence, especially in males. EDC can block the receptor cells by stopping them to respond or can cause an adverse response by getting attached to the receptor in place of a hormone cell.

In Chap. 5 the advanced sensor and sensing system was employed to detect two types of phthalates spiked in different kinds of mediums. The tests were performed in real-time and the sensor performed successfully in the detection of phthalates in the pure polar medium. The system was able to detect the presence of DEHP and DINP even to a trace level in the polar medium, but the outcomes of the investigation made for electrolytic and acidic media were not up to the mark. Although, the sensitivity analysis of the system displayed a high level of sensitivity in pure aqueous and organic solvent media yet, the system sensitivity deteriorated drastically in complex solutions. This led the sensing system research to the next stage of development. In order to adapt the sensor and sensing system for complex chemical matrices like beverages, milk and urine, selectivity for analyte molecules was an absolute requirement. Different options to pave the way to selective adsorption of phthalates on the sensing surface have been explored.

Published research provides a number of methods to detect selectively analyte from a complex matrix by extraction, absorption, adsorption, biological separation and filtration. Unfortunately, all these techniques are laboratory based and require certain skills and expertise to perform. On the other hand, these techniques are extremely delicate and require certain environmental conditions to execute.

One of the main objectives of this research was to develop an assay system that is robust enough to have an in-field application without any technical expertise requirement for the user. To achieve this objective, a robust assay technique was tailored and applied to induce selectivity in the designed sensing system. The discussion on inducing selectivity for specific molecules was carried out in Chap. 6 of this book.

Non-invasive, real-time analyte-selective detection technique for ubiquitous environmental endocrine-disrupting compounds in water has been discussed in Chap 6. The sensing surface was functionalized by a self-assembled monolayer of 3-aminopropyltriethoxysilane (APTES) with embedded molecular imprinted polymer (MIP) to introduce selectivity for the di (2-ethylhexyl) phthalate (DEHP) molecule. Various concentrations (1, 10 and 50 ppm) of DEHP in deionized MilliQ water were tested using the functionalized sensing surface to capture the analyte. The frequency response analyser (FRA) algorithm was used to obtain impedance spectra so as to determine sample conductance and capacitance for evaluation of phthalate concentration in the sample solution. Spectrum analysis algorithm interpreted the experimentally obtained impedance spectra by applying complex nonlinear least square (CNLS) curve fitting in order to obtain equivalent electrochemical circuit and corresponding circuit parameters describing the kinetics of the electrochemical cell. The results achieved by the testing system were validated using commercially available high-performance liquid chromatography-diode array detection at an incident wavelength at 224 nm. DEHP spiked energy drink was also investigated by the developed technology in order to confirm its operation in the real world scenario.

A portable, low-cost microcontroller-based testing system was designed and constructed to detect phthalates in aqueous media. Chapter 7 discussed the steps involved in design and simulation of the hand-held prototype of the proposed

sensing system. The performance of the developed system was evaluated by comparing the results to the commercially available electrochemical Impedimetric frequency response analyzer equipment. CNLS curve fitting algorithm was used to deduce the equivalent circuit for the developed system. The DEHP detection results by the developed system were validated using high-performance liquid chromatography (HPLC) diode array detection confirming that the proposed system was able to detect the concentration of phthalates in an aqueous medium.

8.2 Future Work

8.2.1 Sensitivity and Selectivity Improvement

A satisfactory performance of the sensing system has been achieved though; still a few of following improvements in the sensor and sensing system can make it even better.

1. The sensitivity may be improved by trying different polymerising materials with higher densities of recognition sites.
2. By improving the coating method with spin coating or electro-spin coating methods.
3. Specific coating thickness and uniform layers of cross-linker may be explored.
4. Uniform/patterned distributions of molecular recognition sites to achieve known density of molecular trapping site.
5. Better analyses of results by CNLS can provide more insight in the electrochemical cell.
6. Conducting EIS experiments at a wider range of frequencies starting from mHz range can provide better sensitivity.
7. Change in sensor design is suggested as in Fig. 8.1. This design change will reduce the capacitive effect caused between the connecting lines that will help improve sensitivity.
8. Increasing the length of the sensor will allow soldering flexible wires to the connection pads as shown in Fig. 8.1. That will help keep the sensing part away from the solder heat.
9. Annealing the substrate at 210 °C for two hours should be added as a post-fabrication step in the fabrication process so that all the defects caused in the electrodes' surface due to gold sputtering get removed.

8.2.2 Thick Film Electrodes

The sensors may be fabricated using thick film electrodes. The available sensors' electrodes are formed by sputter coating 500 nm gold over a chromium seed layer of 20 nm thickness. New sensors with electrode thickness as much as 5 μm should

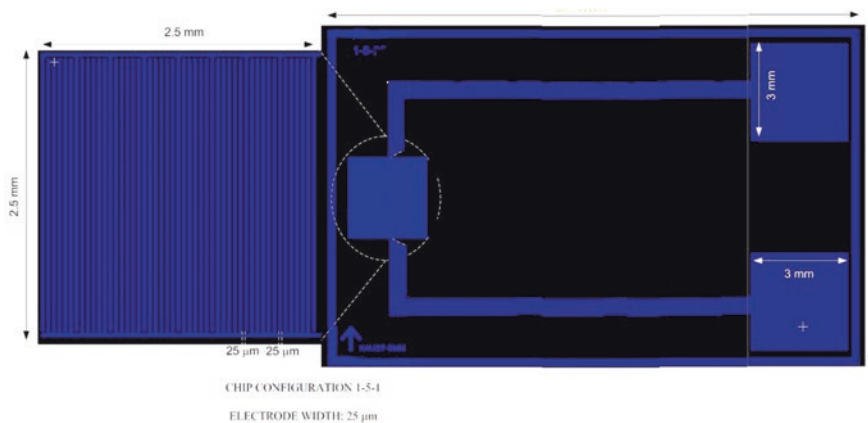


Fig. 8.1 New sensor design to overcome heat and stray capacitance problems

be fabricated and tested. Thick electrode will be able to provide a uniform electric field as high as $5 \mu\text{m}$ between the electrodes. The availability of a uniform electric field along with fringing field will increase the sensitivity many folds. The analyte molecules adsorbed to the silicon surface between the electrodes will contribute more to the C_{ad} and C_{dl} .

8.2.3 Substrate Type

The Si substrate used for the fabrication, presently, is single crystal Si wafer without any doping concentration. It is suggested that p-type and n-type doped Si wafers may also be used for sensor fabrication. The interdigital electrodes should be deposited on silicon dioxide insulation layer. The partially conductive substrate will provide a conductive path to the electric field through the substrate material on the rear side of the sensor. This will help reduce noise in the EIS measurements. Presently a back Au plane at ground potential serves the purpose.